Multi-component decompositions for Spitzer Survey of Stellar Structure in Galaxies (S^4G): I Decomposition strategies and data release (24/06/2014)

H. Salo[1], E. Laurikainen[1,2], J. Laine[1], S. Comerón[1], D. Gadotti, R. Buta, K. Sheth, D. Zaritsky, L. Ho, J. Knapen, E. Athannassoula, A. Bosma

+ S^4G team members

Received _____; accepted _____

[1]Dept. of Physics/Astronomy Division, University of Oulu, FI-90014, Finland

[2]Finnish Centre for Astronomy with ESO (FINCA), University of Turku, Väisälantie 20, FI-21500 Piikkiö, Finland

ABSTRACT

The Spitzer Survey of Stellar Structure in Galaxies (S^{4}G, Sheth et al. 2010) is a deep 3.6 and 4.5 μm imaging survey of 2352 nearby ($< 40Mpc$) galaxies. We describe the S^{4}G data analysis pipeline 4, which is dedicated to 2-dimensional structural surface brightness decompositions of 3.6 μm images, using GALFIT3.0 (Peng et al. 2010). Besides automatic 1-component Sérsic fits, and 2-component Sérsic bulge + exponential disk fits, we present human supervised multi-component decompositions, which include, when judged appropriate, a central point source, bulge, disk, and bar components. Comparison of the fitted parameters indicates that multi-component models are needed to obtain reliable estimates for the bulge Sérsic index and bulge-to-total light ratio (B/T), confirming earlier results (Laurikainen et al. 2007, Gadotti et al. 2009, Weinzirl et al. 2009). In this first Part, we describe the preparations of input data done for decompositions, give examples of our decomposition strategy, and describe the data products released via IRSA and via our web page (`www.oulu.fi/astronomy/S4G_PIPELINE4/MAIN`). These products include all the input data and decomposition files in electronic form, making it easy to extend the decompositions to suit specific science purposes. We also provide our IDL-based visualization tools (GALFIDL) developed for displaying/running GALFIT-decompositions, as well as our mask editing procedure (MASK_EDIT) used in data preparation. In the second Part we will present a detailed analysis of the bulge, disk, and bar parameter derived from multi-component decompositions.

Subject headings: galaxies: spiral —galaxies: kinematics and dynamics —galaxies: structure

1. Introduction

How and when did the baryonic mass assemble into galactic disks? How does the fraction of mass confined into bulges evolve over time? How common are galaxies that have no classical bulges, i.e. bulges that have their origin in the early mergers of dark matter halos and baryonic disk systems? These are difficult questions to answer because galaxy evolution involves secular processes like gas accretion via filaments, where mass presumably ends up in bulges, or internal dynamical evolution, leading to the formation of bars which further re-distribute matter in galaxies. Galaxies in the local Universe are the end products of this evolution and hence provide important clues to the past.

The Spitzer Survey of Stellar Structure (S^4G, Sheth et al. 2010) provides an excellent data base with which to measure the mass distribution of galaxies in the local Universe. It is a survey of more than 2300 galaxies observed in the mid-IR at 3.6 and 4.5 μm, wavelengths that are largely unaffected by internal extinction (Draine & Lee 1984), and trace mainly the old stellar population (Pahre et al. 2004; however see also Meidt et al. 2012 and Driver et al. 2013), so that the mass-to-luminosity (M/L) ratio in these bands is nearly constant inside the galaxies (Peletier et al. 2012). This is particularly important for deriving the properties of bulges and disks, because dust and star formation are more pronounced in the disks than in the bulges, which in the optical region affect their relative M/L-ratio and thus the relative fraction of the bulge light (Driver et al. 2013). Dust and star formation are significant also in the bulges of late-type galaxies (Fisher 2006). The S^4G images are deep, reaching azimuthally averaged stellar mass surface densities of ~ 1 M_0 pc^{-2}, where the baryonic mass budget is typically dominated by atomic gas. S^4G covers a large range of galaxy magnitudes (over three decades in stellar mass), which makes possible to study both dwarfs and bright galaxies in a uniform manner, and to study when the disk instabilities via bar formation start to play an important role. Our sample extends to lower galaxy

luminosities than most previous samples in which bars have been studied (Barazza et al. 2008, Nair et al. 2010, Melvin et al. 2014).

Plenty of information for the S^{4}G sample is already publicly available via the IRSA archive. The data have been processed through Pipeline 1 (P1, Regan et al. 2014) which makes mosaics of the observed individual frames, Pipeline 2 (P2) which makes masks of the foreground stars and image defects, and Pipeline 3 (P3, Munoz-Mateos et al. 2014) which measures the basic photometric parameters like the galaxy magnitudes and concentration indices. In Pipeline 4 (P4), described in this study, we decompose the two-dimensional flux distributions of the images into several structural components using GALFIT (Peng et al. 2010). Because even the mid-IR wavelengths are not completely free of such contaminants as hot dust, mass maps are also created for the images in Pipeline 5 (P5, Querejeta et al. 2014). The galaxies in S^{4}G have been visually classified at 3.6 μm by Buta et al. (2014), whose classifications are used in this study.

For all of the S^{4}G galaxies for which the image quality is good enough, we provide 1-component single Sérsic, 2-component bulge-disk (Sérsic + exponential), and multi-component decompositions, fitting four components at maximum. Our main goal is to estimate the parameters of the bulge and the disk in a reliable manner, which is the motivation for our decomposition approach. In particular, it is important to include bar-components in the decompositions because the flux of the bar is easily mixed with the flux of the bulge (Laurikainen et al. 2006). To measure the scale lengths and central surface brightness of the disks in a uniform fashion, an exponential function is used whenever possible, instead of a generalized Sérsic function. It is well known that galactic disks can have more than one exponential sub-section (Freeman 1970, Erwin, Beckman & Pohlen 2005). In this study we handle this in a fairly conservative manner: two separate functions are used to fit the disk in galaxies where distinct inner and outer components of different

surface brightness are present, but not in all cases in which a disk truncation of some degree has been reported in the literature. Our multi-component approach is similar to those used previously by Laurikainen et al. (2005, 2007, 2010), Gadotti (2009), and Weinzirl et al. (2009). Our motivation for offering also the single Sérsic and bulge-disk decompositions is that they are routinely used in large galaxy surveys (Häuβler et al. 2013, Lackner & Gunn 2012, Cameron et al. 2009, Allen et al. 2006, Driver et al. 2006, 2013). Although single Sérsic fits are not good tracers of the properties of bulges, they are still useful in gross classification of galaxies.

The decomposition results, released via IRSA and our web-page, are given in such a manner that they can be easily extended having different scientific goals in mind. The decompositions were done via GALFIDL, which consists of IDL-based tools for displaying and running GALFIT. It is important to note that due to a large amount of work involved, P4 was started as soon as first P1 data was available. Because of this we did our own mask editing, and orientation and sky background estimation. These masks form part of the final P2 masks. Due to later changes in P1, part of the images used in P4 contain minor shifts (or differ in size by 1-2 pixels) compared to the finalized P1 images in IRSA. Rather than repeating the time consuming GALFIT decompositions with the updated images, we provide together with the decomposition output files the sky subtracted data and mask images we used.

In this Part, we describe the decomposition method and model components, the preparation of the data for decompositions, and concentrate on illustrating our philosophy behind the construction of the final multi-component decompositions. The results published in tabular form include the outer disk orientation estimates, Sérsic parameters from the 1-component fits, and the final parameters from multi-component decompositions, together with a quality flag for each galaxy. The data products released via IRSA include the

GALFIT output files, and all the input fits-files needed for repeating and refining the decompositions. The P4 web pages illustrate the same models in pictorial form, and also provide the GALFIDL code and documentation. (IRSA products and P4 web page are described in the two Appendixes). Analysis of the derived bulge, disk, and bar parameters will be presented in Part 2 (Salo et al, in prep.).

2. Decomposition Pipeline

2.1. Decomposition method and model functions

Our decompositions use the GALFIT-software (Peng et al. 2002, 2010), which has become the *de facto* standard for detailed two-dimensional structural decompositions. It relies on parametric fitting, using the Levenberg-Marquadt algorithm to minimize the weighted residual χ^2 between observed (OBS) and model (MODEL) images,

$$\chi^2 = \frac{1}{N} \sum_x \sum_y \frac{[OBS(x,y) - MODEL(x,y)]^2}{\sigma(x,y)^2}. \quad (1)$$

The sum is taken over all the used (non-masked) image pixels, and $\sigma(x,y)$ indicates the statistical uncertainty of each pixel (*sigma-image*). The model image consists of a sum of model components, i.e for bulge, disk, bar etc, convolved with the image Point-Spread Function (PSF-image). Note that reduced χ^2 is used, with N denoting the degree of freedom, equal to the number of fitted pixels minus the number of free parameters in the fit.

GALFIT it extremely versatile in its selection of model components. Basically the user defines for each component its 'radial' profile function, giving the surface brightness $\Sigma(r)$ at each isophotal radial coordinate r. The isophotal coordinates are most commonly defined in terms of generalized ellipses (Athanassoula et al. 1990),

$$r(x',y') = \left(|x'-x_0|^{C+2} + \left| \frac{y'-y_0}{q} \right|^{C+2} \right)^{\frac{1}{C+2}} . \quad (2)$$

Here x_0, y_0 defines the center of the ellipse, $q = b/a$ is the ratio between minor and major axis lengths. The x', y' denote coordinates in a system aligned with the ellipse, with the major axis pointing at the position angle PA. For pure ellipses $C = 0$, while $C > 0$ indicates boxy and $C < 0$ disky isophotes. For the pipeline decompositions, simple elliptical isophotes $C = 0$ are used for all components. Besides generalized ellipses, GALFIT provides several alternatives, like definition of isophotal shape via azimuthal or bending modes, or via coordinate rotations, which would form a natural basis for detailed modeling of e.g. logarithmic spirals. To keep our models relatively simple (and uniform over the wide range of angular sizes and surface brightnesses spanned by the sample), we have not used these advanced GALFIT features. Keeping the models simple makes the interpretation of the observation minus model residuals more straightforward (see the NGC 1097 examples in Sheth et al. 2010).

The pipeline decompositions use five different choices for the model components/radial functions:

1) The **bulge component** is described with a Sérsic profile (*"sersic"*)

$$\Sigma(r) = \Sigma_e \exp\left(-\kappa \left[(r/R_e)^{1/n} - 1\right]\right), \quad (3)$$

where Σ_e is the surface brightness at the effective radius R_e (isophotal radius encompassing half of the total flux of the component). The Sérsic-index n describes the shape of the radial profile, which becomes steeper with increasing n. In particular, $n = 1$ corresponds to an exponential profile and $n = 4$ to de Vaucouleurs profile. The factor κ is a normalization constant determined by n. In GALFIT the corresponding *"sersic"*-function is used, with the integrated magnitude m_{bulge} as a free parameter (instead of Σ_e).

2) In the case of low or moderate inclination, the **disk component** is described with an infinitesimally thin exponential disk (*"expodisk"*) ,

$$\Sigma(r) = \Sigma_o q^{-1} \exp(-r/h_r), \tag{4}$$

where Σ_o is the central surface brightness of the disk observed from the perpendicular direction and h_r denotes the exponential scale length. In this case the $q = \cos i$, where i is the disk inclination. Assuming no extinction, $\Sigma_o q^{-1}$ is the projected surface brightness at the sky plane. The *"expodisk"*-function in GALFIT is used, with integrated $m_{disk} = -2.5 \log_{10}(2\pi\Sigma_0 \ {h_r}^2)$ as a free parameter (instead of Σ_0).

3) For a nearly **edge-on disk** (apparent axial ratio $q \lesssim 0.2$), the function (*"edgedisk"*)

$$\Sigma(r_x, r_z) = \Sigma_o \frac{r_x}{h_r} K_1 \left(\frac{r_x}{h_r} \right) \ \mathrm{sech}^2(r_z/h_z), \tag{5}$$

is adopted, where r_x and r_z are the (positive) distances along and perpendicular to the apparent major axis of the disk, and K_1 stands for a modified Bessel function. This function corresponds to the line-of-sight (viewing along the disk plane) integrated surface brightness of a 3D luminosity density distribution (van der Kruit & Searle 1981)

$$L(r_x, r_z) = \frac{\Sigma_0}{2h_r} \exp(-r_x/h_r) \ \mathrm{sech}^2(r_z/h_z). \tag{6}$$

4) For a **bar component** a modified Ferrers profile (*"ferrer2"*)is assumed,

$$\Sigma(r) = \begin{cases} \Sigma_o \left[1 - (r/r_{out})^{2-\beta}\right]^{\alpha} & r < r_{out} \\ 0 & r \geq r_{out} \end{cases} \tag{7}$$

Here r_{out} defines the outer cut of the profile, while α defines the sharpness of this cut. The parameter β defines the central slope of the profile, and Σ_0 is the central surface brightness (at sky plane). The modified Ferrers function in GALFIT is used, with Σ_e as a free parameter (instead of Σ_0).

5) When the galaxy contains an **unresolved central component** it is fit with a PSF-convolved point source (*"psf"*). In this case the free parameter is the total magnitude m_{psf}. Typically this component, if present, is not an active or starburst nucleus, but rather a small bulge with angular size so small that it cannot be resolved in the S^{4}G images ($R_e \lesssim FWHM = 2.1''$ of S^{4}G images).

For the decomposition pipeline we chose to do three types of decompositions: 1) one-component Sérsic-fits, 2) two-component bulge-disk decompositions using Sérsic-bulges and exponential disks (or edge-on disk if appropriate), and 3) multi-component 'final' decompositions, optionally with additional bar and central components (the level of complexity of the models is discussed in more detail in Section 3). The first two types of models are made in an automatic manner, while the final models always include human judgment about what components should be included.

2.2. Preparation of data for decompositions

2.2.1. What is needed?

The S^{4}G data analysis Pipeline P1 (Regan et al. 2014) provides image mosaics in both 3.6 and 4.5 μm, accompanied with *weight-images*, which indicate for each pixel location the number of original frames covering it. Together with the header information, these weight images provide means for producing the *sigma-images* needed in GALFIT.

Before decompositions can be started, frames masking the foreground/background objects and various image defects are needed. Additionally we need the galaxy centers, sky background values, and the orientation of the galaxy relative to the sky plane, estimated from the shape of the galaxy's outer isophotes. In principle, this additional input for

decompositions are published for all S^{4}G galaxies in Munoz-Mateos et al (2014), available via IRSA/S^{4}G Pipeline 3. However, at the time our Pipeline 4 decompositions were made, these data was not yet available. Therefore, we made our own sky background estimates and ellipse fits. Also, the automatically created masks (see Munoz-Mateos et al. 2014) were visually inspected and hand-edited when needed (these edited masks later became part of the final S^{4}G masks). If the decompositions are rerun starting from the output files provided in P4, it is important to use the data and mask images, as well as the pre-defined parameters offered via P4.

In summary, Pipeline 4 consists of scripts for editing the masks, determining the galaxy centers, estimating the sky background, fitting isophotal ellipses, preparing the input files, and running GALFIT. It also includes tools for visualization of the GALFIT output files (see Sect 2.4) and routines for storing the data on IRSA server (Appendix A) and the P4 web pages (Appendix B).

2.2.2. Mask images

The raw masks for the S^{4}G 3.6 μm images were made with the SExtractor software (Bertin & Arnouts 1996), as described in Munoz-Mateos et al. (2014). Various automatic detection thresholds for point sources were used. However, it soon became evident that no single criterion was sufficient to exclude all extra sources, without sometimes affecting also the galaxy light itself, in which case the masks needed manual editing. Also, in some cases the images contained artifacts that needed to be removed by hand. To speed-up this editing process, we developed a small portable IDL-routine (MASK_EDIT). Basically it displays on the screen simultaneously the original and masked images, and allows the user to remove/insert masked regions interactively. As an initial step of P4, all of the raw 3.6 μm masks were visually checked and edited if needed. The resulting masks are suitable

for the purposes of our structural decompositions. However, because the wings of the PSF are quite extended (see Section 2.2.6) more extensive masking might be required in some applications. The MASK_EDIT routine, with source code and examples of use, is available at the P4 web page.

2.2.3. Galaxy centers, sky background, isophotal profiles

After the edited masks were completed, we run the galaxies through a semi-automatic IDL script which determines the galaxy centers, sky background levels and galaxy orientation parameters. The accurate galaxy center is measured with the `cntrd`-routine[1], after its approximate location is interactively defined. We also have the option to mark the center by force, in case the automatic center finding routine does not work satisfactorily even after repeated trials.

The regions used for estimation of the sky background are identified manually, by selecting several (typically 10-20) locations outside the visible galaxy, while avoiding the image edges or contaminated areas. The local sky values in these locations are obtained by taking medians of the non-masked pixels in 40 pix $\times$ 40 pix boxes. The global sky background (SKY) and its uncertainty (DSKY) are then estimated from the mean and RMS of these local values, respectively (see Fig. 1). In section 3.1, using the estimated DSKY, we show that the expected uncertainty of decomposition parameters caused by possible uncertainties in background subtraction is negligible. We also determine the average RMS sky variation, by taking the median of standard deviations in different sky regions (after removing outliers by iterative 3-sigma clipping). We use the sky RMS estimates in Section

[1]`cntrd` is part of IDL Astronomy Library (Landsman 1993). It locates the position where brightness gradient is zero.

2.2.5 for assessing the validity of theoretically calculated sigma-images.

We calculate the isophotal profiles with a *pyraf* script called from IDL, using the standard IRAF `ellipse` algorithm. (Jedrzejewski 1987). As inputs for the ellipse fitting the sky background subtracted data image and the edited mask image are used. We fix the ellipse center to the previously found galaxy center and use a logarithmic increment of 0.02 between isophote levels. As often happens with IRAF `ellipse`, the fit does not necessarily converge over the whole galaxy area: we have an option to re-try the fit with different starting locations until a successful fit is obtained over the whole galaxy region (see Fig. 2). From the isophotal profiles, we choose a semi-major axis range from which outer orientations ($(b/a)_{outer} = 1 - \epsilon_{outer}, PA_{outer}$) are estimated, Also, a rough estimate of the galaxy outer radius, R_{gal}, is made to define the image region used in the GALFIT decomposition.

Figures 1 and 2 give examples of typical plots produced during these preparatory steps, illustrating the sky background fitting and the elliptical isophote profiles. The estimated ϵ_{outer} and PA_{outer} are marked. In all our decompositions, we fix the orientation of the disk component to these outer values[2] and interpret them to represent the galaxy viewing inclination. Therefore, extra care is taken to estimate the orientations reliably. For example, the corresponding inclination $i_{disk} = \cos^{-1}(b/a)_{outer}$ is visually checked by de-projecting the galaxy images to face-on. Figure 3 shows an example of such a de-projection, also comparing the estimated inclinations with those calculated from axial ratios given in the HyperLeda database. Typically, our $(b/a)_{outer}$ and PA_{outer} are determined at much lower surface brightness levels than those in HyperLeda (which are mainly from RC3). P4 values are thus less affected by bulges, bars, or prominent spirals, and should reflect better the orientation of the underlying extended disk, which appears with circular outer isophotes in

[2]The reason is to reduce the degeneracy of different model components in decompositions

face-on projection[3]. In some cases, S^{4}G images are so deep that the outermost isophotes are dominated by an outer stellar halo rather than the disk. Good examples are NGC 681, NGC 1055 and NGC 4594. Possible misinterpretations of the outer isophotes were avoided by visually inspecting all the images: when the disk (identified with spiral arms, rings, and lenses) is clearly more inclined than suggested by the outermost isophotes of the image, the disk isophotes were used for the estimate of galaxy orientation. For nearly face-on galaxies, the possible stellar halos are more difficult to distinguish, but in these cases the involved error in the orientation is less important. The final P4 axial ratios and position angles, center locations, and sky background values are listed in Table I. For each galaxy we also include a flag indicating the inclination uncertainty: 'ok' indicates that outer isophote axial ratio should give a reliable estimate of i_{disk}, 'u' indicates that the inclination is uncertain, while 'z' that the galaxy is close to edge-on.

A scatter plot of P3 orientation parameters versus HyperLeda values is presented in Fig. 4 (upper row). The P4 axial ratios are on the average closer to unity than those in Hyperleda, though the difference is not very large (median $(b/a)_{P4} - (b/a)_{HyperLeda} = 0.024$). On the other hand the standard deviation of the difference is quite large (~ 0.1). Fig. 4 also contains a comparison to P3 isophotal orientation parameters (Munoz-Mateos et al. 2014) which correspond to a fixed surface brightness level $\mu_{3.6} = 25.5 mag/arcsec^2$. On average, P4 orientations are measured at about 0.9 times this distance. The scatter is now significantly reduced and no systematic difference is seen.

Since we are fixing the disc orientations in the decompositions it is important to check

[3]This expectation is of course not valid for a vertically extended (say $T \leq 0$) galaxy disk, nor in the case of intrinsically non-circular disks. However, the fitted GALFIT expodisk-function assumes an infinitesimally thin intrinsically axisymmetric disk, so any other treatment would be inconsistent in the decompositions

the consistency of our inclinations. Figure 5a displays the histogram of the P4 axial ratios for Hubble types $-3 \leq T \leq 10$. In case of randomly oriented sample of thin disks, the distribution of b/a should be flat. In case of finite thickness a drop would be expected near a lower limit $b/a = q_i$, where q_i is the intrinsic aspect ratio of the galaxies. According to Fig. 5a such a drop is evident for $b/a \lesssim 0.15$. However, overall the sample contains an *excess* number of galaxies with small axial ratios. Similar trend is seen also when using the HyperLeda axial ratios (Fig. 5b) or P3 isophotal orientations (Fig. 5c). A possible explanation for the excess of small b/a ratios is that the S4G sample has been selected (Sheth et al. 2010) using an inclination-corrected blue magnitude limit ($BT_{corr} = 15,5$): if this dust correction is exaggerated, say for very late types, it would lead to an excess of faint, highly-inclined galaxies. This explanation is supported by the solid curves in Fig. 5 which display the histograms when limiting to galaxies with non-corrected $BT < 15$: now the histogram of P4 values is quite flat. The histogram for P3 isophotal axial ratios is rather similar, though there are somewhat fewer small $b/a \lesssim 0.2$ values. This could be due to the above-mentioned faint stellar halos: in case of nearly edge-on galaxies a fixed surface brightness level could pick up the rounder faint outer envelopes, whereas in P4 we have in such cases tried to trace the disk isophotes. On the other hand, compared to both P3 and P4, the HyperLeda distribution has a deficit of large axial ratios.

It is interesting to compare our sky background estimates to those in P3. In P3 an automatic sky measurement is made using 45 sky regions with 1000 pixels each. The regions are chosen close to the distance $2R_{25}$ from the galaxy center (R_{25} is the blue band isophotal radius from HyperLeda; if needed the distance of sky regions is modified manually). According to Fig. 6 there is a very good agreement in the estimated sky backgrounds between P3 and P4 (see the right frame which takes into account that different P1 mosaics are used for some of the galaxies). This is remarkable as the measurements are made completely independently and with different methods. The median difference between

the determinations (0.0006 Mjy/sr) is only about 1% of the typical sky background value, and its standard deviation (0.003 MJy/sr or) is comparable to the magnitude of global sky variations in both sets of estimates (see Fig. 7). However, the figure also reveals some cases where the difference between P4 and P3 is significant: inspection of the images indicates that this is due to a bright star (NGC1055), a nearby interacting component (NGC3327, NGC4647), or a too small FOV (NGC2655). In two cases (NGC1300, UGC10288) the final P1 mosaic used by P3 is much improved over the earlier version used in P4.

Fig. 7 compares our sky background variation estimates ('DSKY' denotes global variations between sky measurement regions and 'RMS' the average of the locally determined rms-scatter) with the corresponding estimates in P3 (ESKY1 and SSKY1, respectively). There is a good overall agreement in the level of estimated global variation (left frame): the somewhat larger values for P4 are likely to follow from the larger range of radii we used for the sky measurement regions compared to P3. Also the local sky rms values show good agreement (right frame). In Section we will use these P4 RMS estimates for assessing the theoretically calculated sigma images.

2.2.4. Input data images

As input for GALFIT decompositions we use the the 3.6 μm images. Because all necessary data reduction and calibration were already done in P1, the main preparatory steps are to subtract the estimated sky background value and determine which image region to include in the decomposition. In principle, GALFIT can also fit the sky background. However, this requires that the decomposed image region contain sufficiently large regions free of galaxy light or other contaminants. Use of such large image regions would slow down the decompositions considerably. Even more importantly, the S^{4}G images often fill a substantial part of the raw frames or there are sudden jumps in the background levels

(well outside the galaxy). To have a control of where the sky level is estimated, we chose to do the sky background evaluation manually, as described in Sect. 2.2.3 and to limit the decomposition to the rectangular region $\pm R_{fit}$ around the galaxy center. In practice, we choose $R_{fit} = 1.3 \times R_{gal}$, where R_{gal} is the visually estimated outer size of the galaxy[4]. Finally, the image header keyword EXPTIME is set to 1 sec (as a default GALFIT will normalize the input data values with EXPTIME, which keyword is not relevant for P1 mosaics), and all *NaN's* (bad image values indicated with Not-a-Number value) are replaced with a constant value, and flagged in the mask in order to prevent them from affecting the decompositions.

2.2.5. Sigma-images

The sigma-images were calculated using the pixel values and header information in the 3.6 μm data images and the pixel values of the weight images. The images provided by P1 are in flux units (MJy/sr), and for the calculation of the noise the pixel values F are converted to the number of electrons N_e,

$$N_e = \frac{F + F_{bg}}{F_{conv}} \times T_{frame} \times N_{frames} \times g, \tag{8}$$

where F_{bg} is the zodiacal light background which has been subtracted from the frame by the automatic Spitzer pipeline (its value is given by the header keyword `SKYDRKZB`). Note that the flux F contains also the subtracted sky background ($F = F_{gal} + F_{sky}$. The F_{conv} is the

[4]Later comparison to P3 isophotal radii published in IRSA indicates that the median $< R_{\rm fit\ region}/R_{25.5} >= 1.7$, where $R_{25.5}$ is the Pipeline 3 isophotal radius at $\mu_{3.6}(AB) = 25.5$. The region is thus large enough to ensure that also the fainter outer parts are included in the fit.

conversion factor between flux units and original digital units (header keyword `FLUXCONV`, in units of MJy/sr per DN/sec), T_{frame} is the integration time/frame in seconds, N_{frames} is the number of combined frames for each pixel, and g is the detector gain factor (`GAIN` in units of e/DN). The number of frames combined is coded to the pixel values W of the weight images, $N_{frames} = W/10$. Note that $T_{frame} = 30$ sec must be used instead of the original integration time/frame given by the header keyword `FRAMTIME`: this is because during the compilation of P1 mosaics the pixel values have been normalized to this value regardless of the original T_{frame}[5]. The statistical uncertainty of each pixel is then calculated as a combination of Poisson noise (photon noise) and the readout noise of the detector (RON),

$$\sigma^2(N_e) = N_e + N_{frames} \times RON^2. \tag{9}$$

We use RON = 15.0, 14.6, and 21 electrons, for `FRAMTIME` = 12, 30, and 100 secs, respectively. Note that these values, communicated by Spitzer Science center helpdesk, deviate slightly from those given by the image header keyword `RONOISE`. The $\sigma(N_e)$ is then converted to the estimated uncertainty of the image flux

$$\sigma_{est}(F) = \sigma(N_e) \times F_{conv}/(T_{frame} \times N_{frames} \times g). \tag{10}$$

Figure 8 compares the theoretical noise estimate with the noise measured directly from the image. An average over all sky measuring boxes is used. In the left frame the measured RMS is plotted against the estimated σ_{est}. Colors distinguish between archive images from the cryogenic mission (original exposure time/frame either 12, 30, or 100 secs) and the new observations during the warm Spitzer mission (time/frame 30 secs, with total exposure time of 240 seconds). For the archive images the overall agreement is quite good: there is a practically linear trend $RMS \approx 0.9\ \sigma_{est}$ holding for all three frame times, with the largest

[5]This concerns the treatment of archival images; all warm mission S^{4}G observations had $T_{frame} = 30 secs$.

noise levels corresponding to the shortest frame times which have the largest contribution from the readout noise. The factor ~ 0.9 is probably due to the P1 mosaicking process, during which the images have been combined and sampled to 0.75 ″pixel size from the native pixel size of 1.2 ″. Because of this sampling the adjacent pixel values are strongly correlated, which is not taken into account in the theoretical estimate. Instead of trying to account in detail for the noise propagation during the mosaicking prosess we apply an empirical correction

$$\sigma_{decomp}(F) = 0.9\ \sigma_{est}(F) \qquad \text{(cryogenic mission =} \tag{11}$$

to be used in decompositions of cryogenic phase archival images.

For the warm mission the observed RMS is nearly 50% larger than the theoretical estimate (Fig. 8), indicating the presence of some extra source of noise. Following the advice of Spitzer Science Center helpdesk, we include an extra noise component (σ_{conf}), which is added quadratically to the noise estimated above. To account for the P1 mosaicking, the above factor of 0.9 is again included. We thus adopt

$$\sigma_{decomp}(F) = 0.9\ \sqrt{\sigma^2{}_{est}(F) + \sigma^2_{conf}} \qquad \text{(warm mission)} \tag{12}$$

for the warm phase images. The empirical correction σ^2_{conf} is estimated by this same formula when applied to the sky measurement regions.

Figure 9 illustrates the magnitude of different contributions to the sky background noise. For the archival images (cryogenic phase) the background is dominated by the readout-noise, though the contribution due zodiacal background light (the SKY we have subtracted + the SKYDKZD subtracted during automatic Spitzer pipeline) still has a noticeable contribution. For the warm phase the extra confusion noise term is even larger than the readout contribution. Fig. 10) compares the relative importance of the shot noise (Poisson) due to galaxy flux to the background noise, for different surface brightness

levels. The two horizontal lines indicate the typical background noise levels for the cryo (lower) and warm (upper) missions. The figure also illustrates how the σ-map looks for the galaxy NGC3992 (observed during warm mission). Near the center ($\mu \approx 17$), the shot noise completely dominates, though already in the bar region ($\mu = 20 - 21$ both contributions are important.

In principle, the obtained σ^2 is just a statistical estimate of the true underlying variance at each pixel. We did some experimentation by smoothing the *sigma* -images (median averaging with kernels amounting up to 20 pixels). Except in the case of a few galaxies with very centrally peaked light profiles, this smoothing had very little influence on the decomposition parameters. For the galaxies where smoothing played a role, the derived parameters were in any case uncertain (for example, the bulge Sérsic index obtained unrealistically high values > 10). In the end, we decided to apply no smoothing at all.

2.2.6. PSF-image

The IRAC data is not very well sampled: its native pixel resolution is $1.2''$, which is close to the Gaussian spread of a point source observed at channel 1. As discussed in detail in Peng et al. (2010), in such a case an oversampled PSF should be used. The IRAC PSF has also wide wings (see Fig. 11), so that a relatively large convolution box size must be used in decompositions: we set this to $40'' \times 40''$ (in some cases with a very centrally peaked light profile this region was extended to $150'' \times 150''$ with considerable increase in CPU time). Note also that IRAC PSF depends slightly on the instrument orientation. Therefore, in principle a separate PSF should be used with each image, determined from point sources in the same frame, or a combination of appropriate PSFs, in case the final image is a combination of several images obtained at different times. Clearly, such a procedure would be very time consuming. Fortunately, such an accuracy is hardly needed

in our decompositions. The common oversampled PSF provided by T. Jarret was used for all images, made as a composite over several instrument rotation angles. Fig. 11 displays the PSF, as well as a Gaussian profile (with $FWHM = 2.1$") approximately matching the core of the composite PSF. Also shown is an azimuthally averaged profile of the composite PSF. It will be shown in Section 2.5 that it is important to account for the central core, as well as for the nearly circular wings of the PSF, whereas the outermost spikes have less importance for the obtained decomposition parameters.

Table 1. Pipeline 4 parameters: galaxy center, outer orientation, and sky background

IDE	MODEL	xc	yc	PA ± dPA	ELL ± dELL	RANGE	SKY	DSKY	RMS	FLAG
ESO011-005	bz	780.84	299.02	42.7 ±0.1	0.747 ±0.002	18.0 - 22.0	0.0125	0.0039	0.0109	z
ESO012-010	dbar	760.68	294.95	146.2 ±1.1	0.542 ±0.012	100.0 - 120.0	-0.0022	0.0025	0.0109	ok
ESO012-014	dbar	782.57	459.99	31.0 ±5.2	0.580 ±0.040	90.0 - 100.0	0.0080	0.0033	0.0106	u
ESO013-016	ndbarf	478.49	282.78	-14.3 ±3.1	0.343 ±0.031	70.0 - 110.0	0.0041	0.0027	0.0101	ok
ESO015-001	dbar	291.43	294.80	125.7 ±2.7	0.586 ±0.018	75.0 - 100.0	0.0050	0.0018	0.0102	u
ESO026-001	ndbar	795.50	495.47	19.3 ±21.1	0.060 ±0.028	70.0 - 80.0	0.0125	0.0024	0.0105	ok
ESO027-001	bdbar	776.34	294.63	12.5 ±10.1	0.216 ±0.061	150.0 - 170.0	0.0109	0.0032	0.0112	u
...										
UGC12791	d	295.88	289.63	82.6 ±1.4	0.709 ±0.037	60.0 - 80.0	0.0406	0.0033	0.0110	ok
UGC12843	-	290.20	287.90	17.5 ±3.9	0.553 ±0.058	70.0 - 90.0	0.0418	0.0037	0.0105	u
UGC12846	d	571.15	851.20	-4.7 ±14.0	0.127 ±0.031	80.0 - 90.0	0.0446	0.0007	0.0019	u
UGC12856	dbarn	291.07	296.89	16.9 ±1.5	0.615 ±0.049	65.0 - 100.0	0.0401	0.0025	0.0111	u
UGC12857	zzn	284.91	280.12	33.5 ±0.2	0.760 ±0.009	20.0 - 40.0	0.0453	0.0018	0.0110	z
UGC12893	bd	294.93	283.15	87.2 ±3.8	0.131 ±0.039	70.0 - 90.0	0.0463	0.0022	0.0110	ok

Note. — Galaxy center x_c, y_c is given in pixels, $ELL \pm dELL$ and $PA \pm dPA$ are the outer isophote ellipicity and position angle together with their standard deviations in the measurement range, given by $RANGE$ (in pixels). SKY, $DSKY$, and RMS give the estimated sky level and its global and local variation (in MJy/sr), $FLAG$ indicates whether the inclination can be reliably estimated from the ellipticity ($i_{disk} = \cos^{-1}(1 - \epsilon_{outer})$): ok = reliable, u = uncertain, z= nearly edge-on galaxy.

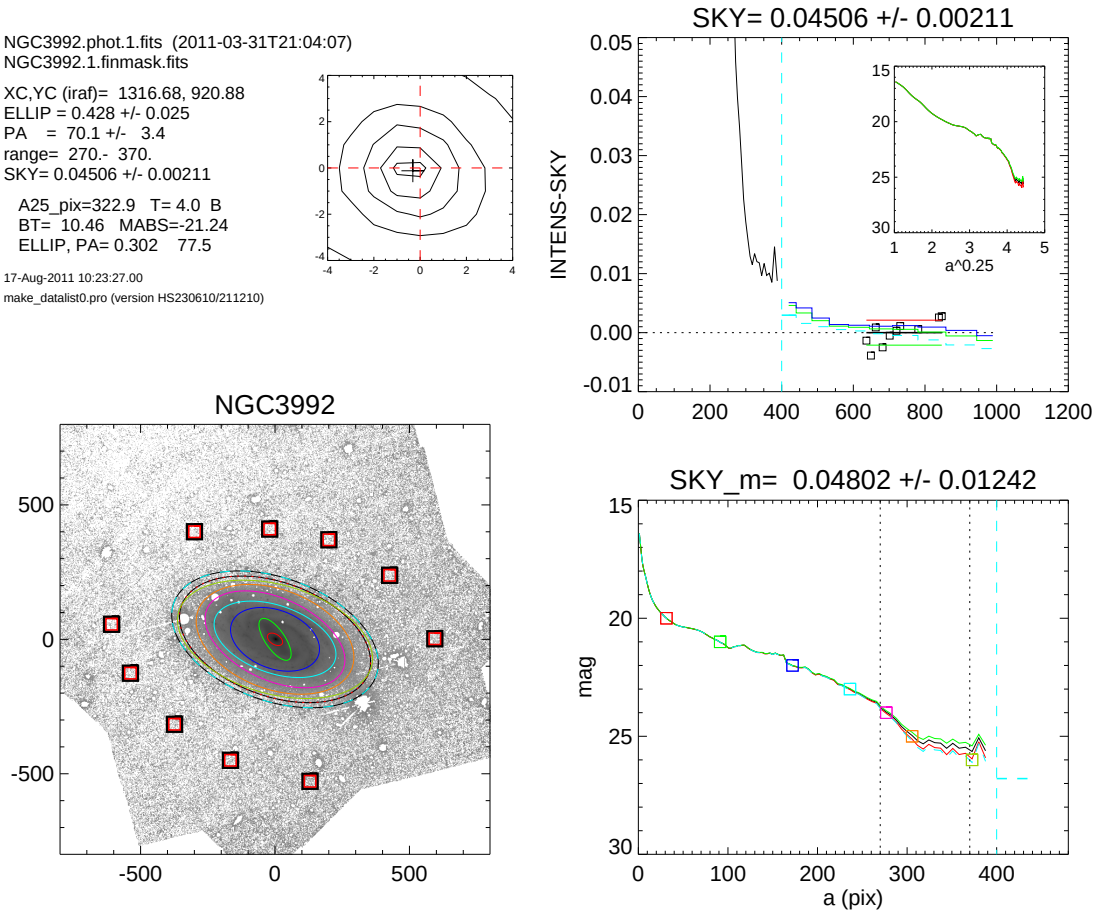

Fig. 1.— Example of the determination of sky background for NGC 3992. The small **upper left** frame illustrates the center location found with *cntrd*-routine (black cross) relative to the image isophotes near the center (dashed red lines indicate the nearest integer pixels). In the **lower left** frame, red boxes indicate the local regions used for estimating the sky background: the mean and the RMS of these local median values were adopted for the sky background and its uncertainty (SKY and DSKY, respectively). The dashed ellipse indicates the visually estimated galaxy size (R_{gal}). The white specks indicate masked stars. The **upper right** frame shows the intensity profile after subtracting the SKY value (indicated in the title of the plot; note the linear scale, intensities are from IRAF *ellipse* fits), marking also the $\pm DSKY$ (vertical red/green lines) and the median sky values in local measurement regions (boxes). The vertical dashed line corresponds to R_{gal} The insert shows the same profile, but as magnitude versus $a^{0.25}$, where a is the isophotal major-axis distance: de Vaucouleurs profile would appear a straight line in this plot. The **lower right** frame shows the intensity profile in magnitude units (AB-magnitudes): red/green profiles correspond to adding/subtracting DSKY to the sky background. The title indicates an alternative sky estimate made fully automatically with IDL Astro library's *mmm*-procedure; this was not used except as a rough check. All distances are in pixels (0.75″). Similar plots for all sample galaxies are given in the P4 web site

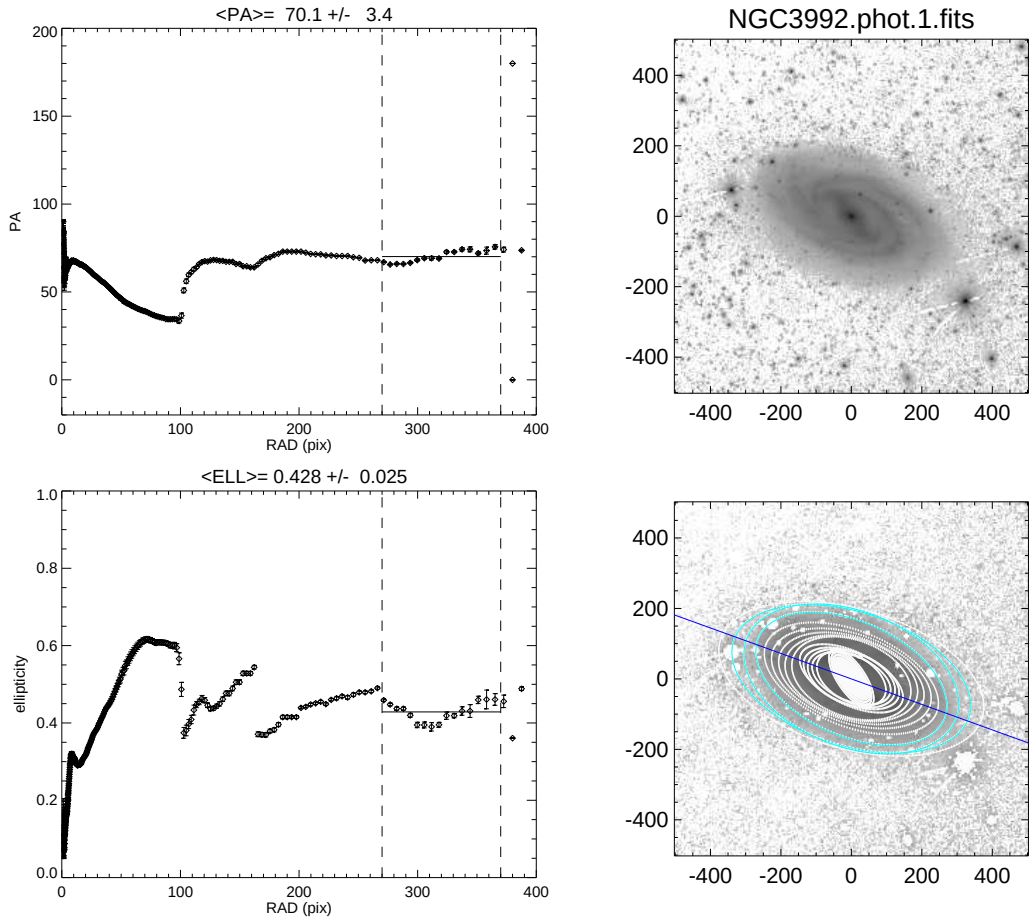

Fig. 2.— Example of the isophotal profiles derived for NGC 3992 using iraf *ellipse* routine. The plots in the left display the PA and ellipticity profiles versus semimajor axis (a) of isophote ellipse: the dashed vertical lines indicate the range used in estimating the outer disk orientation parameters; solid vertical line indicates the mean over that range. The upper right plot shows the observed, sky subtracted image, clipped at $1.3 \times R_{gal}$ (the image region used in decompositions). In the lower right the isophotes are plotted on top of observed (masked) image: the light blue isophotes correspond to the a range from which the outer disk orientation ($\epsilon_{outer}, PA_{outer}$) was derived; dark blue indicates the assigned PA_{outer}. Similar plots for all sample galaxies are available in the P4 web site.

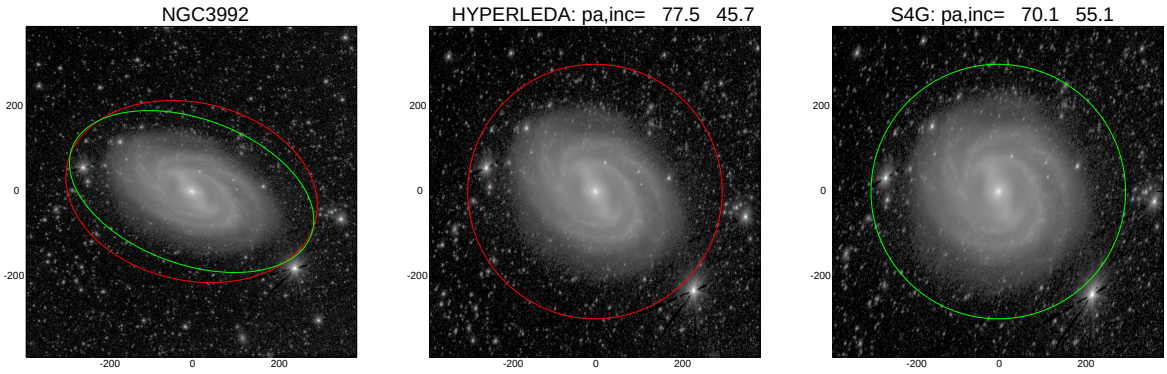

Fig. 3.— Example of deprojections with HyperLeda and P4 orientation parameters ($(b/a)_{outer}$ and PA_{outer}) for NGC 3992. The red and green ellipses on the original image in the left illustrate the HyperLeda and P4 parameters, respectively (semimajor axis of the ellipse equals R_{gal}), the frame in the middle shows the deprojection with HyperLeda orientation, and that in the right with P4 parameters: here the inclination is taken simply as $i = \cos^{-1}(b/a)$ (note that this differs from the inclination ("incl") listed in HyperLeda, which includes a morphological type-dependent correction for the assumed disk thickness). Clearly, the face-on disk is closer to axisymmetric when using P4 parameters: the difference would remain if the thickness-corrected HyperLeda inclination were used (47 degrees for this example). Similar plots for all sample galaxies in the P4 web site.

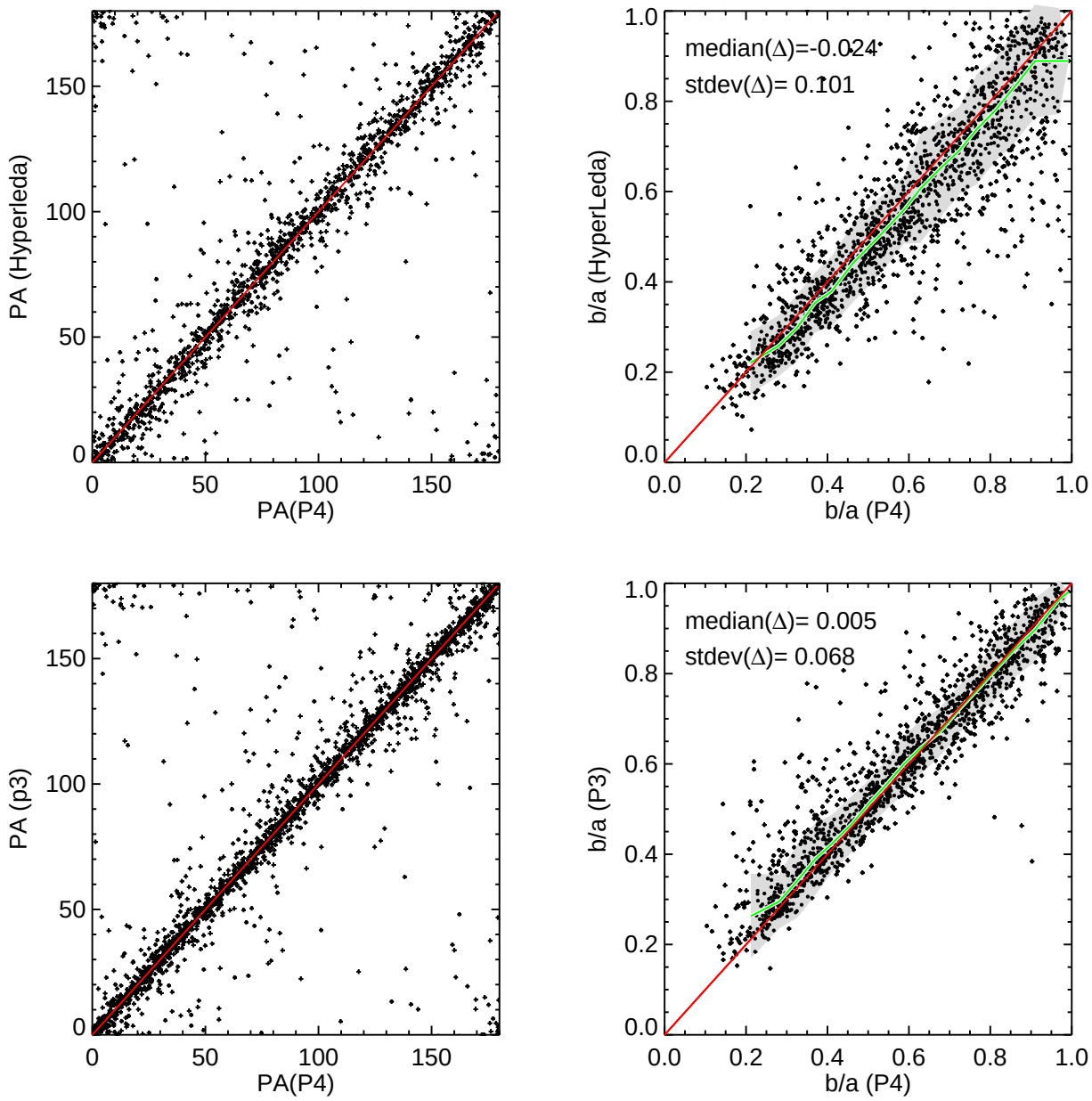

Fig. 4.— Upper frames: Comparison of derived outer disk orientation parameters with those in HyperLeda. In the left the position angles, and in the right, the axial ratios b/a. The green line in the right hand plot indicates the running median of HyperLeda axial ratio, calculated in bins of 100 galaxies; gray indicates the RMS scatter in the bin. Red line indicates unit slope. The labels give the median difference and rms between Hyperleda and P4 for the whole sample: P4 axial ratios are generally larger than those in HyperLeda. The lower frames show a similar comparison to the orientation parameters at the $\mu_{3.6} = 25.5\ mag/arcsec^2$ isophote calculated in P3.

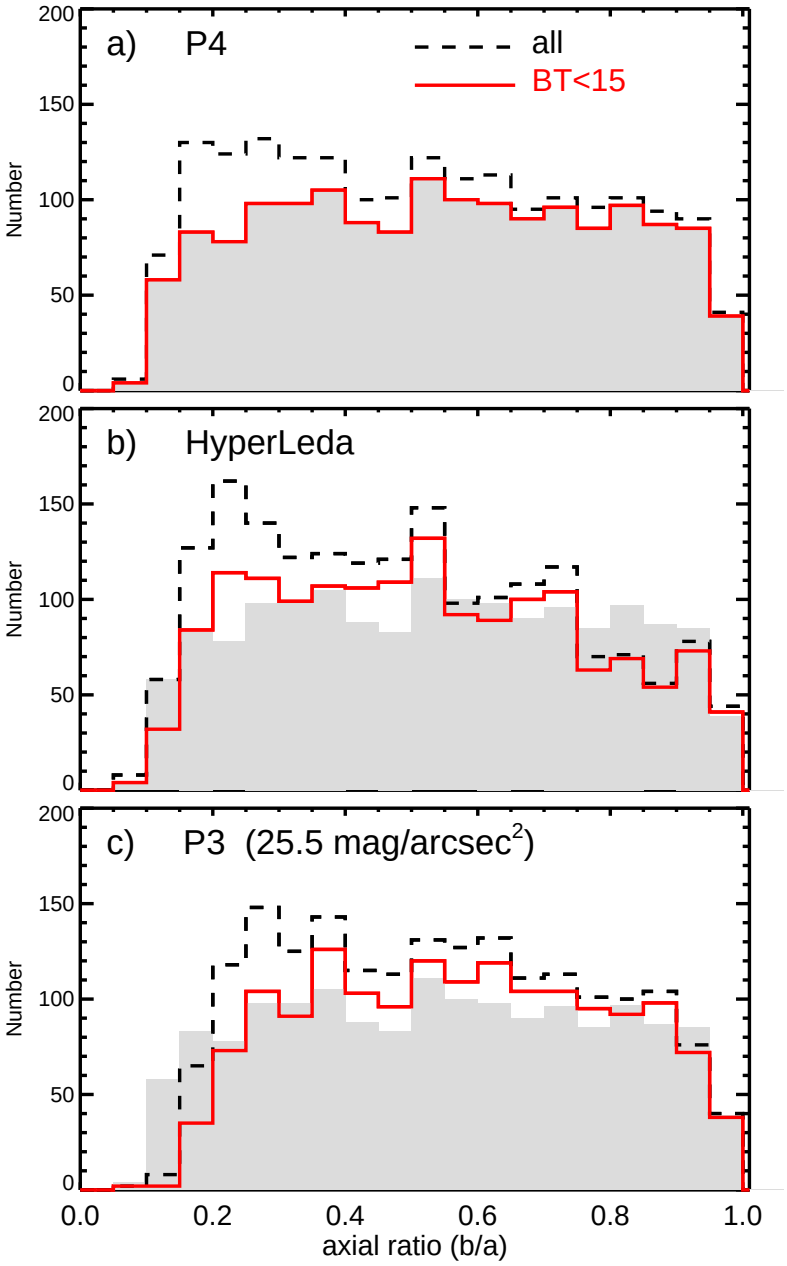

Fig. 5.— Distribution of axial ratios, calculated with P4 (a), HyperLeda (b), and P3 orientation parameters. Hubble types $T \leq -4$ and $T > 10$ are excluded. Dashed line indicates the whole S4G sample, with the magnitude selection $BT_{corr} < 15.5$, where BT_{corr} is the inclination-corrected blue magnitude from HyperLeda. Solid line corresponds to a similar limit, but using non-corrected blue magnitude BT. To ease the comparison the P4 histogram for $BT < 15$ is shown as the shaded region in each frame.

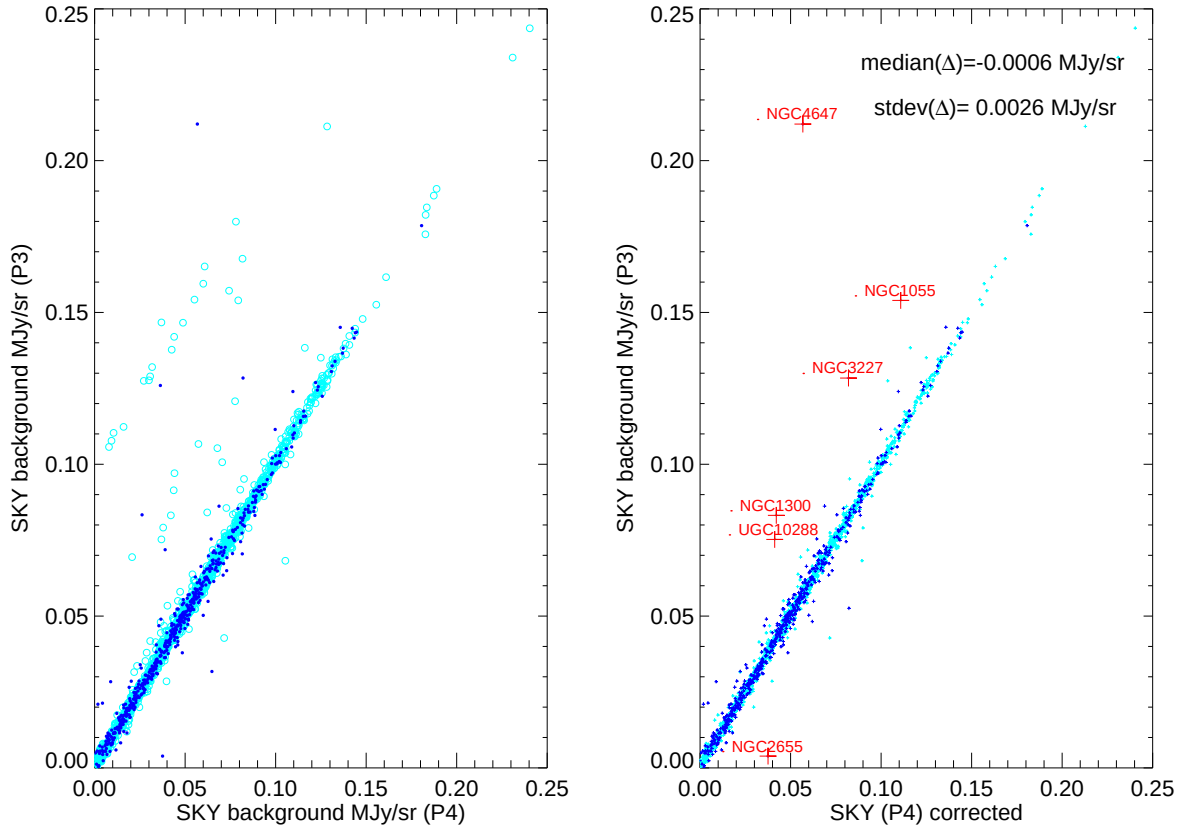

Fig. 6.— The left frame displays the used P4 sky background estimates (SKY) in comparison to P3 (Munoz-Mateos et al.; variable 'SKY1'). The large apparent differences are due to use of different versions of P1 mosaics. In the right we have corrected the P4 values to corresponds to the final P1 mosaics (=those used in P3). Excluding the few deviant cases (discussed in the text) the median difference between P3 and P4 is 0.003 Mjy/sr. Light and dark blue symbols indicate observations during cryogenic and warm phases, respectively.

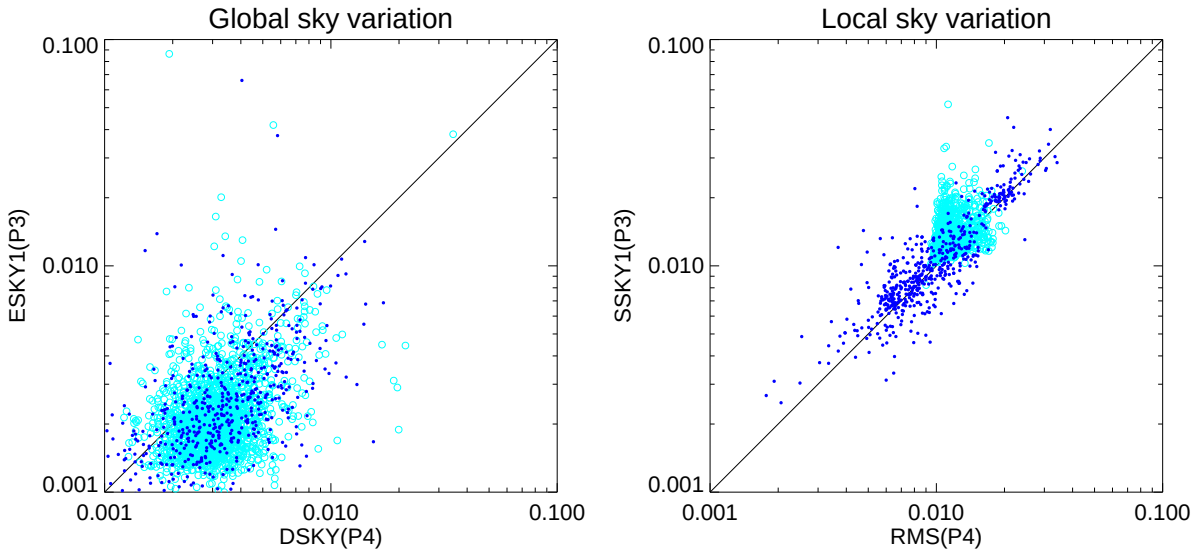

Fig. 7.— Comparison of P4 and P3 sky variation estimates. The left frame displays the global variations, estimated from the standard deviation of sky measurements at different areas (variable 'DSKY' in P4 and 'ESKY1' in P3; the symbol colors are the same as in the previous Figure). In the right the local variation, estimated from the median scatter of sky values in local measurement areas (variable 'RMS' in P4 and 'SSKY1' in P3).

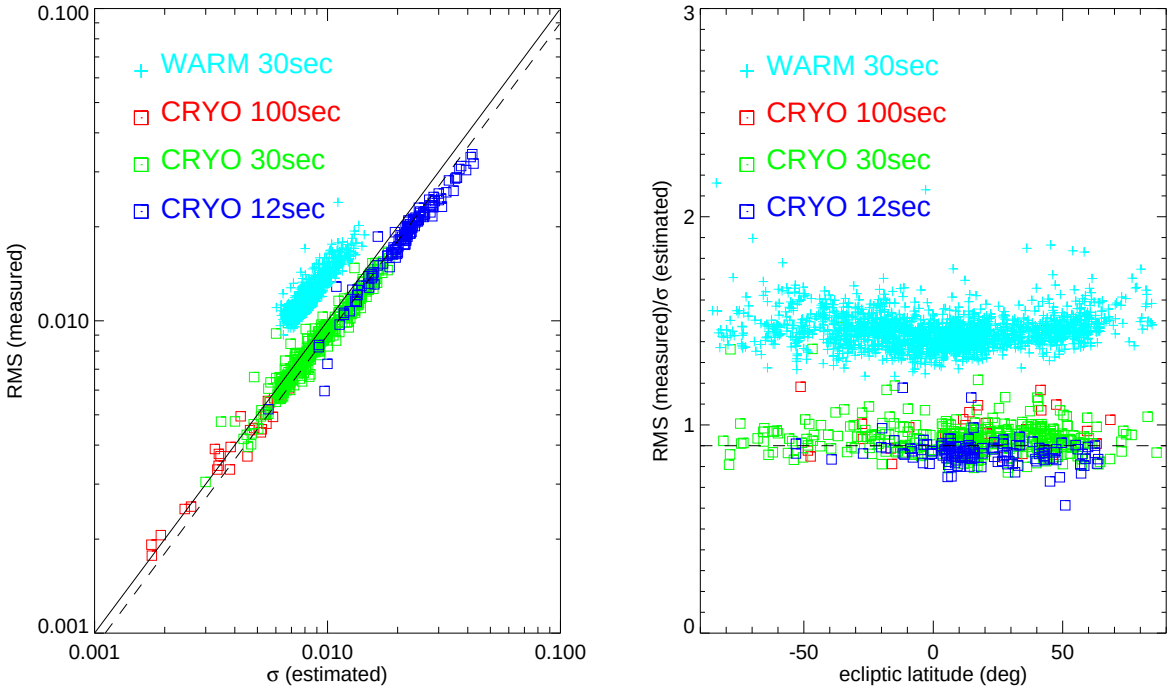

Fig. 8.— The left frame displays the relation between measured RMS in sky regions and the estimated σ taking into account the read-out noise, and the Poisson noise due to sky background (including the zodiacal light contribution removed by automatic Spitzer pipeline). For the cryogenic mission phase the agreement is fairly good, with $RMS \approx 0.9\ \sigma_{est}$ (indicted by the dashed line; solid line indicates a one-to-one correspondence). For the warm phase the observed RMS is about 50% larger than the theoretically estimated noise. The right frame shows the ratio of the observed and estimated noise as a function of ecliptic latitude.

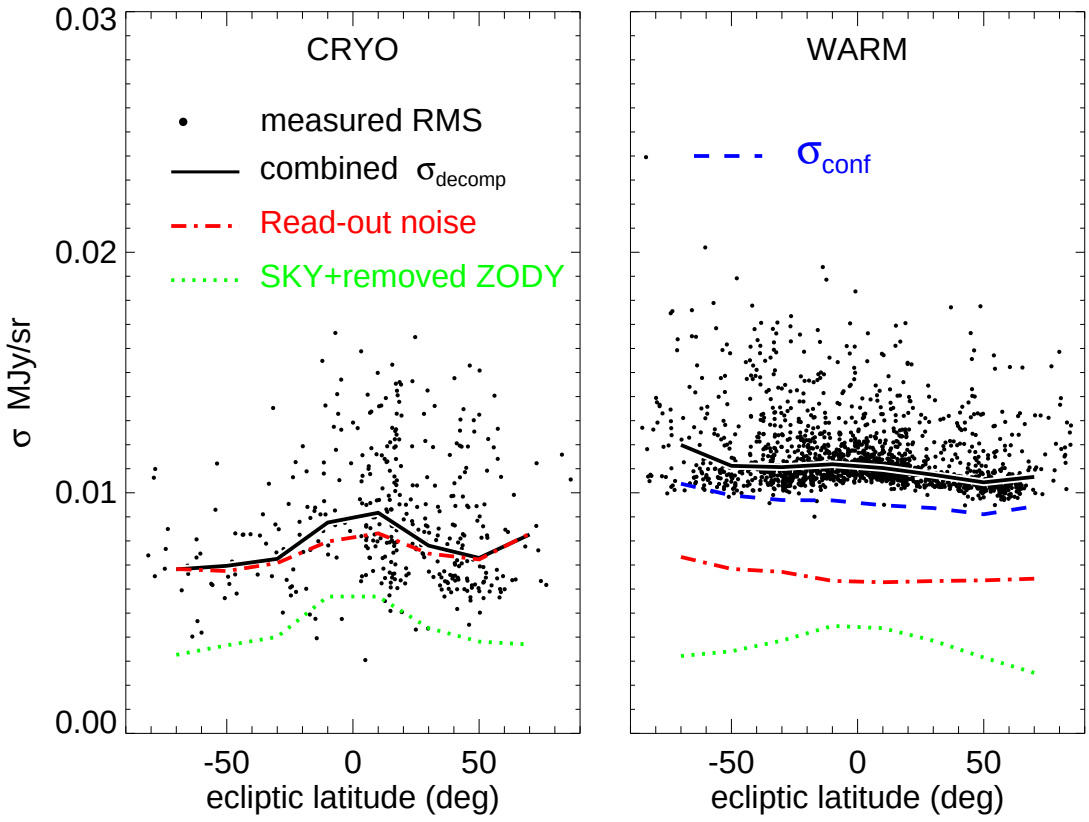

Fig. 9.— Different contributions to the sky background noise. The symbols indicate the measured average noise in sky measurement regions (RMS) in warm phase archival images (CRYO; for clarity only those with 30 sec original frame time are shown) and in warm mission images, as a function of ecliptic latitude. The lines indicate various noise contributions: for clarity a mean over 20 deg bins is shown. Note that in the left frame the peaking of readout noise contribution close to ecliptic plane is just a spurious effect: these archival images happen to have on average a smaller total exposure time (smaller N_{frames}).

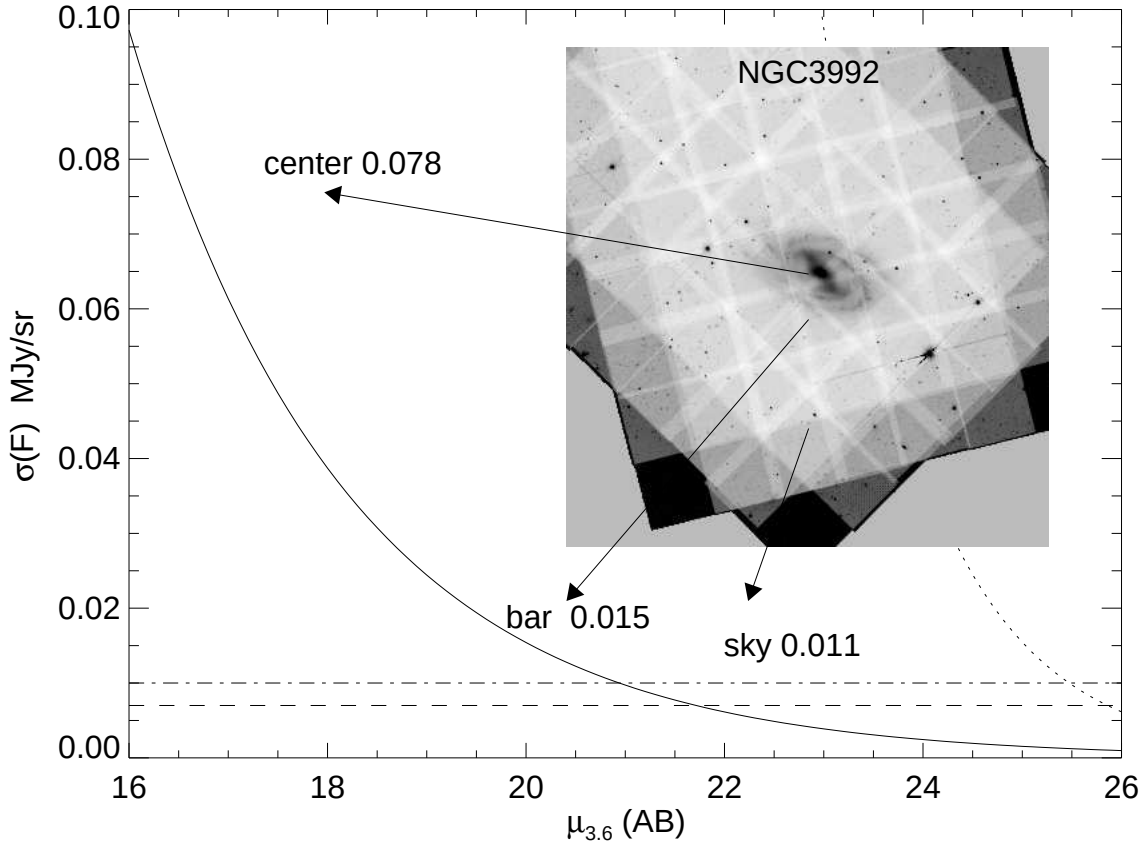

Fig. 10.— Comparison of Poisson and background noise contributions. The solid curve is the calculated σ due to Poisson noise associated with galaxy flux as a function of surface brightness, and the horizontal lines indicate the typical background contributions for warm and cryo missions (dot-dashed and dotted lines, respectively; they include both the noise associated with sky background flux +instrumental contributions). The insert shows the *sigma*-map for NGC 3992. The structure in the background is due to different number of frames covering each pixel. Also notice how the galaxy stands clearly on the *sigma*-map.For comparison, the dotted line crossing the horizontal lines at $\mu_{3.6} \approx 25.5$ indicates the galaxy flux in Mjy/sr.

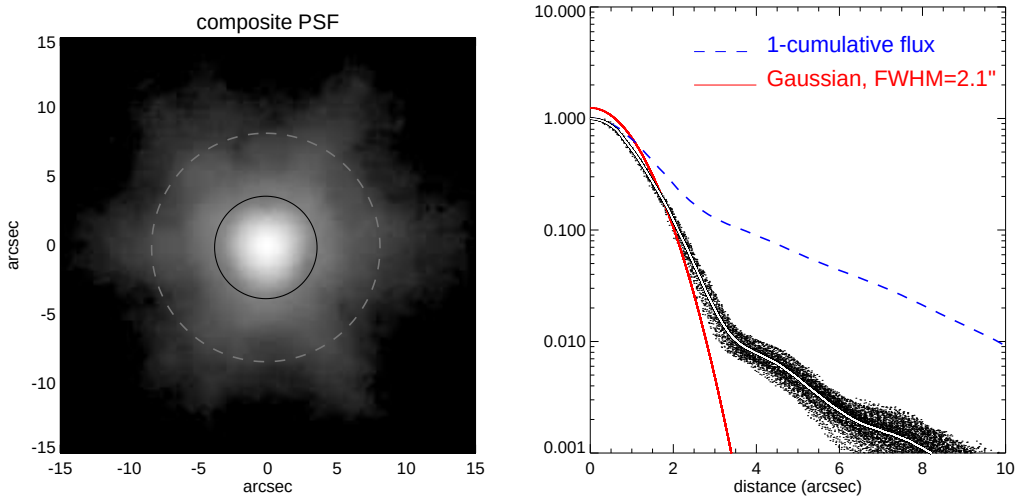

Fig. 11.— The composite PSF used in decompositions (shown in log-scale to emphasize the wings: in the right the PSF is normalized to its maximum value). The red solid curve indicates a Gaussian with the same FWHM=2.1, approximately matching the inner part of the actual PSF (black symbols). The white curve indicates an azimuthally symmetrized version of the composite PSF. The dashed curve indicates the cumulative flux outside a given distance from the center: the solid and dashed circles in the left, with radii 3.7″ and 8.3” indicate the regions where 90% and 98% of the flux is concentrated (50% of flux falls within 1.3″). The composite PSF, oversampled with a factor of 5 (pix-size 0.15 arcsec) was provided by Tom Jarrett.

2.3. Generation of input files for GALFIT decompositions

The (ascii) input file for GALFIT specifies the galaxy data, mask, sigma, and PSF fits-files, and the region of the data image used in the decomposition. It also lists the components/functions used in the decomposition model, the initial guesses for the parameters, which of the parameters will be kept fixed, and which are iteratively varied in order to minimize the χ^2. After convergence to a final solution, the final parameter values are written into an output file, with similar format as the input file. If needed this output file can thus be used as an input for a new iteration (see Peng et al. 2002, 2010 for details).

The input file also specifies how to convert the image values to magnitudes. The data images from P1 are in flux units (MJy/sr). A conversion from pixel values F_i to (AB) surface brightness and integrated magnitudes is done with the formulas:

$$\mu_{3.6} = -2.5 \log_{10} F_i + 5 \log_{10} pix + zp \quad (13)$$

$$mag_{3.6} = -2.5 \log_{10} \sum_i F_i + zp, \quad (14)$$

where $pix = 0.75''$ and the zeropoint at 3.6 μm is $zp = 21.097$ (P3). Values of pix and zp are inserted into GALFIT input file.

All P4 input files for 1-component (Sérsic) and 2-component bulge+disk (Sérsic+exponential) decompositions were generated automatically. Similarly, the multi-component decompositions template files were created, which contained, in addition to bulge and disk components, entries for a Ferrers-bar, and a central unresolved PSF-component. The user then manually choose which components are fit and which functions used in the final model (see Sect 3 for more details). In all our decompositions we keep the centers of the components fixed to the galaxy center. The cases were this is clearly not appropriate (galaxies with off-center bulges) are noted in the parameter files.

1. In *1-component* input files initial guesses are needed for five free parameters: the

Sérsic index n, effective radius R_e, total magnitude m, isophotal minor-to-major axial ratio q, and position angle PA. The starting values of m and R_e were estimated from the data (m_{image} and R_e(image), respectively), for Sérsic index $n = 2$ is inserted as an initial guess, and q and PA were set to arbitrary values (0.9 and 10°, respectively). We thus avoided using the measured outer isophotes, to force GALFIT to search through a wider parameter space while minimizing the χ^2. Typically 1-component fits converged after 10-20 iterations. When the fit did not converge, or if the final parameters were nonphysical (say, $n > 10$, $q < 0.05$, very large or small R_e), a new decomposition was started manually with new initial guesses. Usually this did not lead to any improvement, indicating that GALFIT is indeed very efficient in avoiding spurious local minima.

2. The *2-component* bulge-disk models apply a Sérsic-function for the bulge: they thus need guesses for the same Sérsic parameters as before, except that now these refer to the central component. Accordingly, we used the initial guess R_e (bulge) = 0.5 $\times R_e$ (image) and $m_{bulge} = m_{image} + 1$. For the disk we use either *'expodisk'* or *'edgedisk'*-function, depending on the estimated galaxy inclination. In case of low or moderate inclination $b/a \gtrsim 0.2$ (corresponding to $i \lesssim 80°$), we use the '*expodisk'* function, which needs two free parameters, the scale length (h_r) and the integrated magnitude of the disk, m_{disk}. We chose $h_r = 0.25 \times R_{gal}$ and $m_{disk} = m_{image} + 1$, thus starting with a model with fairly massive and extended bulge. The disk orientation was fixed to the shape of the outer isophotes determined from the image (see Sect 2.2.3). In case of nearly edge-on disk, $b/a \lesssim 0.2$, we use the *'edgedisk'* function with four free parameters: the central surface brightness μ_0, radial scalelength h_r, vertical scalelength h_z, and the position angle of the disk. The first guesses are $\mu_0(disk) = \mu_0(image) + 3$, h_r as for the expodisk-model, while $h_z/h_r = 0.1$. Position angle is left free, with PA_{outer} as an initial guess.

3. In the template files for the *multi-component* fits the initial bulge and disk

parameters are set as for the 2-component models. For the Ferrers-bar the free parameters are the surface brightness at the effective radius of the bar, μ_e, its outer truncation radius R_{bar} (denoted with r_{out} in Eq. (7)), axial ratio, and position angle. As initial guesses we choose μ_e (bar)=μ_e (image)+3, $R_{bar} = 0.25 \times R_{gal}$, $q_{bar} = 0.5$, and $PA_{bar} = PA_{disk} + 90°$. For the magnitude of the unresolved central component we used $m_{psf} = m_{image} + 5$. However, in practice we typically modified these pre-inserted template values even before starting the search of the final model, for example by adopting the *output* parameters from 2-component decompositions for the disk and bulge.

2.4. Visualization of GALFIT decompositions: GALFIDL Package

In its standard use, GALFIT is executed from the operating system command line, with an input file argument. This input file lists the needed data files and the initial guesses for the parameters, as described above. The final decomposition parameters are written to an output file with a fixed name `galfit.NN`, where `NN` is a running number. Optionally, GALFIT makes a fits file containing the clipped data image (OBS; includes the region chosen for the fit), and total PSF-convolved model (MODEL), and the OBS-MODEL residual. Another GALFIT option is to write a fits file containing model components in separate fits extensions.

We have used GALFIT via GALFIDL, which is a set of IDL routines designed for easy visualization of the output from GALFIT decompositions. In addition, GALFIDL includes wrapper routines for calling GALFIT from inside IDL, with the advantage that the GALFIT output files and the produced plots are automatically renamed in a systematic fashion, using the names of the input files. We have utilized this by coding the galaxy identification and decomposition model components to the name of each produced output file (see Appendix A)

The visualization options in GALFIDL follow those of the BDbar-decomposition program we have earlier developed for the NIRS0S survey (Laurikainen et al. 2005), the most central of which is displaying a 2D plot of surface brightness vs. distance from the galaxy center (see Fig. 12). The advantage of this, compared to the more commonly used azimuthally averaged profile, is that the contributions of different model components, with different apparent ellipticities, are easily highlighted (Laurikainen et al. 2005; see also Gadotti 2009). The other visualization options include OBS-MODEL residual plots, profile cuts along a constant PA, comparison to observed profiles along isophotal major axis produced by IRAF ellipse, and plots showing the schematically different components included in the decomposition. The next section illustrates our decomposition strategies in more detail, concentrating on 2D-profiles. Additional plot types are illustrated in Appendix B, which describes the output released through P4 web page for all S^4G galaxies.

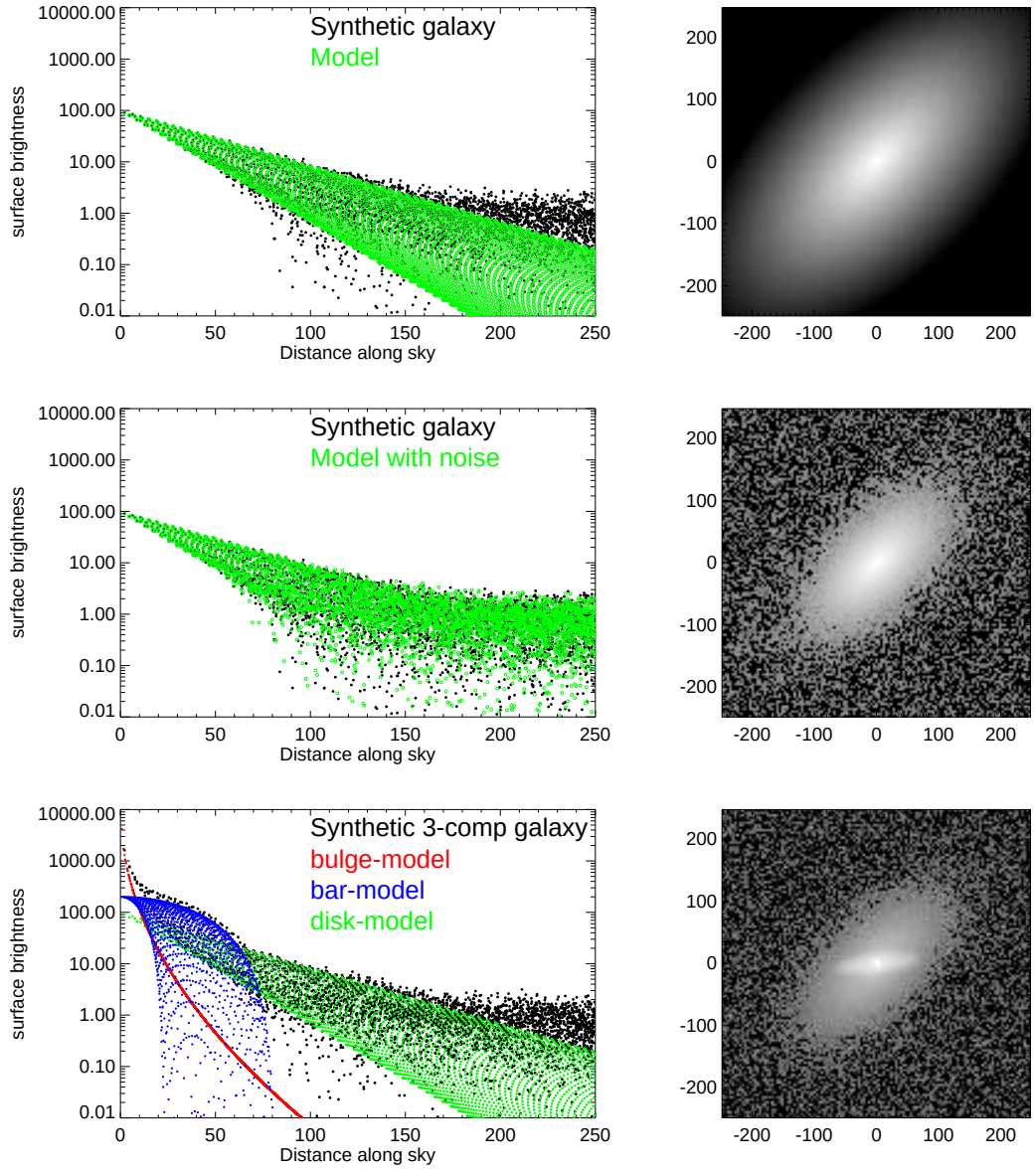

Fig. 12.— Schematic example of the 2D-profile plots. The black dots in the upper left frame show a synthetic observational image (exponential disk with added Poisson noise): the surface brightness (in arbitrary units) is plotted as a function of distance along the sky plane. The green dots indicate the best fitting GALFIT *expodisk* model; the width of the wedge-shaped profile depends on the disk inclination (here $i = 60°$). Note that this plot might leave an impression that the outer disk is not properly fitted: this illusion is due to the noise distribution appearing skewed in magnitude plots. The middle left frame illustrates the same model, after realistic noise (measured from the synthetic image) has been added also to the model profile, giving a visual confirmation that the model indeed is successful. The images in the right indicate the fitted model without (upper frame) and with noise (middle). The lowermost frames display a fit to a synthetic galaxy (image in the right) composed of a Sersic-bulge (here $n = 2$, with circular isophotes), an exponential disk, and a Ferrers bar.

3. Building the final multi-component decompositions - examples

The final decompositions for S4G galaxies were done by fitting a maximum of 4 components. Typically the components were the bulge (*B*), disk (denoted either as *D* or *Z*, depending on whether *'expodisk'* or *'edgedisk'* function was used), bar (*bar*) and the nucleus (*N*), but could be any combination of these. The ingredients of the model are indicated by concatenating the designations of the components to the final model name: this same naming convention is used in the names of decomposition output files stored to IRSA (Appendix A).

In all final decompositions the orientation parameters of the outer disk were fixed and for Ferrers function α and β are fixed (α=2, β=0). All other parameters were left free for fitting. However, to find the structure components properly it was convenient to temporarily fix many of the model parameters at the beginning, and then release them one by one. For some galaxies, the length of the bar was kept fixed even in the final model. This was the case if GALFIT persistently gave a clearly incorrect bar length when compared to visual evaluation (in such a case the χ^2 minimization was attempting to fit some other feature than a bar).

Altogether over 20 different combinations of components were used in the final decomposition models; Table 2 collects an inventory of the main categories. This diversity of models is motivated by our desire to measure the bulge (if present) and the underlying disk parameters in a reliable manner. In (non edge-on) galaxies with two disks, the inner disk was fit either with an exponential or a Sérsic function, depending on the flattening of the profile. Small central components were fit with the PSF, indicated as *'N'* in the model names. However, because the S4G images do not resolve very small bulges, many of those structures, particularly in late-type spirals, might actually be small bulges, which typically contribute less than a few percent of the total flux.

Table 2. Main categories of final decomposition models.

	Disk: moderate inclination		1855
		BD	210
		BDbar	306
		ND	206
		NDbar	206
		Dbar	470
		DD	119
		D	361
	Disk: nearly edge-on		358
		BZ	54
		NZ	63
		Zbar	8
		ZZ	113
		Z	119
	Spheroidal:	B	24
ALL			2237

Note. — Final decompositions were made for 2237 galaxies: in case of low or moderate inclination (apparent $\epsilon \lesssim 0.8$; 1897 galaxies), the disk component was fitted with *expodisk*-function, while for nearly edge-on galaxies ($\epsilon \gtrsim 0.8$; 358 galaxies), the *edgedisk*-function was used. In models **BD** and **BZ**, a bulge component was identified besides a disk, and it was modeled with a *Sérsic-function*. These models *may* also contain additional disk components or unresolved central components (modeled with *psf*). The models **BDbar** include those bulge+disk systems which contained also a bar (modeled with *ferrer2*). In **ND** or **NZ** models the central component is modeled with *PSF* instead of *Sérsic*-function. This may represent either a true central point source or (more commonly) an unresolved bulge. The models **NDbar** include also a bar. The models **Dbar** and **Zbar** have no inner *Sérsic* or *psf*-components, but include a bar-component. They may also contain an outer disk component. The **DD** models contain both an inner and outer disk (and no bulge nor bar), while **D** models refer to pure disks. Similarly **Z** models apply a single *edgedisk*-function, while **ZZ** models contain both thin and thick disk-components.

Non-barred galaxies:

The decompositions were made starting from simple 1 and 2-component models, and then adding as many components as necessary. For non-barred galaxies the process leading to the final model was the following:

(1) Accepting the automatic 1-component model (single Sérsic) as the final model. This was the case for elliptical galaxies (see NGC 3962 in Fig. 13).

(2) Accepting the automatic 2-component bulge/disk decomposition as a final model. A typical example is NGC 3938 (Fig. 14).

(3) Adopting a bulge/disk model, after interactively finding modified initial parameters that converged to an acceptable final fit

(4) Adding a nucleus component or an inner disk (e.g. NGC 1357, Fig. 15) to the bulge/disk model.

(5) When the galaxy had no obvious bulge we started from a single exponential disk, and if necessary, a second disk and/or nucleus was added (see NGC 723, Fig. 16).

When the outer profile was affected by a possible stellar halo, the outermost part of the profile was not fit. The best model was vetted by looking at the original image, the residual image after subtracting the model, the 2D surface brightness profile, and the ellipticities of the structures. The value of final χ^2 was not used as a criteria in assessing the relative merits of the models (often a simpler final model was preferred even if a more complicated model would have yielded slightly smaller reduced χ^2). It has been shown by Huang et al. (2013) that many elliptical galaxies might be better fit with multiple Sérsic profiles, but such a detailed approach was not taken in this study, where the emphasis is in analysis of disk galaxies (Part 2). It is worth noticing that while using deep images like those in S^4G, in an automatic fit the bulge profile even in late-type spirals is easily degenerate with the

outer part of the disk. In automatic fits this may lead to an unrealistically large Sérsic n and R_e for the bulge, of which NGC 628 and NGC 1357 are good examples (Figs. **??** and 15). Care is needed even for later type disks with small bulges: for NGC 628 the B/T values in automatic and controlled fits are 0.21 and 0.06, respectively.

Barred galaxies:

For barred galaxies a similar approach was followed. NGC 936 (Fig. 17) and NGC 5101 (Fig. 18) are good examples demonstrating the importance of preventing the bar from mixing with the bulge flux. Adding a bar component to a simple bulge/disk model drastically changes the obtained properties of the bulge (for NGC 936 B/T drops from 0.46 to 0.19; for NGC 5101 from 0.62 to 0.22). NGC 5101 has also a type II profile in the disk break/truncation classification associated to a broad outer ring (Laine et al. 2014). Using the edge of the ring as a manifestation of a different flux distribution in the outer disk might be a bit misleading. Because of such ambiguities in the interpretation, we typically fit the type II disk profiles with a single exponential component. However, there are other barred galaxies in our sample, like IC 4901 (Fig. 19), in which two exponential components (+ Ferrers function for the bar) were used for fitting the disk. In this particular galaxy using two exponentials is necessary, and those clearly corresponding to distinct surface brightness components.

Pure disk galaxies:

A third main group of galaxies in our sample are those having no obvious bulge. They may have a single exponential disk (NGC 3377A in Fig. 20), or more than one disk components (NGC 723 in Fig. 16). The structure fit as an inner disk in NGC 723 consists of broad, prominent, and tightly wound spiral arms. Bulgeless galaxies may have bars, of which NGC 3517 (Fig. 21) is an example. To get an estimate for the scale length of the disk for these galaxies, the outer disks were always fit with an exponential function, even in

galaxies where the disk would have been better fit by a Sérsic function with n slightly less than unity. Generally, the assumption of an exponential disk is good, but there are also cases, like ESO026-001 (Fig. 22) in which a Sérsic function would actually be a much better choice.

Edge-on galaxies:

The models for the nearly edge-on galaxies were done assuming that the disk is viewed completely edge-on. Bulge, and in some cases also a bar or an additional disk were fit. In these models also the vertical thickness was an output parameter. However, these models are only tentative, and are meant solely as starting point for better, scientifically oriented decompositions. There already exists detailed modeling of edge-on galaxies in S4G, based on fitting their vertical profiles to hydrodynamical thin-thick disk models (Comerón et al. 2011, 2012)

The P4 models for the spiral galaxies are generally good, giving reliable estimates for the parameters like the bulge-to-total flux ratio (B/T), the scale lengths of the disk (h_r) and the central surface brightnesses (μ_0). However, despite the fact that up to four components were fit, the pipeline decompositions for the early-type disk systems (T<1), because of their complex structures, are often insufficient. These systems may have nuclear bars, ovals and lenses, which are not included in the models in any systematic fashion. Because of this, the B/T flux-ratios, particularly for S0 galaxies, can be over-estimated. Including all these structures would require even more complex decompositions, like those done in the near-IR by Laurikainen et al. (2005, 2006, 2009, 2010). Such time consuming modeling goes beyond the scope of P4 decompositions. Nevertheless, P4 decomposition output files provide good starting point for such fine-tuned modeling.

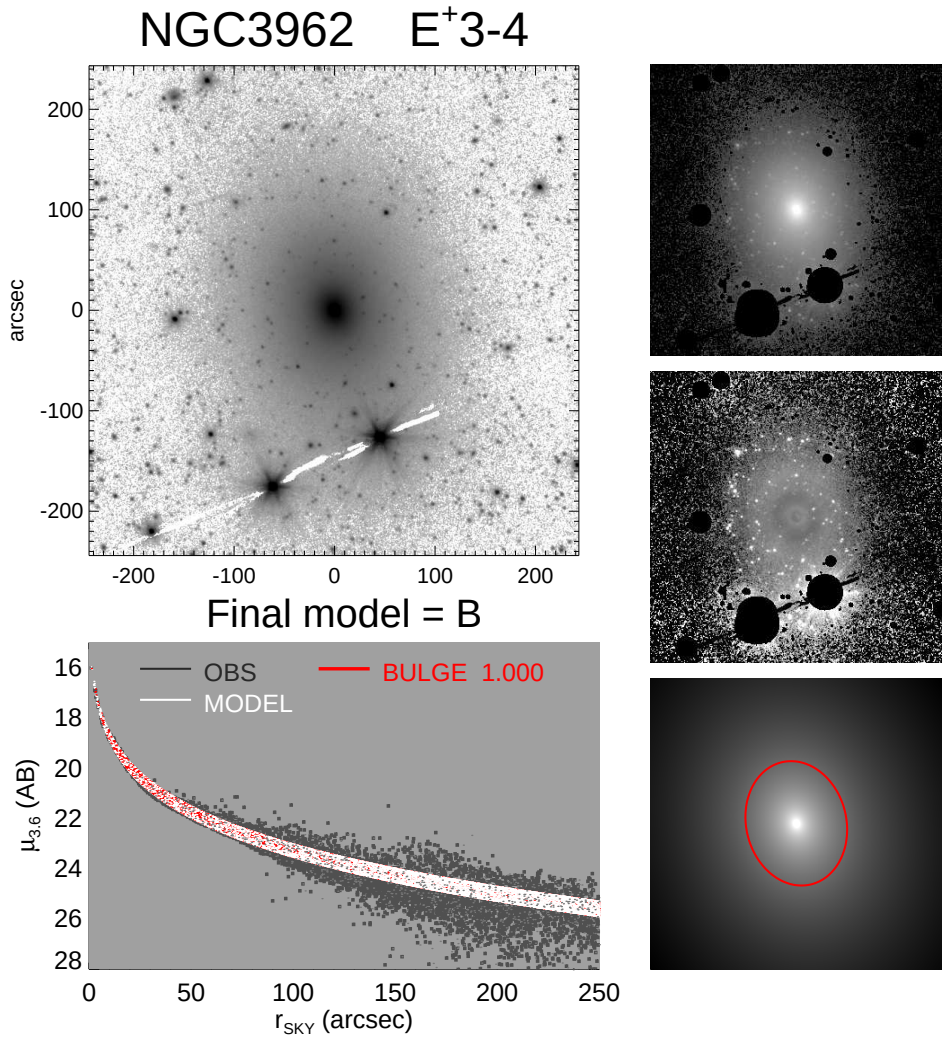

Fig. 13.— Figs. 13 -22 show the examples of final decompositions described in the text. In the big panel the galaxy image is shown in an inverted logarithmic scale (magnitude range $27 > \mu_{3.6}(AB) > 18$), clipped to display the main morphological characteristics. The three small panels show the masked original image (upper right panel), the model image (lower right), and the residual OBS-MODEL in the middle (range $\pm 1 mag$; white indicate excess light over the model). The lower left frame shows the 2D profiles of the observed and model images (black and white dots), together with the model components (colors; labels indicate the relative fraction of flux in this component; in this particular case there is only one component). The same components are also marked, with same colors, on the lower right model image: the size of the ellipse corresponds to $2R_e$ of the component in question. The mid-IR classification from Buta et al. is also indicated. In this particular example for NGC 3962, the single Sérsic fit provides an acceptable final model. The overall profile is close to de Vaucouleurs profile (Sérsic $n = 5.6$) in accordance with the morphological classification (E). Nevertheless, the slight bends in the profile and the structure in the residual image suggests that if desired, it would have been possible to get an even slightly better fit by including multiple components.

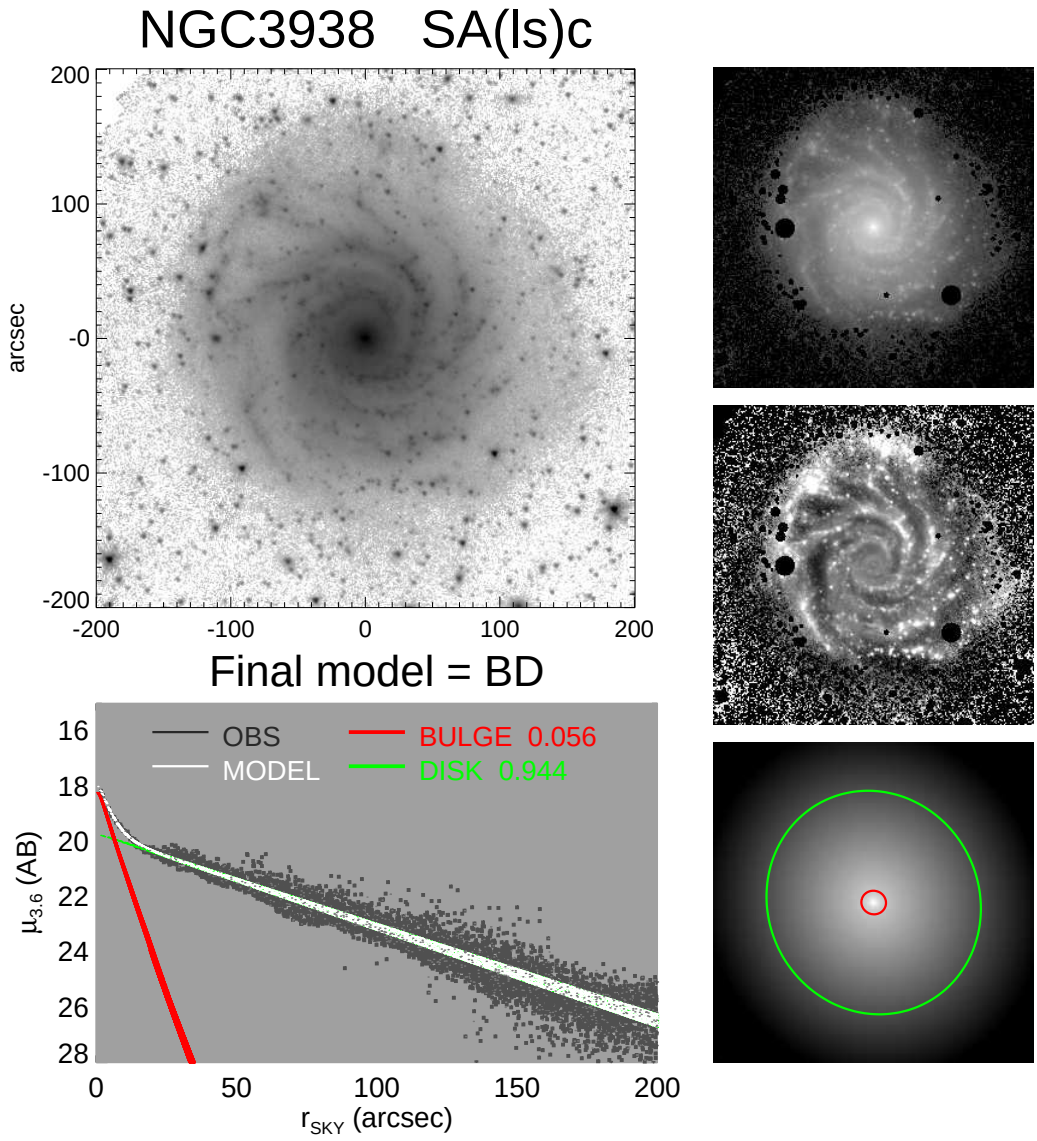

Fig. 14.— NGC 3938: Example of a galaxy in which automatic Sérsic bulge + exponential disk fitting gave an acceptable final solution. The spirals appear as small undulations on the well-fitted disk.

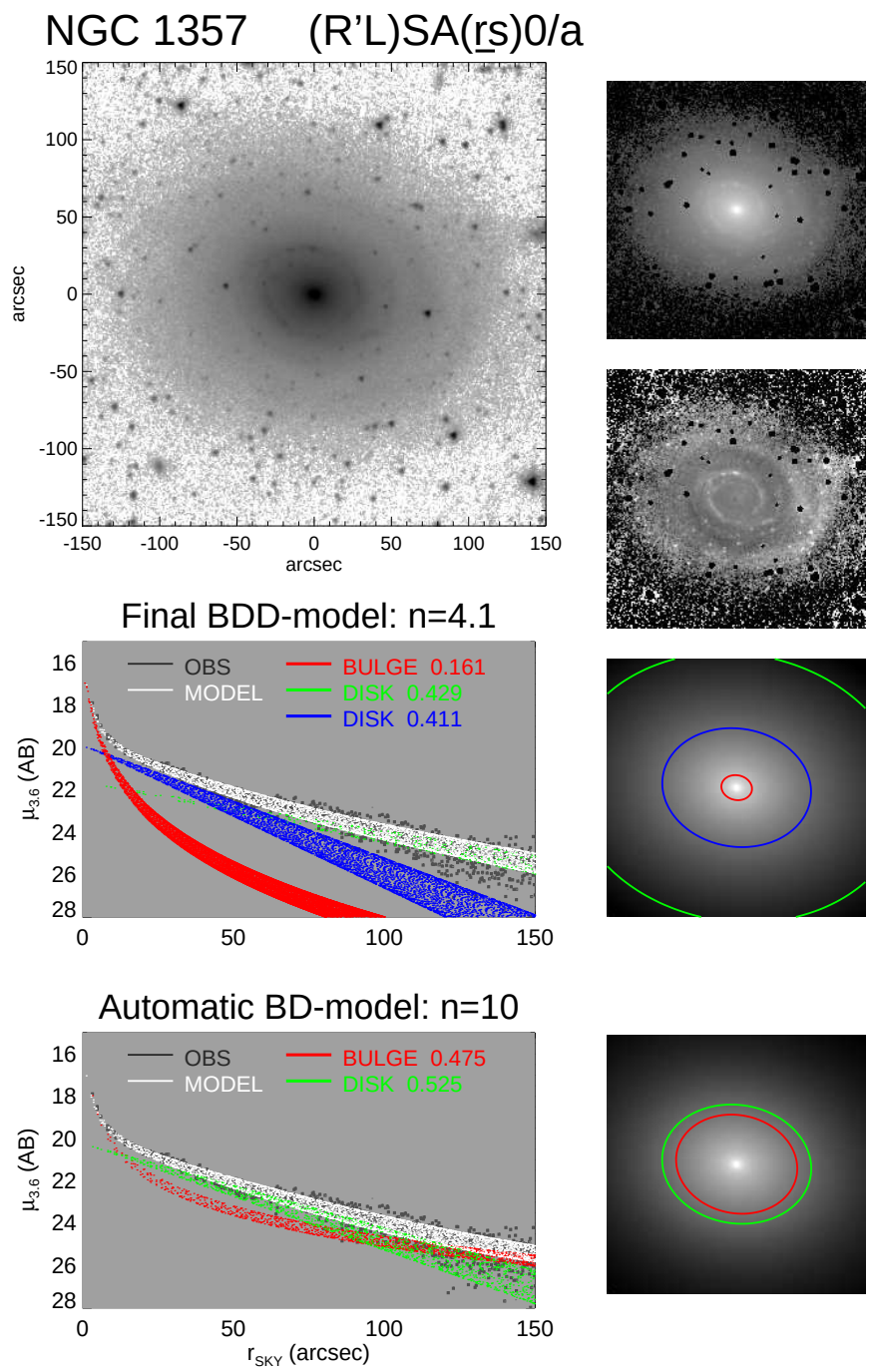

Fig. 15.— NGC 1357: The surface brightness profile of this galaxy shows a small bulge and a large, fairly exponential disk. However, again the automatic bulge-disk fit would give an unreliably large bulge extending through the whole galaxy (lowermost row). A more reasonable fit is obtained by adding another exponential disk component to the inner part of the galaxy (upper profile). This inner component corresponds to the region of tightly wound spiral arms with higher surface brightness.

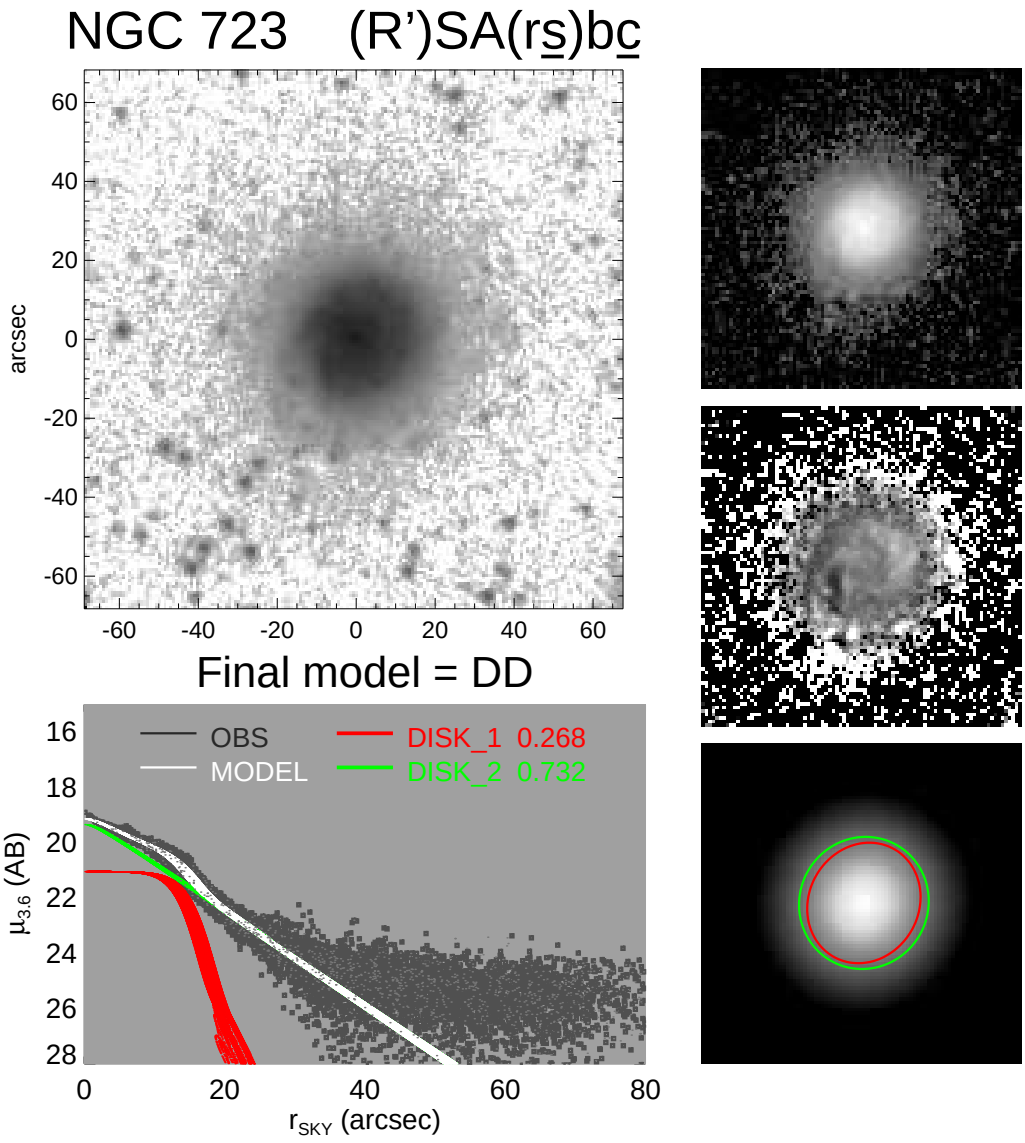

Fig. 16.— NGC 723: This is a disk galaxy with no bulge component, but it is clearly not a single exponential galaxy. The bump in the surface brightness profile corresponds to the strong high surface brightness spiral structure in the inner parts of the galaxy, here fit with a nearly flat part (Sérsic function with $n = 0.12$.

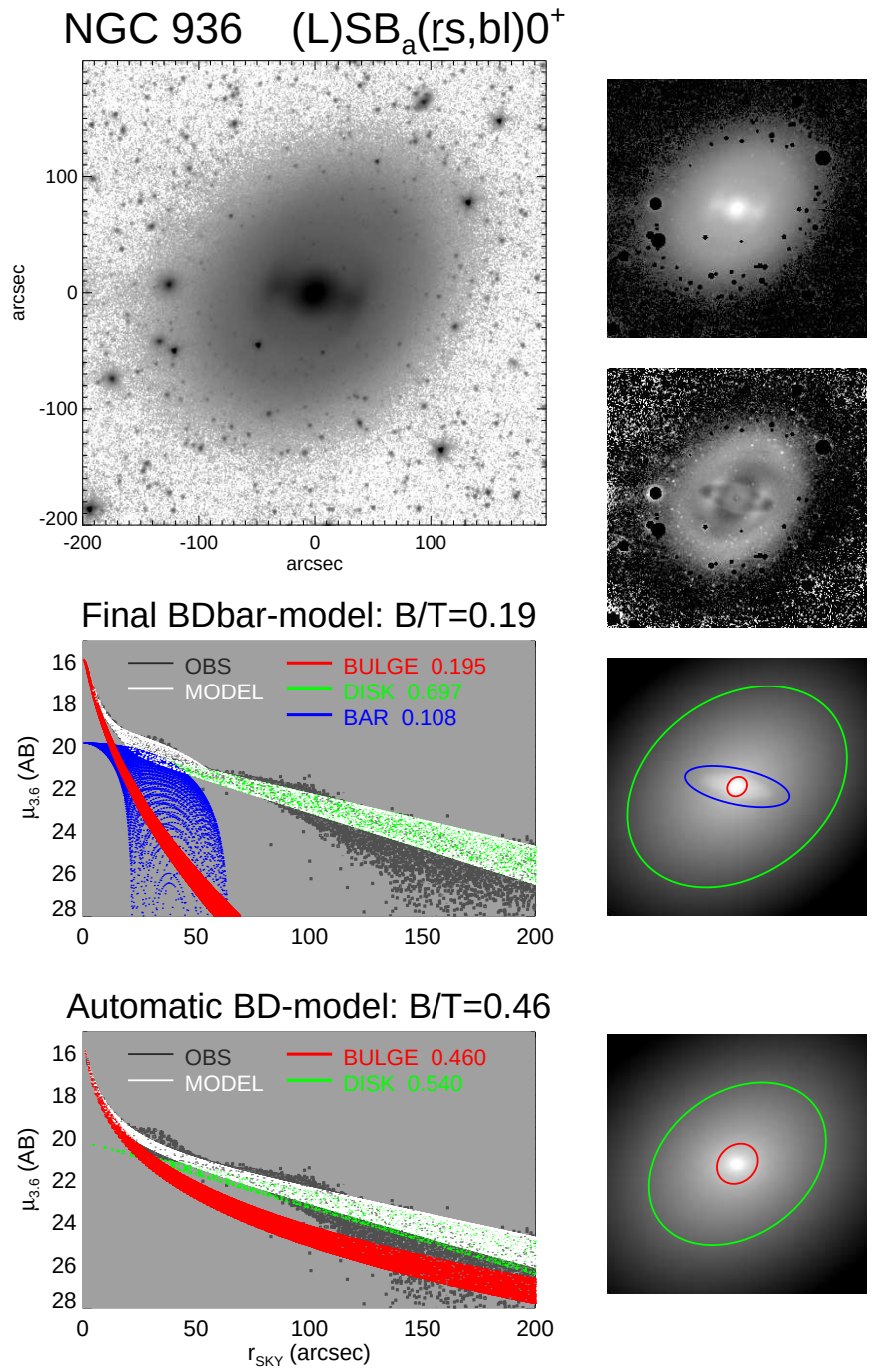

Fig. 17.— NGC 936: An example of a barred galaxy where inclusion of the bar component to the model makes a large difference in the bulge parameters. The lowermost row shows the automatic bulge/disk model, whereas the upper panels include a bar component. In the simple model, the bar flux is degenerate with the bulge flux. Multi-component decomposition is thus essential for getting a realistic bulge-to-total flux ratio: for comparisons the B/T = 0.38 in the *BD*-model, but drops to 0.18 in the *BDbar* model .

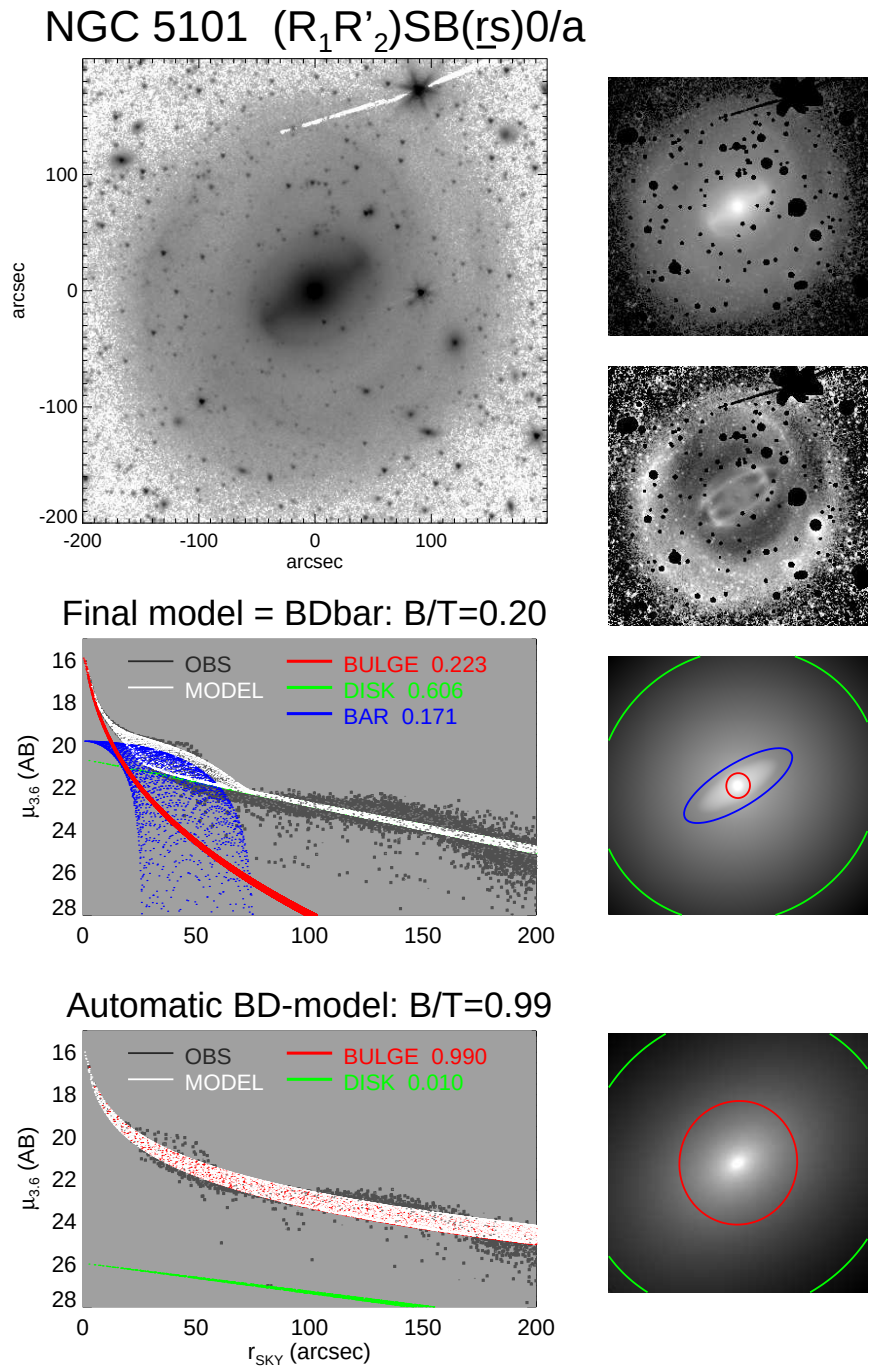

Fig. 18.— NGC 5101: Another example of *BDbar* decompositions where inclusion of the bar components is essential in getting realistic bulge parameters. Note also that in the final model the underlying disk is fit with an exponential function, although the outermost profile is downdending (Type II truncation). However, the steeper outer slope seems to be associated with a broad double outer ring, rather than a fundamentally distinct outer disk component.

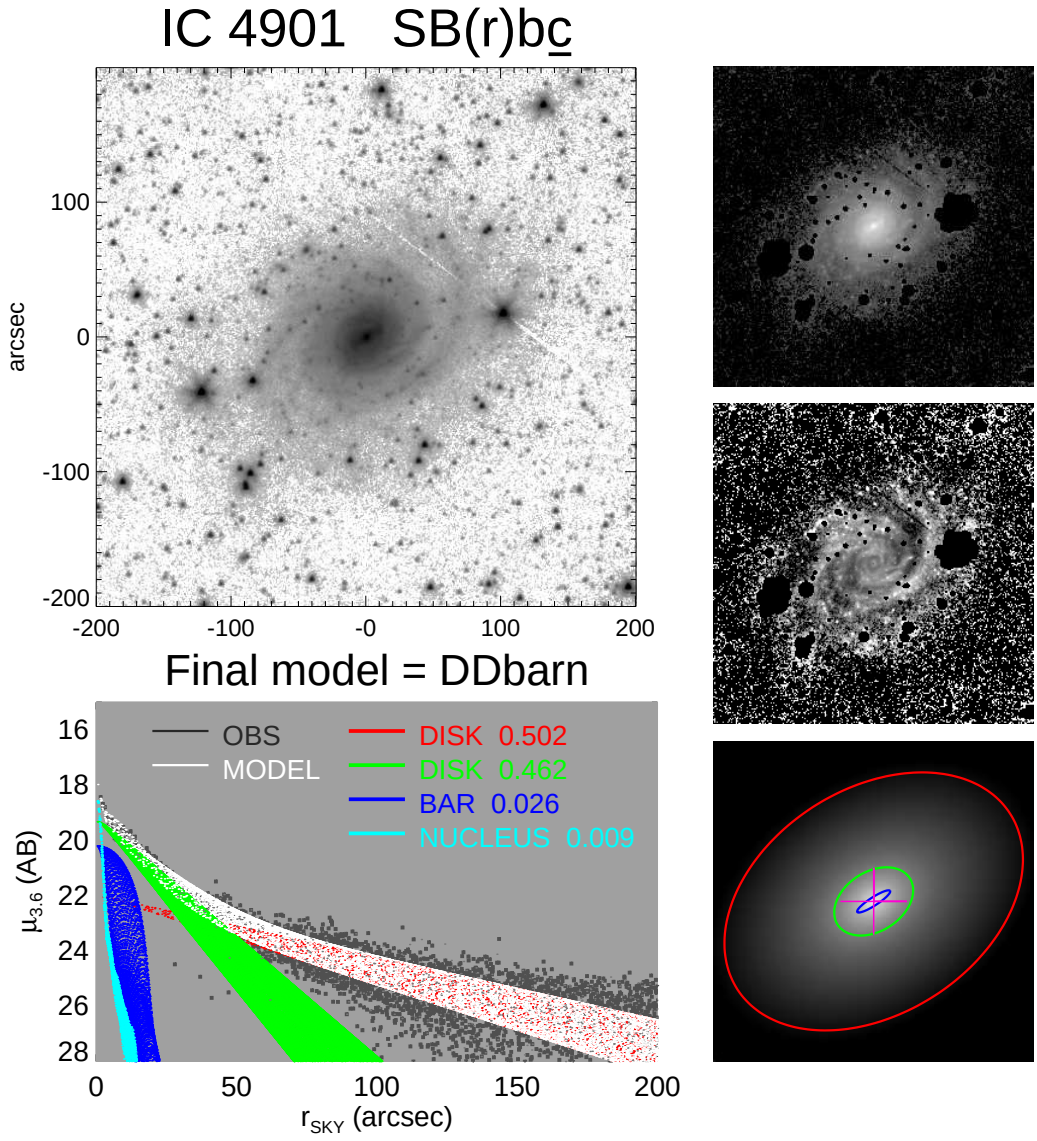

Fig. 19.— IC 4901: An example of a barred galaxy, in which the disk is fit with two exponential functions. The inner disk corresponds to the higher surface brightness part of the disk outside the bar, where the spiral arms are also prominent.

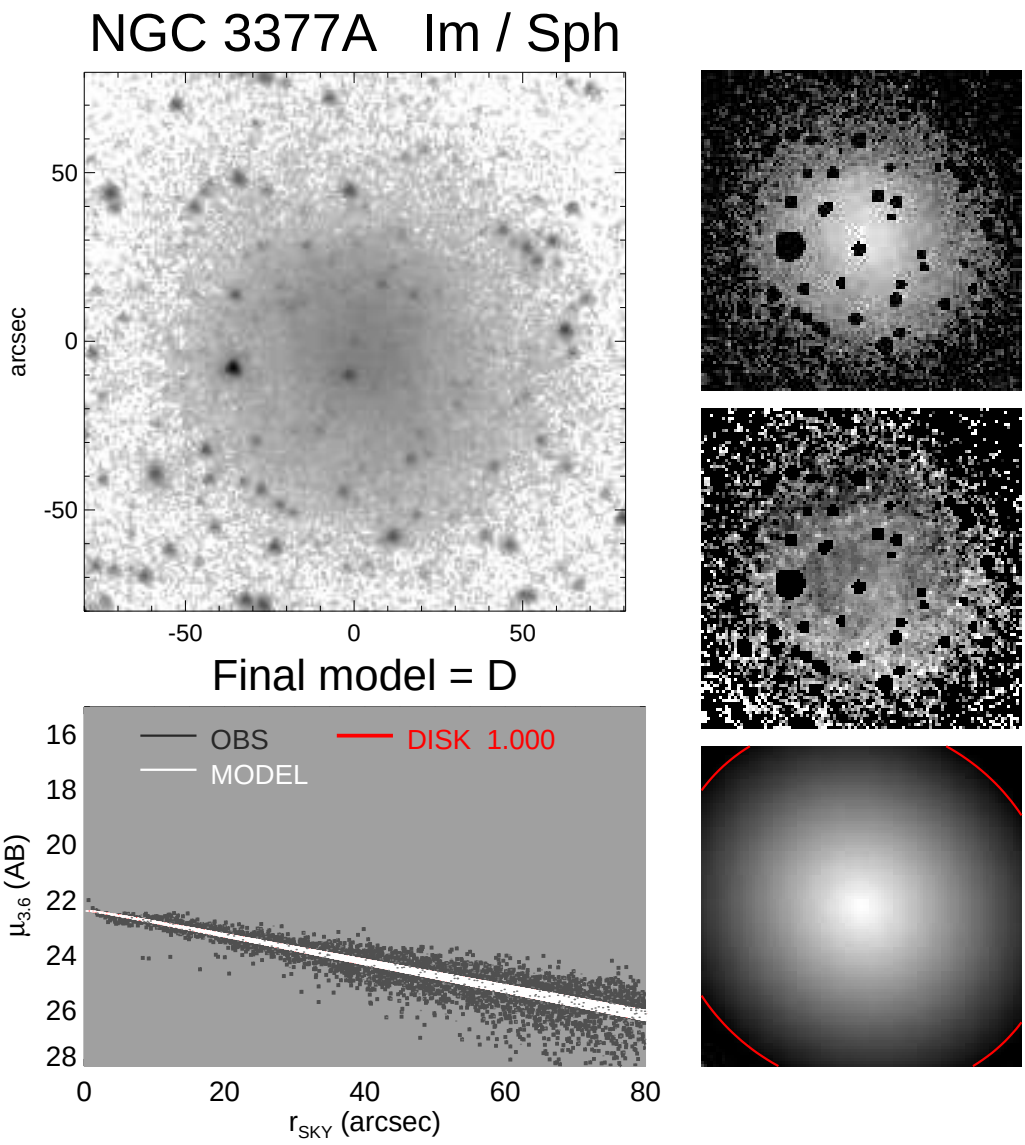

Fig. 20.— NGC 3377A: A bulgeless disk galaxy, well fit with a single exponential function.

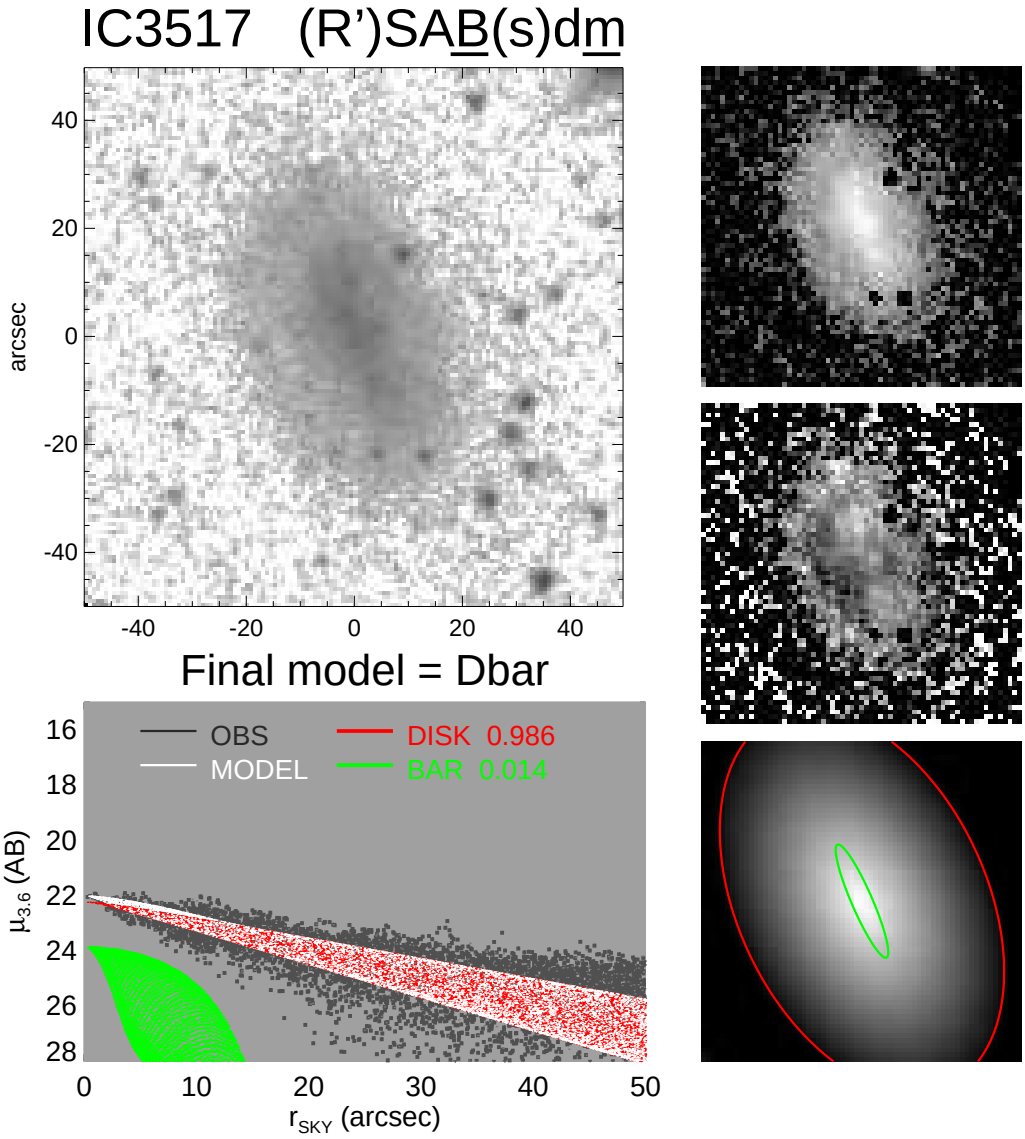

Fig. 21.— IC3517: Another example of a bulgeless disk galaxy. The surface brightness profile is well fit with a single exponential function. However, the image shows also an elongated inner structure, which can be fitted with a Ferrers function.

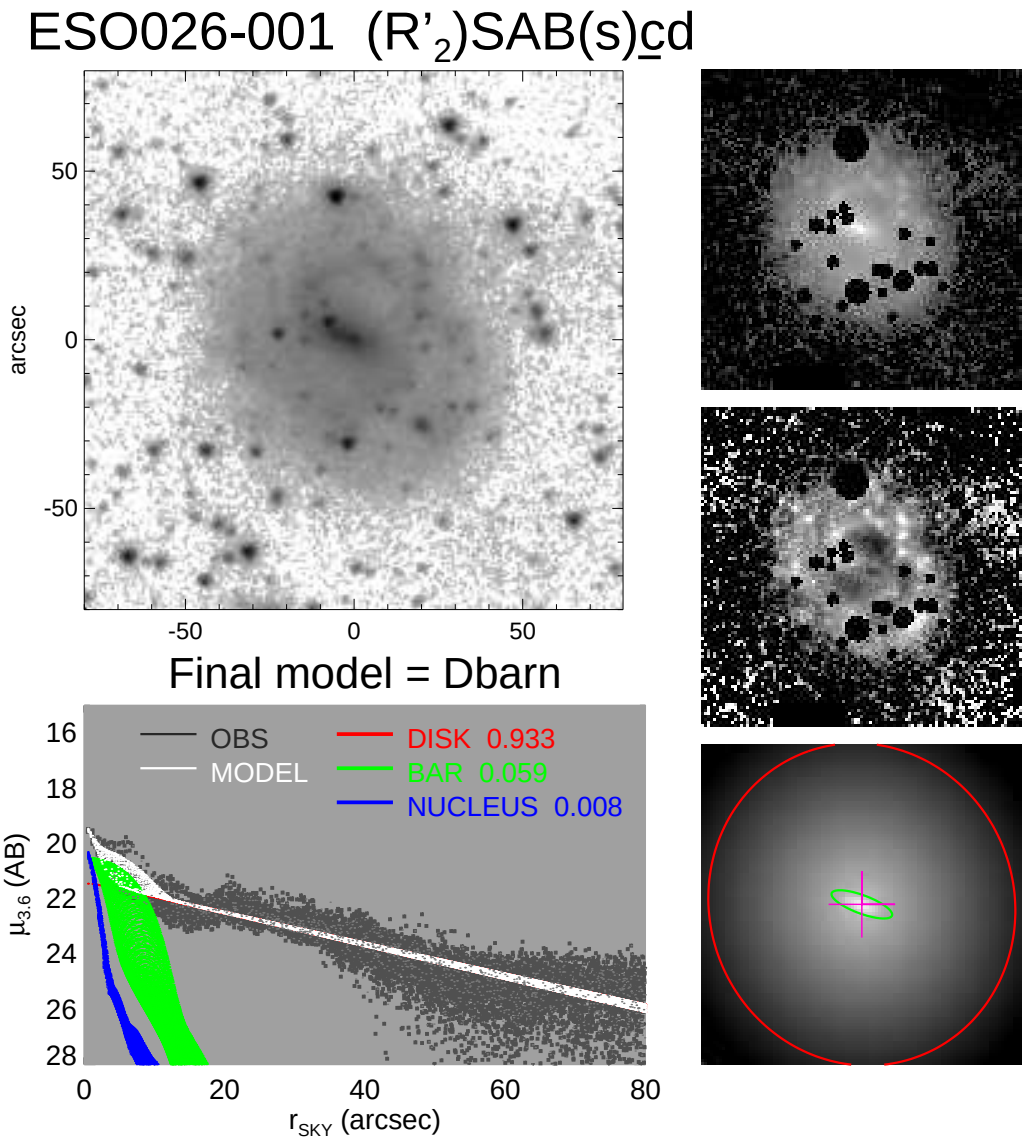

Fig. 22.— ESO026-001: An example of a galaxy in which the disk is fitted with an exponential function, although Sérsic function with n <1 would have given a more precise fit to the disk.

3.1. Uncertainties of the decomposition parameters

The formal uncertainties of the decomposition parameters have little significance, as they refer to purely statistical uncertainty due to image noise based on the assumption that the model is accurately describing the true underlying light distribution. Taking into account the complex morphology of most galaxies, this assumption is clearly not valid (see Peng et al. 2010 for detailed discussion of errors)[6]. Related to this, the final value of the reduced χ^2 is a poor indicator of the goodness of the fit (even for a good model it is much larger than unity) and is thus not used as a decisive factor in choosing the preferred final model. In practice, the choice of the final model components plays a crucial role: for example as seen in Section 3, omission of the bar component when a bar is present may lead to seriously biased bulge parameters. In this Section we perform a systematic comparison of bulge and disk parameters between 2-component and final multi-component models. We also first examine the potential uncertainties related to the preparation of data before the decompositions, namely the used PSF-function, the effect of sky subtraction uncertainty and the sigma-image.

3.1.1. PSF

As illustrated in Figure 5, the IRAC PSF has extended wings. Moreover, the PSF and the orientation of its asymmetric extensions vary from image-to-image, which has not been taken into account in the decompositions. To check the importance of the PSF wings, we compared differences in decomposition parameters obtained when the adopted composite PSF was replaced with a Gaussian PSF having the same $FWHM = 2.1''$. Fig.

[6]The formal uncertainties calculated by GALFIT are listed in the headers of pipeline output files in IRSA

23 compares the resulting effect on the Sérsic parameters in 1-component models. Clearly, decompositions with the truncated Gaussian PSF yield n values that are systematically too small, differences reaching even tens of percents for some of the galaxies (though the median deviation is only 3%). However, these rather large deviations are not representative of the true uncertainties, but rather give an idea of the magnitude of the error if the tails of the PSF were altogether ignored. A better measure of the actual uncertainty in P4 decompositions is obtained by comparing with an azimuthally symmetrized version of the composite PSF. Clearly, now the differences in n are much smaller (see the red symbols in Fig. 23).

We also checked the influence that the PSF has in the multi-component models. For that purpose we rerun all final decompositions that included both bulge and disk components (+ possible bar and center components; total of 515 models after excluding nearly edge-on galaxies), using both the Gaussian PSF and the symmetrized PSF. Table 3 lists the median of relative differences in bulge $B/T, n$, R_e, disk scale lengths h_r, and bar-to-total ratio Bar/T, when compared to the results obtained using the standard composite PSF. The largest differences are seen for the Sérsic parameters while using the Gaussian PSF, whereas h_r is barely affected. On the hand, the differences in parameters between those obtained using the composite PSF and using the symmetrized version are negligible. Based on these results we conclude that the spikes of the PSF have no significant effect as long as the nearly circular wings of the PSF are included. The use of single composite PSF for all S4G images should thus be acceptable.

3.1.2. Sky subtraction

In principle, poor sky subtraction can severely affect the decomposition results, in particular the parameters of the disk. To constrain the possible magnitude of such

uncertainties, we rerun the multi-component decompositions that included both bulge and disk components (+ possible bar and center components; same 515 models as above). Two additional sets of sky values, $SKY' = SKY \pm 0.5 \times DSKY$, were used. Fig. 24 shows the effect on the scalelength of the disk. Although individual changes can in few cases be large ($h_r(\mathrm{mod})/h_r(\mathrm{ori}) > 1.2$ in 9 cases when too small a sky is subtracted), the median differences are less than 2% (and even smaller in the other parameters of interest, see Table 4). The sky subtraction is not a concern in the current decompositions.

3.1.3. Sigma-image

The weighs applied to various pixels have an important role in decompositions, in particular when the galaxy structure is complicated, so that the differences between the applied model and the true structure are large. As mentioned in Section 2.2.5 the σ-image itself is a statistical estimate of the underlying σ in each pixel, so it might be reasonable to smooth it before applying to decompositions. In Fig. 25 (left column) we examine the effect of sigma-image smoothing on the derived bulge parameters. A median filter is applied with a width of 5 pixels. Clearly the effect is quite small except for a few deviant cases marked on the plot. In these cases the bulge parameters are sensitive also to changes in the PSF or the sky background level. This can be due to perturbed morphology (e.g. NGC 3773 classified as SA0 pec has asymmetric structure near the center), although in some cases there is no obvious reason (e.g. NGC 3321). For NGC 3021 the apparent bulge effective radius is in fact below the FWHM of S4G-images, so that all bulge parameters except the B/T ratio are ill-defined (an equivalent model with a PSF-component instead a Sersic yields same $B/T \approx 0.04$). In the tabulation of final decomposition parameters we will flag such ambiguous cases.

For comparison, Fig 25 (right column) also illustrates the changes in bulge parameters

if a constant sigma is assumed at all image pixels. A constant sigma exaggerates the relative weight of the central regions compared to the outskirts. Besides a large scatter, also a systematic increase of the estimated n is obvious: the median $n_{mod}/n_{ori} = 1.2$ (the mean ratio is 1.4). What typically happens is that the fit tries to reproduce the central peak with an increased n, even if the outer disk becomes too much bulge dominated. Indeed, the bias (and the scatter) is particularly large for earlier type disks (open circles in the plot indicate $T \leq 5$; median $n_{mod}/n_{ori} = 1.25$). This comparison reminds that when decomposition parameters from different studies are compared, it is always important to pay attention that proper weights have been applied.

3.1.4. Two-Component versus multi-component decompositions?

Automatic 2-component Sérsic-exponential (or Sérsic-Sérsic) models are often applied to large data surveys. This is a natural approach as the data quality (depth/angular resolution) might be insufficient for more detailed modeling, and simply because of the large effort involved in multi-component decompositions. Moreover, it has been recently claimed (Tasca & White, 2011) that 2-component decompositions (Sérsic + exponential) are also sufficient for fitting barred galaxies. Their argument was based on obtaining similar average B/T ratios for barred and nonbarred galaxies in their 2-component bulge/disk models. They reasoned that if the omission of the bar were a problem it should manifest as a higher B/T for barred galaxies. However, to accurately address this matter one has to compare the different types of decompositions (2-component and multi-component) for well-defined samples of barred/non-barred galaxies.

Such a comparison between different decomposition models is shown in Fig. 26. Again, those galaxies for which the final model contains both a bulge and a disk are studied. For the non-barred galaxies (those with no *bar*-component; leftmost column in the Figure)

the bulge parameters (Sérsic n, B/T, R_e/h_r) in automatic 2-component runs are almost identical to those in the final models. This agreement is expected because about 85% of the final non-bar models are just Sérsic-expodisk models (15% have two disk components), and typically the automatically found *bd* models did not need any refinement. For barred galaxies (those with a *bar*-component in final model; middle column), the obtained median values depend drastically on whether the bar is included. This result emphasizes that the examples of decompositions given in Section 3, highlighting the importance of modeling the bar (e.g. Figs. 17 and 18) were not exceptional cases. Overall, ignoring the bar increases the estimated B/T ratios by a factor of 2-3 because of gross (even by as much as a factor of 5) overestimate of R_e and n. For example, for spirals in the range $1 \leq T \leq 5$ the 2-component decompositions suggest $n \gtrsim 4$ whereas the multi-component runs indicate $n \approx 1 - 2$. Altogether, the difference in bulge parameters obtained in the multi-component decompositions for barred and non-barred galaxies is fairly small (right column in the Figure).

The conclusion that multi-component decomposition models are essential to measure realistic bulge parameters for barred galaxies is not new (Laurikainen et al. (2006, 2007), Gadotti (2009) and Weinzirl et al. (2009)). Similar conclusion, based on synthetic images, was reached also by Laurikainen et al. (2005).

In Fig. 27 we compare the combined bar/nonbarred sample of the previous figure with the decompositions in Laurikainen et al. (2007). Because of the large fraction of barred galaxies, the difference in the obtained bulge properties between the 2-component and multi-component decompositions remains significant, even when barred and nonbarred galaxies are considered together. What is remarkable is the excellent agreement between the current multi-component results and those in Laurikainen et al. (2007), obtained with a completely different decomposition code, and based on different near-IR image data. It is

worth noticing that in these decompositions Sérsic n for Hubble types Sa-Sc is nearly $n \sim 1$, whereas in the decompositions by Tasca & White (2011), for the same Hubble types, Sérsic index is peaked at $n \sim 4$. Small values of the Sérsic index, similar to ours for these Hubble types, are reported also by Graham & Worley (2008).

Table 3. The effect of modified PSF on final decomposition model parameters

	GAUSSIAN PSF		SYMMETRIZED PSF	
	median(D)	median($\|D\|$)	median(D)	median($\|D\|$)
B/T	-1.5 %	4.5 %	-0.1 %	0.2 %
n	-3.0 %	7.8 %	0.0 %	0.5 %
R_e	8.9 %	9.8 %	0.1 %	0.3 %
h_r	0.0 %	0.3 %	0.0 %	0.0 %
Bar/T	-1.5 %	4.4 %	-0.1 %	0.2 %

Note. — D stands for the relative difference (e.g. $D = [n(\mathrm{mod}) - n(\mathrm{ori)}]/n(\mathrm{ori}))$, where 'ori' refers to the standard composite PSF. Medians are used to characterize the typical deviations and the scatter, to eliminate spurious cases where the decompositions with Gaussian PSF converged to a different type of solution.

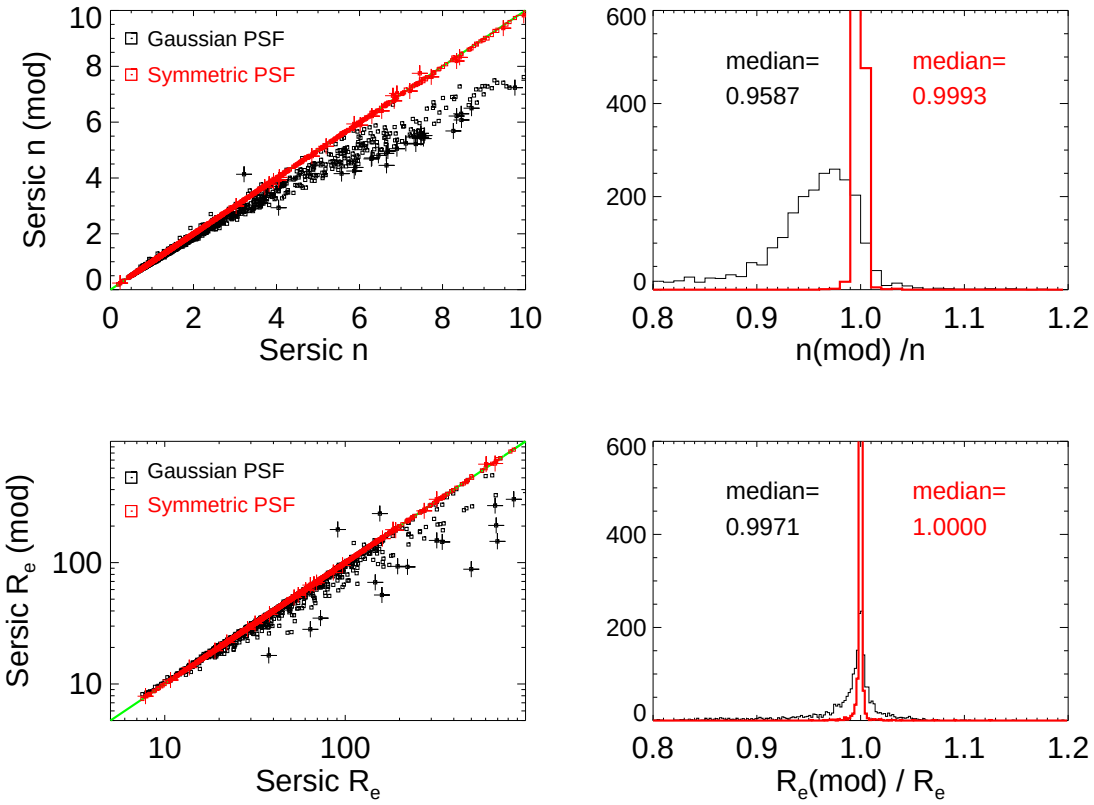

Fig. 23.— The plots on the left show the Sérsic index and effective radius in 1-component fits using modified PSFs: black symbols indicate results using a Gaussian PSF (wings truncated), and red points a symmetrized composite PSF. Larger black (red) symbols indicate points deviating more than 25% (10%) from the unit line. In the right panels the histograms of the relative changes in the parameters are shown: black and red colors have the same meaning as in the left frames

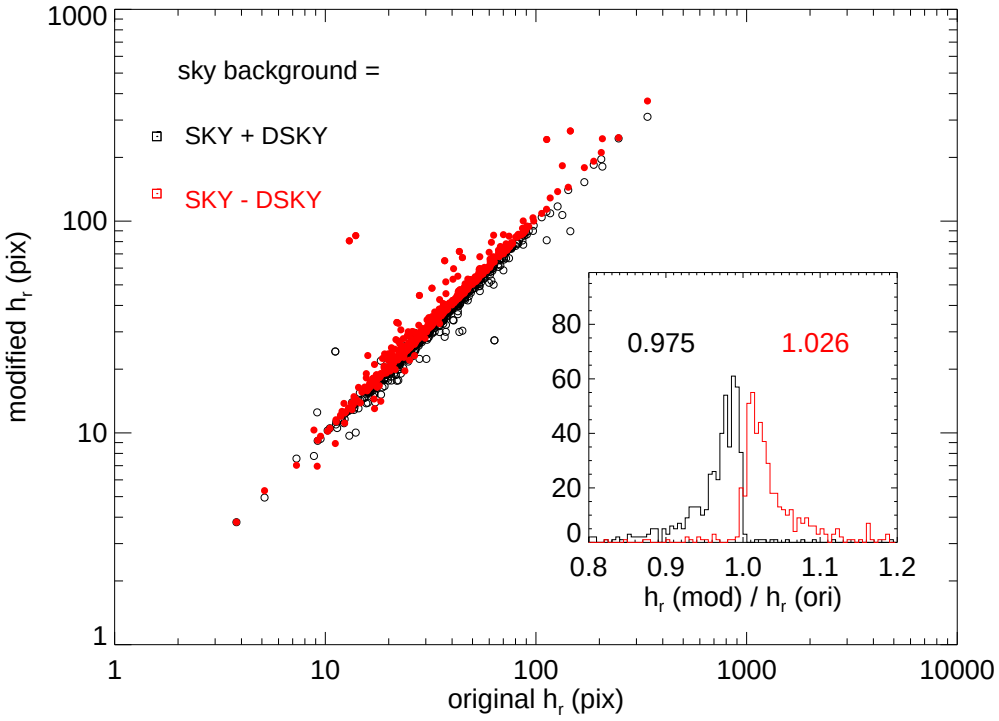

Fig. 24.— The effect of sky background subtraction on the disk scalelength. All final decomposition models including both a bulge and disk (and possible additional bar and central components) were rerun using images where the assumed sky background was modified by $\pm DSKY$, where $DSKY$ is the conservative estimate of global sky variations in the image (see Section 2.2.3).

Table 4. The effect of sky subtraction on final decomposition model parameters parameters

	SKY + DSKY		SKY - DSKY	
	median(D)	median($\|D\|$)	median(D)	median($\|D\|$)
B/T	0.2 %	1.5 %	-0.1 %	1.6 %
n	-1.4 %	1.8 %	1.8 %	2.0 %
R_e	-1.2 %	1.4 %	1.7 %	1.8 %
h_r	-2.5 %	2.6 %	2.6 %	2.8 %
Bar/T	0.2 %	1.5 %	-0.1 %	1.6 %

Note. — D stands for the relative difference (e.g. $D = (n(mod) - n(ori))/n(ori)$), where 'ori' refers to the standard sky subtraction.

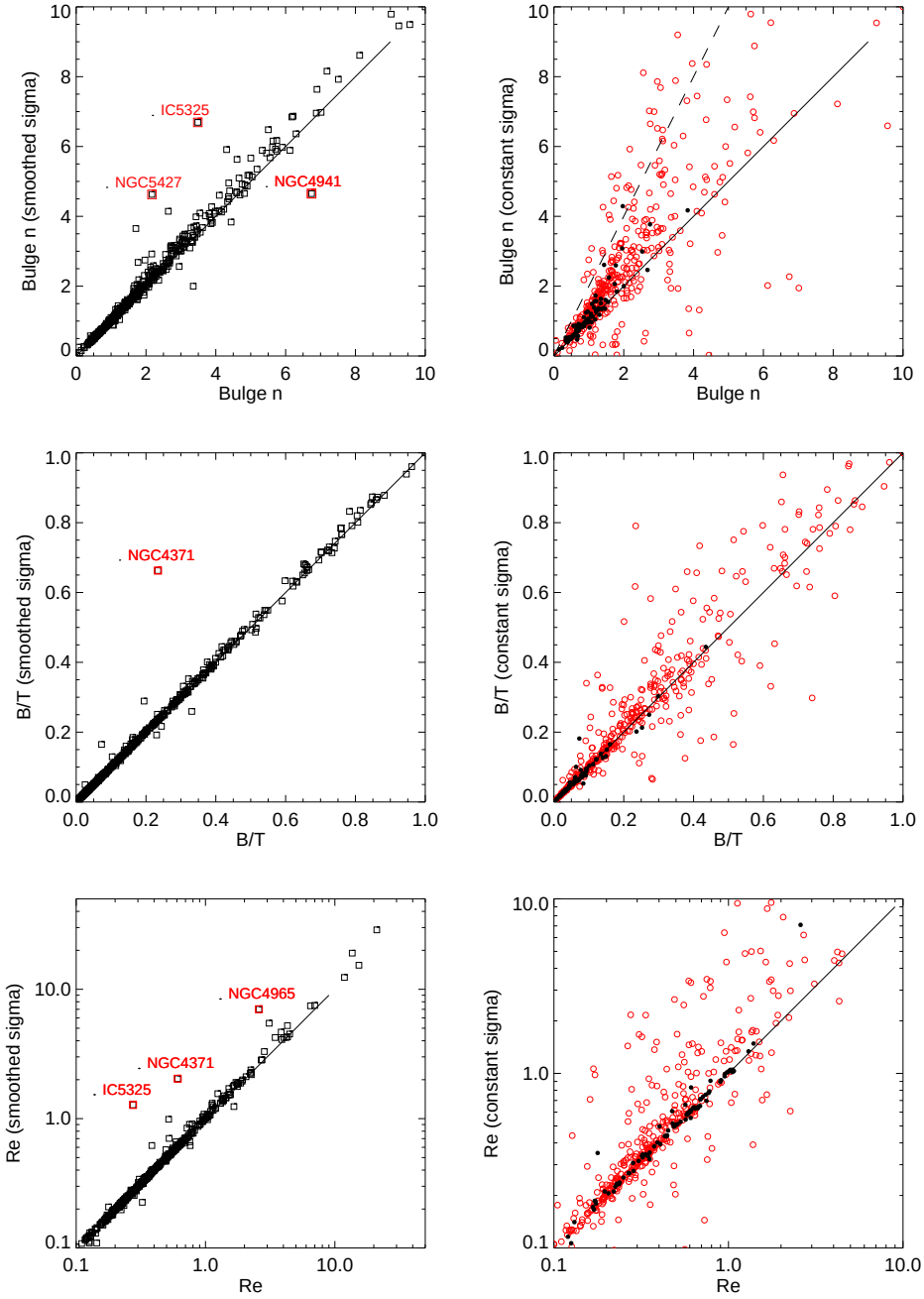

Fig. 25.— Sensitivity of estimated bulge parameters (Sersic n, bulge-to-total flux ratio B/T, effective radius R_e in kpc's) on the used σ-image. In the left column, we have smoothed the P4 σ-images with $5pix \times 5pix$ median filter, while in the right it has been replaced with a constant σ. The scatter plots show the modified parameter values versus the original ones. In the right, the red open and black filled circles refer to galaxies with mid-IR type $T \leq 4$ and $T \geq 5$, respectively. Lines corresponding to one-to-one correspondence are drawn in each frame: in the right uppermost frame the dashed line indicates $n_{mod}/n_{ori} = 2$.

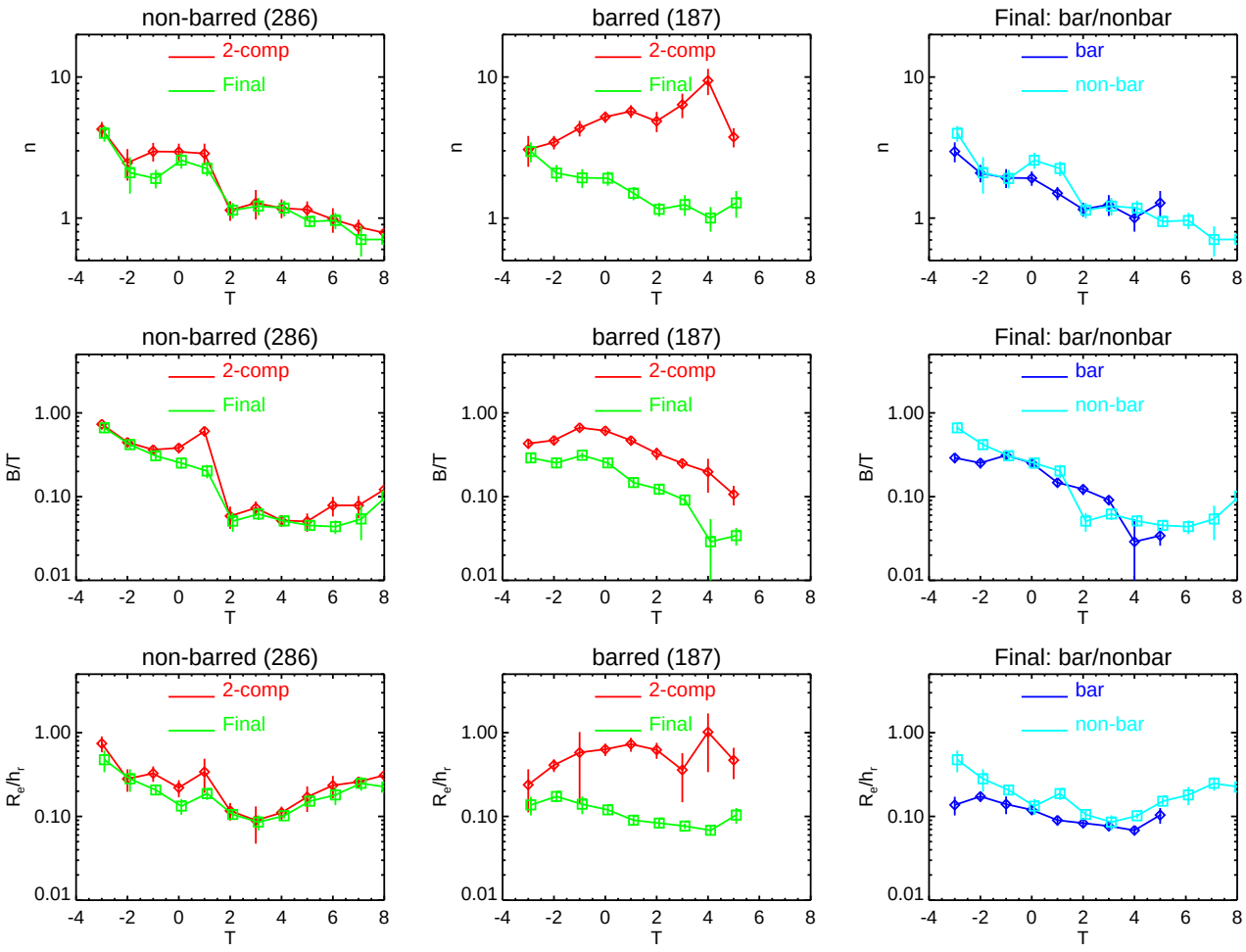

Fig. 26.— Comparison of bulge parameters between automatic 2-component and final multi-component decompositions. The morphological type T is from Buta et al. (2014) mid-IR classification. Comparison is made for the galaxies for which the final model included both bulge and disk components. In the left frames decompositions for non-barred galaxies are compared, while the middle frames show those with a bar component in decompositions. In the right frames the final decompositions for barred and nonbarred galaxies are compared. The symbols stand for median values in bins with five or more galaxies, error bars are errors of the mean values in the bin.

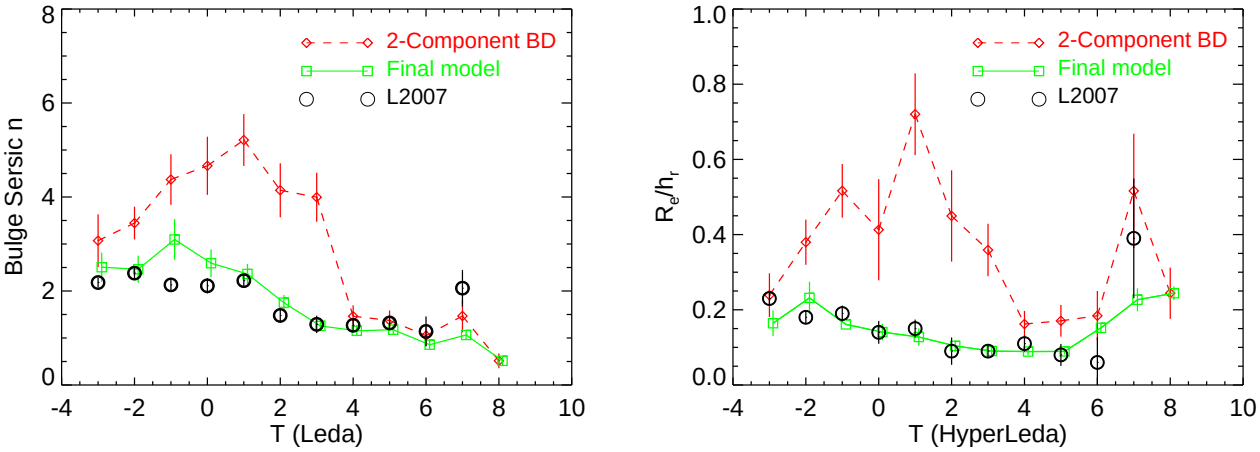

Fig. 27.— Comparison of final S^{4}G decompositions parameters to those of Laurikainen et al. (2007; the values are tabulated in Table 2 in Laurikainen et al. 2010) multi-component decompositions for NIRS0S (K_s band, 143 galaxies $-3 \leq< T < 1$) and OSUBSGS (H band, 129 galaxies $2 \leq 7$) data. In a) Sérsic n-parameter and in b) R_e/h_r. S^{4}G results show 516 galaxies for which the final decomposition model contained both a disk and a bulge component (excluding nearly edge-ones). For comparison, also the results of semi-automatic 2-component decompositions are shown. The symbols stand for the median values in each bin with 5 or more galaxies, while the error bars denote the error of the mean. Note that here the optical classifications from Hyperleda are used to facilitate comparison with previously published results.

3.1.5. Disk truncations

One of the main goals of Pipeline 4 is to obtain measurements for the galaxy size-magnitude scaling relations. In order to be consistent with earlier analysis (e.g Courteau et al. 2008) the P4 final models as a default use single exponentials. However, deep optical and near-IR surveys (Erwin et al. 2005, Pohlen & Trujillo 2006, Gutierrez 2011, Munoz-Mateos et al. 2013) have shown that only a fraction of galactic disks ($\sim 1/3$) are simple exponentials (=Type I in Pohlen & Trujillo 2006 classification). Instead the typical brightness profiles consist of two (sometimes three) exponential subsections with different radial slopes. When the outer disk has a steeper slope, the galaxy is classified as possessing a Type II truncation, and conversely if the outer slope is more shallow, it is classified as a Type III truncation ('antitruncation'). Kim et al. (2014) have recently made 2D decompositions for 144 barred S^4G galaxies taking into account disk truncations in their decompositions with the BUDDA code (de Souza et al. 2004, Gadotti 2008, 2009). Their fitting function for the disk consists of two exponential sections, with different scale-lengths (h_{in} and h_{out}) inside and outside the break radius R_{break}. They also made decompositions where they fitted the disk with a single exponential component. According to their result the inner scale lengths for two-component disks are typically about 40% longer than the scalelengths obtained in single disk fits; they thus conclude that "it is important to model breaks in Type II galaxies to derive proper disk scale lengths."

Nevertheless, it is not always obvious what is the "proper" disk scale length estimate in case the galaxy exhibits several exponential subsections. For example, it is well known (Pohlen and Trujillo 2006) that Type II breaks are often connected to outer rings associated with bar OLR resonances. Such breaks are indeed dominant for early type barred disks ($T < 3$; Laine et al. 2014). Since the bar torques are able to push material from the CR regions out toward OLR, this will promote a shallower distribution inside the break radius.

However, beyond the OLR the effect of bar is insignificant, so that the underlying disk can remain more or less intact. In such a case it might in fact be the outer, rather than the inner scalelength that would better characterize the original mass distribution. On the other hand, for later Hubble types the Type II truncation is often connected with the end of prominent spirals (Laine et al. 2014) and could be due to suppressed star formation: for such a case the inner scale length might indeed be more appropriate to characterize the disk as a whole. Laine et al. (2014) also find that for such spiral-related breaks the ratio h_{inner}/h_{outer} is typically closer to unity than for OLR related breaks.

Figure 28 compares Pipeline 4 decompositions with recent disk truncation studies, which use subsamples of the exactly same S^{4}G dataset. Besides the above-mentioned Kim et al. (2014) study, we also compare with Munoz-Mateos et al. (2013) and Laine et al. (2014), where fits to 1-dimensional profiles were conducted. First of all, the Figure (upper row) indicates a very good agreement for the scale lengths of Type I profiles between all four studies, conducted with independent methods. Secondly, it illustrates the significant difference between the inner and outer slopes for Type II (and III) profiles, amounting to roughly a factor of two in agreement with that reported in Munos-Mateos et al. (2013) and Kim et al. (2014) original studies. The P4 single disk scalelengths seem to fall quite close to being a geometric mean of h_{inner} and h_{outer}, in particular when comparing with Munoz-Mateos et al. (2013) and Laine et al. (2014).

To emphasize the possible 'unperturbed' nature of Type II outer disks, Fig. 29 compares the P4 scale lengths for Type I galaxies (following classifications from the above mentioned truncation studies) with those of the outer disks in Type II galaxies, collecting together Munoz-Mateos et al., Laine et al. and Kim et al, measurements of h_{outer}. Indeed the difference between the Type I single disk h and the Type II h_{outer} are quite small. The fits to the data also give the impression that h_{inner}/h_{outer} ratio gets closer to unity

for less massive galaxies: this is in accordance with the above mentioned dominance of spiral-related less abrupt truncations for later and on average less massive spirals.

The Pipeline 4 single exponential fits have a nice feature of taking an effective average over inner and outer disks (when present). They thus provide a homogeneous set of robust scale measurements, not sensitive to factors modifying the local slopes. Nevertheless, a possible caveat is that the fitted effective single h might become dominated by different degrees by the inner/outer parts, depending on the galaxy surface brightness. For example, the estimated h might be biased toward h_{inner} when the disk central surface brightness decreases toward less massive galaxies: this would be the case if the image depth was not sufficient to cover the galaxy regions beyond the break radius. Fig. 30 addresses this potential problem by comparing the trends of the break radii with respect to galaxy mass, to that of the galaxies' visual outer extent (R_{gal}, see Sect 2.2.3; a similar trend would result if $R_{25.5}$ were plotted instead of R_{gal}). The figure indicates that breaks, if present, should be visible through the whole range of S^4G galaxy masses.

In summary, we feel confident that the single disk fits provide a useful overall estimate of the disk original scale length (and its extrapolated surface brightness), though especially in case of barred massive galaxies secular evolution might have led to significant deviations from simple exponentials, important to include in detailed models for individual galaxies. Moreover it is likely that the slope differences associated with truncations are smaller for later types, forming a vast majority of S^4G galaxies.

Nevertheless, as concluded by Kim et al., estimates of other decomposition parameters, like the B/T ratio for massive galaxies would become more accurate if steeper inner slopes are accounted for (less disk light assigned to bulge). The situation is somewhat analogues to the benefit of including extra inner components like bars in the decompositions (Laurikainen et al. 2005, Gadotti 2008), or lenses in S0s (Laurikainen et al. 2011). However, for the

goals of Pipeline decompositions, the expected magnitude of changes (about 10% relative change is B/T) is very small, compared to, say, the uncertainties related to choice of the decomposition model components (say, including a bar versus ignoring it). The choice of the code might also sometimes have a bigger effect. For example, Kim et al. (2014) use NGC 936 as an example of Type II galaxy (see their Fig. 4). For this galaxy they fit a break at 98″ and derive $h_{inner} = 53''$ and $h_{outer} = 28''$, all very close to both Munoz-Mateos et al. and Laine et al. measurements. On the other hand, the Pipeline 4 single disk fit (see Fig. 17) gives $h = 40''$. We verified that truncating the disk in GALFIT decompositions at the Kim et al. break radius reproduces their inner slope quite well (we get 57″). At the same time, the B/T increases slightly (from 0.19 to 0.22), in accordance with Kim et al.[7]. Nevertheless, the B/T we obtain after accounting for the more shallow inner slope is still nearly 50% smaller than their value (B/T=0.32), probably because of some model/code dependent factors, like the weighting of image pixels which might be different in the two studies.

[7]We also checked the effect of letting the boxiness and shape parameters of the bar free but these had only a small effect

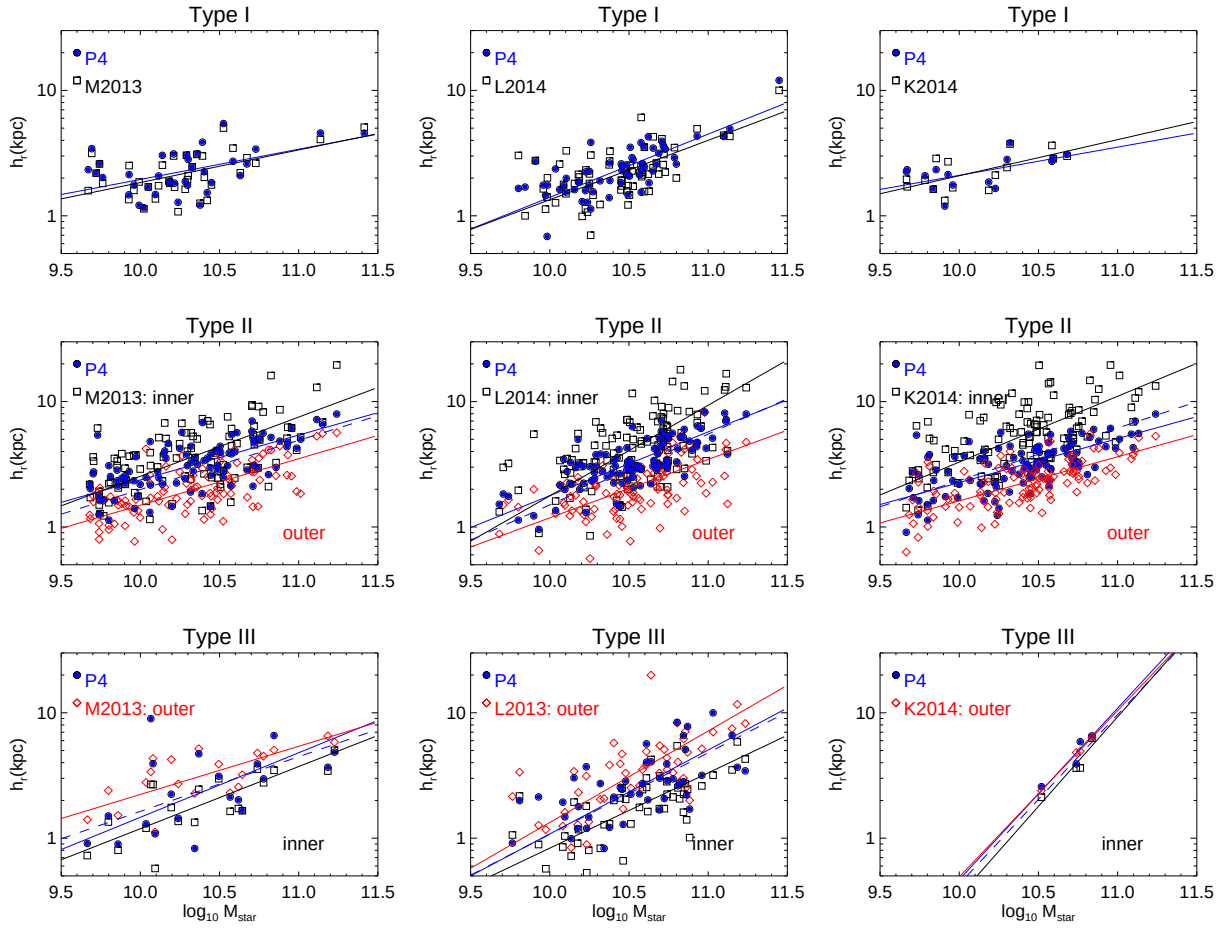

Fig. 28.— Comparison of P4 single disk scalelengths with decomposition studies including disk truncations. In the left frames the h_r vs. stellar mass, obtained in P4 (blue symbols) are compared with the results in Munoz-Mateos et al. (2013; M2013) and Laine et al. (2014; L2014), where inner and outer scalelengths (h_{inner} and h_{outer}, denoted with black and red symbols, respectively) were estimated for S^{4}G galaxies from fits to 1-dimensional profiles. On the right, similar comparison to Kim et al. (2014; K2014), who used 2D BUDDA decompositions for 144 barred S^{4}G galaxies. In the uppermost frames Type I disks (no truncation) are compared: the lines show orthonormal fits to the measurements (orthogonal deviations minimized with the help of IDL PCOMP routine). In the middle same for Type II truncations: the dashed blue line indicates a fit to geometric means of the inner and outer scalelengths. In the lowermost frame: galaxies with Type III truncations.

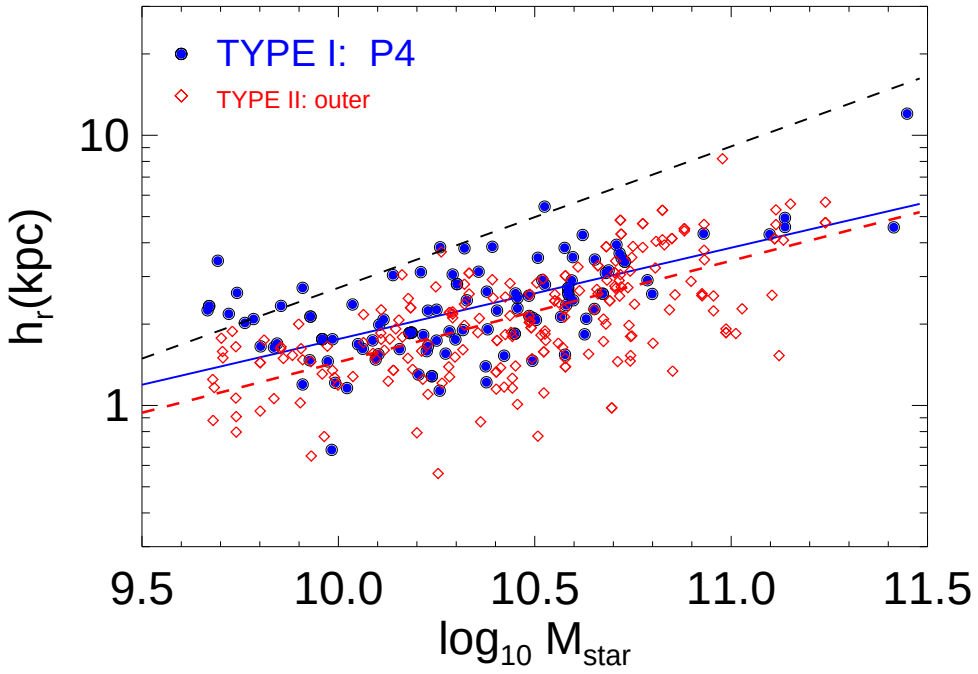

Fig. 29.— Comparison of P4 scalelengths for Type I galaxies (green points), with the outer scalelengths of Type II profiles (red points; combining Munoz-Mateos et al. (2013), Laine et al. (2014) and Kim et al. (2014) measurements). Also shown are the corresponding orthonormal fits (blue and red lines), and a corresponding fit to inner scalelengths derived in the above mentioned studies (individual measurements not shown). Note that the single scalelengths in Type I galaxies resemble more those of outer scalelengths in Type II's than the inner ones.

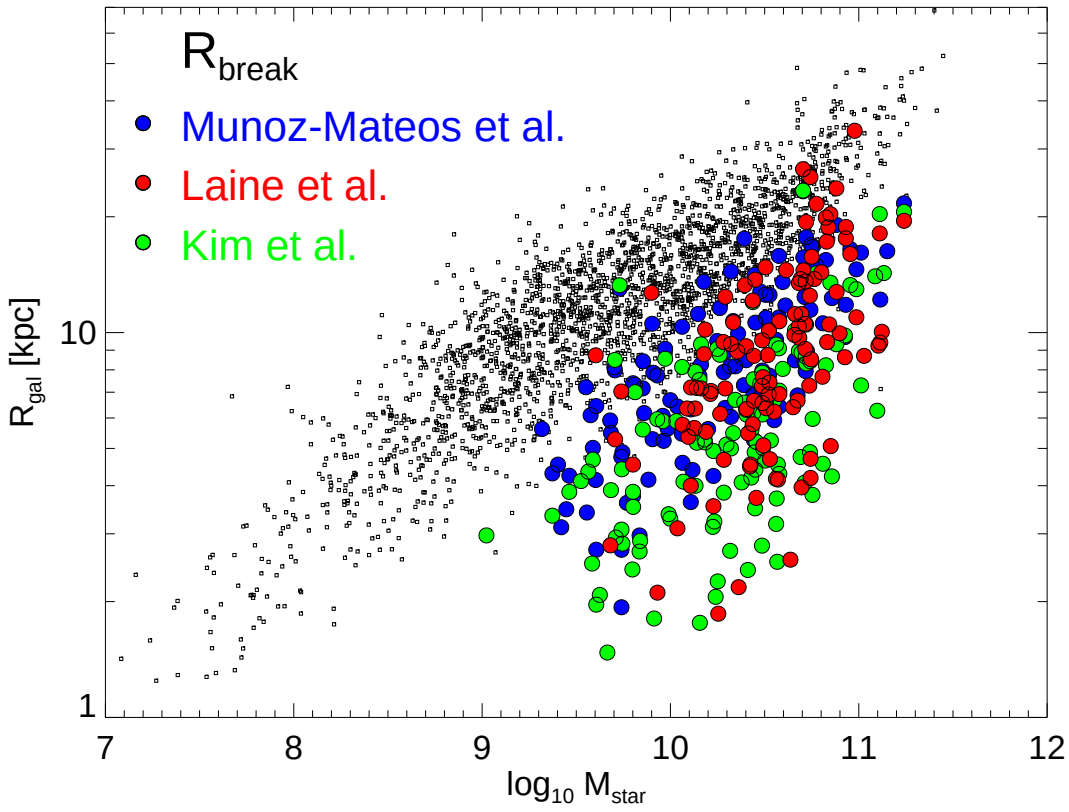

Fig. 30.— Comparison of the fitted break radius between the inner and outer disk segments in the studies of Munoz-Mateos et al. (2013), Laine et al. (2014) and Kim et al. (2014). Note that the break radius drops rapidly with galaxy stellar mass. Also shown is R_{gal}, the visual estimate of the galaxy size in S^{4}G images. The plot suggest that even in the case of low-mass, low surface galaxies the depth of the S^{4}G images is sufficient to assure that the break, if present, is not likely to be buried in the sky background.

4. Decomposition parameters

In the current paper (Part 1) we provide all the 1-component and final multi-component decomposition parameters in a tabular format, together with quality assignment flags. A brief check of how the major categories of the final models distribute among different Hubble types is also shown. All actual analysis will be presented in Part 2.

4.1. Quality assessment

The full S^{4}G sample contains 2352 galaxies, chosen according to their internal extinction corrected B-magnitude ($M_{Bcorr} < 15.5$), apparent B-band 25-mag isophotal diameter ($D_{25} > 60''$), galactic latitude ($|b| > 30°$), and HI recession velocity ($V_{radio} < 3000 km/s$), obtained from Hyperleda database. Because the sample is complete within these limits, it contains a large number of low surface brightness late-type spirals and irregulars. Also, no exclusion was made for galaxies with peculiar morphology or for galaxies with nearby bright stars. In some cases the field-of-view (FOV) is not large compared to the galaxy size (the new Spitzer observation mapped regions covering at least 1.5 D_{25}, but this condition is not satisfied with the all archival galaxies included to the sample). In such cases the sky background is difficult to estimate reliably, and for galaxies near the ecliptic, the background may have larger gradients (see Munoz-Mateos 2014). Altogether, the sample contains a number of galaxies for which decompositions are less reliable, or not possible at all to carry out.

Because it is important to estimate the reliability of the derived structural parameters, we have assigned to each galaxy a **quality flag**, running from 1 (worst case) to 5 (most reliable). The judgment was done partly by visual inspection of the original data and partly by evaluating the decomposition models:

• ***Quality=1*** (30 cases)

Reasons: Bad original data (very bright overlapping stars, strongly varying background, image defects).

Action: Excluded from all analysis: galaxy identifications are listed in parameter tables but no parameter values are given. P4 web page illustrates the raw data + mask, but no ellipticity profiles nor any decomposition models.

• ***Quality=2*** (42 cases)

Reasons: Original data is more or less fine, but the FOV is too small for reliable sky estimation. Alternatively, galaxies exhibit strongly distorted shapes which make even 1-component fits unreliable (mergers, interacting, peculiar, strong warp, very lopsided).

Action: 1-component Sérsic fit was done and the parameters are given in Table 6 (and in the web pages), together with a comment indicating that they need to be taken with caution. Multi-component decomposition are not given (only galaxy identifications are listed in Table 7).

• ***Quality=3*** (65 cases)

Reason: Original data is fine but the galaxies have complex structures that require detailed multi-component models beyond the scope of the pipeline decompositions (with maximum of 4 components).

Action: 1-component Sérsic fit is considered reliable (Table 6) . Multi-component decomposition was also made and parameters are listed in Table 7) , with a cautionary comment. Web pages show both 1-component and multi-component decompositions.

• ***Quality=4*** (404 cases)

Reason: Original data and decomposition are of good quality. However, the galaxy was either highly inclined (contained a 'z' component; 332 cases), or it had complicated

structure, so that there might be a degeneracy between model components (like between inner and outer disk components) (72 cases).

Action: All decomposition parameters given in Tables 6 and 7, and illustrated in the P4 web-pages. However, these are omitted from the analysis of disk central brightness and scale length.

• ***Quality=5*** (1810 cases)

Reason: Both the original data and the decompositions are of good quality.

Action: All decomposition parameters are given in Tables 6 and 7, and illustrated in the P4 web-pages.

Table 5 summarizes the number of galaxies in different quality categories.

4.2. One-component fits

The output parameters of 1-component Sérsic fits are listed in Table 6. For 1-component fits the parameters are the Sérsic index n, effective radius R_e, integrated magnitude mag, axial ratio q, and major axis position angle PA (the centers are fixed to those given in Table I; the isophotes are assumed to be elliptical and have fixed shape and orientation over radius). Additionally, there is a column for the quality of the data/decomposition described in Section 4.1

Single-component Sérsic-fits are routinely used in large data surveys. This gives objective, easily reproducible results, that provide useful characterization of the galaxy global characteristics[8]. For example, Cappellari et al. (2013) argued that Sérsic n>4 largely

[8]However, the derived parameters can be misleading if the Sérsic index for the whole galaxy is interpreted to characterize its bulge properties

finds the most massive early-type galaxies ($M > 3 \cdot 10^{11} M_{\odot}$), which are also the slow rotators in their kinematic classification. Also, there are well-known correlations between galaxy color and Sérsic index. Therefore, in Part 2 we will present detailed analysis of the 1-component Sérsic parameters for the S^{4}G sample. Here just the dependence of n on the morphological type is reported.

Figure 31 displays the histogram of Sérsic index-values in the 1-component models. Galaxies are divided into three bins according to their mid-IR Hubble type (E with $T \leq -4$, S0 with $-3 \leq T \leq 0$, spiral with $1 \leq T \leq 9$, and irregulars $T = 10$). Clearly, the distribution of galaxies peaks at $n \approx 1.4$, with a broad tail to larger values of n. There is also a secondary peak at $n \approx 4$ (corresponds to de Vaucouleurs profile), but this is not very prominent. The overall distribution reflects the nearly exponential profiles of many late type spirals, which dominate the S^4G sample. For irregulars, the distribution peaks at $n \approx 1$. For S0's, the distribution is much broader. The distributions remain essentially the same for less inclined galaxies, say to those with apparent $b/a > 0.5$

4.3. Multi-component decompositions

For multi-component decompositions the tabulation is more complicated, as model components/functions vary from one galaxy to another. Also, the same function can be used to describe different structures in galaxies. Therefore, Table 7 lists, for each component included in the model, both the physical interpretation of the model (*B, D (or Z), bar, N*), and the GALFIT function used (*sersic, expdisk, edgedisk, ferrer2, psf*). The Table caption specifies the parameters listed for each function.

358 galaxies were considered to be close to an edge-on vie and are excluded from further analysis in Part 2. Also, 24 are spheroidal systems, modeled with a single Sérsic function. This leaves 1855 moderately inclined disk systems. As discussed in Section 3 there are over

20 different combinations of functions/components used in the final models, so that there is a need to group the decompositions in to major categories. A natural approach is to base this grouping on whether the decomposition model has a bulge component. Because the bulge can be modeled either with a "sersic" or "psf" component, depending on its apparent size, we have two categories, *BD* and *ND* models, respectively. When there is no trace of a bulge, the system can be either a single disk (*D*), possess a bar-like component (*Dbar*), or contain both inner and outer disk components (*DD*).

The numbers and relative fractions of galaxies in these categories as a function of Hubble type are shown in Fig. 32. Apparently the relative fraction of *BD*-models decreases gradually towards the late-type spirals. However, taking into account that most of the *ND* models describe small bulges (support for this claim is given in Part 2), indicates a much smoother distribution of galaxies with bulges, dropping rapidly only above $T \sim 5$. The fact that *ND* models cover a relatively large range of Hubble types, including S0s, is quite interesting because it indicates that S0s can possess very small bulges. This is in agreement with Laurikainen et al. (2010), where the same conclusion was made based on decompositions of NIRS0S data. The result is consistent with the idea that at least some S0s might be former late-type spirals with small bulges, devoid of gas, following quenching of star formation. A very small B/T ratio in an early-type spiral has also been reported also by Kormendy & Barentine (2010). Another interesting feature in Fig 32 is that many galaxies that lack bulges, can still have bars. These *Dbar* galaxies peak at Hubble types $T = 7$. Beyond $T = 9$ they are replaced with single disks, becoming almost the sole type of models for irregulars (T=10). The *DD*-models are most common (about 10%) for $T = 9$

Finally, Fig. 33 gives examples of galaxies in these major categories, indicating the model components for the 4 least and 4 most massive systems in each category. For *BD* and *ND* categories the barred and non-barred models are also distinguished.

Table 5. Summary of decomposition quality flags

Quality	#	#(≥quality)	1-component	Multi-component	Disk μ_0 and h_r
1	30		-	-	-
2	42	2312	uncertain	-	-
3	65	2270	ok	uncertain	-
4	404	2205	ok	ok	uncertain (or z)
5	1810	1810	ok	ok	ok

Note. — Quality flags (1-5) assess the reliability of decomposition parameters. The second column indicates the number of galaxies in each class, while the third column indicates the number of galaxies with decomposition parameters of this or better quality.

Table 6. Parameters of 1-component Sérsic fits

Identification	Quality	mag	q	PA	n	R_e
ESO085-014	5	13.04	0.323	77.640	1.304	64.197
ESO085-030	4	13.15	0.519	-32.105	1.421	15.858
ESO085-047	5	15.04	0.477	31.992	1.250	43.062

Note. — *Quality* specifies the reliability of fit: value = 2 indicates that parameters are not necessarily reliable. *mag* is the the total magnitude, q is axial ratio and PA position angle of elliptical isophotes, n is the Sérsic index and R_e the effective radius (in arcsec).

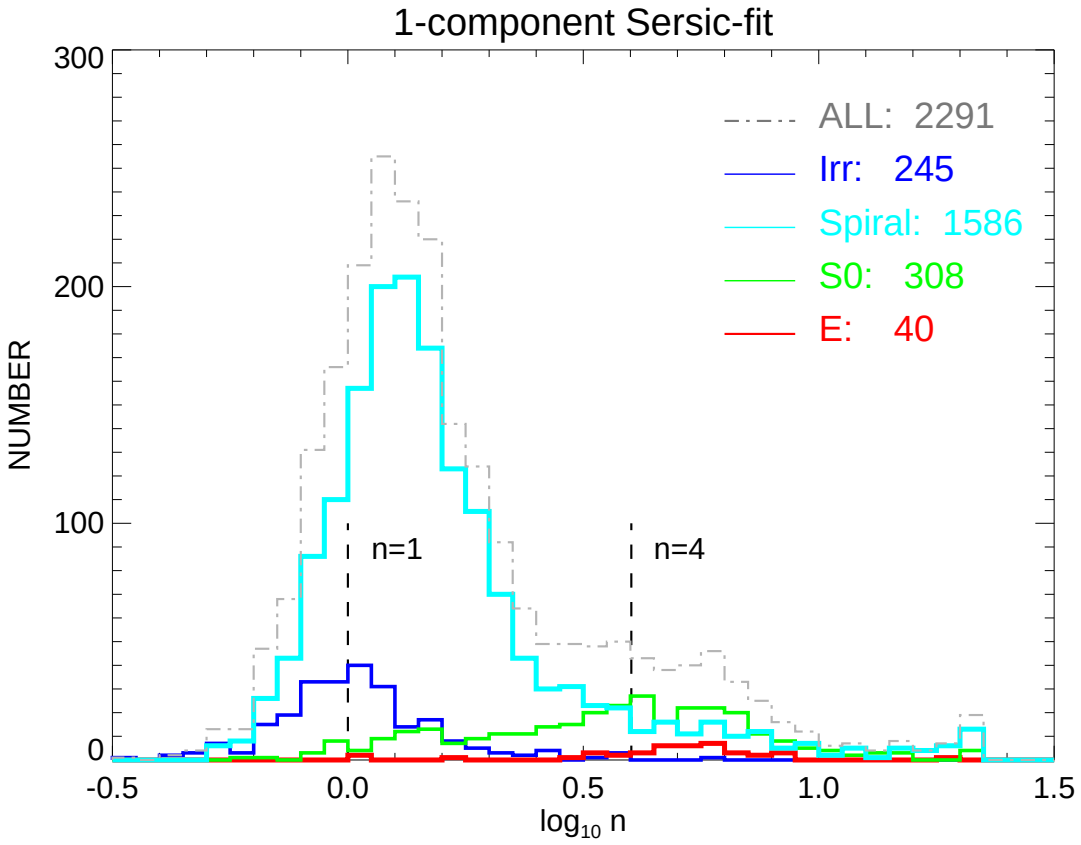

Fig. 31.— Histogram of Sérsic-index n in 1-component Sérsic-fits. Dashed line indicates the whole S^{4}G sample, after elimination of 61 galaxies due to bad image quality, bright nearby star etc. Additionally, 22 galaxies with fitted $n > 10$ fall outside the plot region. Main morphological types are shown separately with different colors (Ellipticals: $T \leq -4$, S0s: $-3 \leq T \leq 0$, Spirals: $1 \leq T \leq 9$, Irregulars $T = 10$; Additionally there are 32 dwarf galaxies ($T = 12$ not shown: their median $n = 1.06$). The mid-IR morphological classification by Buta et al. (2014) is used here and in subsequent plots, unless otherwise mentioned. The vertical dashed lines indicate the values $n = 1$ and $n = 4$, corresponding to exponential and de Vaucouleurs profiles, respectively.

Table 7. Parameters in final multi-component decompositions

0							
ESO011-005	bz	NCOMP=2	quality=4				
B	sersic	0.608	15.017	0.342	41.769	1.800	27.961
Z	edgedisk	0.392	21.055	43.928	12.881	3.663	
1							
ESO012-010	dbar	NCOMP=2	quality=5				
D	expdisk	0.939	13.550	0.458	-33.795	42.639	
B	ferrer2	0.061	22.344	0.363	22.878	31.586	
2							
ESO012-014	dbar	NCOMP=2	quality=4				
D	expdisk	0.809	15.015	0.420	31.032	38.733	
B	ferrer2	0.191	24.829	0.249	10.021	115.964	
...							
2351							
UGC12893	bd	NCOMP=2	quality=5				
B	sersic	0.017	18.087	0.786	-76.631	0.477	5.939
D	expdisk	0.983	13.671	0.869	87.208	25.515	

Note. — The first row for each galaxy is the running number (1-2352). The second row gives the galaxy name, type of final decomposition model (coded to all output file names), the number of components in the model, and the quality flag. The type of the decomposition is coded to all decomposition output file names If no final decomposition was made then for this galaxy type='-' and NCOMP=0. The next NCOMP entries give: (1) the physical interpretation of the component, (2) the GALFIT function used for it, and (3) the component's relative fraction of the total model flux. The next entries depend on the GALFIT function. For *sersic* they are: mag, q, PA, n, R_e, for *expodisk*: mag, q, PA, h_r, for *edgedisk*: μ_0, PA, h_r, h_z, for *ferrer2*: mu_0, q, PA, R_{bar}, and for *psf*: mag. Here mag is the total 3.6 μm AB magnitude, μ_0 is the central surface brightness in mag/arcsec^2, R_e, h_r, h_z are in arcsecs. All decompositions assume a fixed common center for all components and elliptical isophotal shape, constant over radii. If there is an (outer) disk, q and PA are kept fixed to those in Table 1.

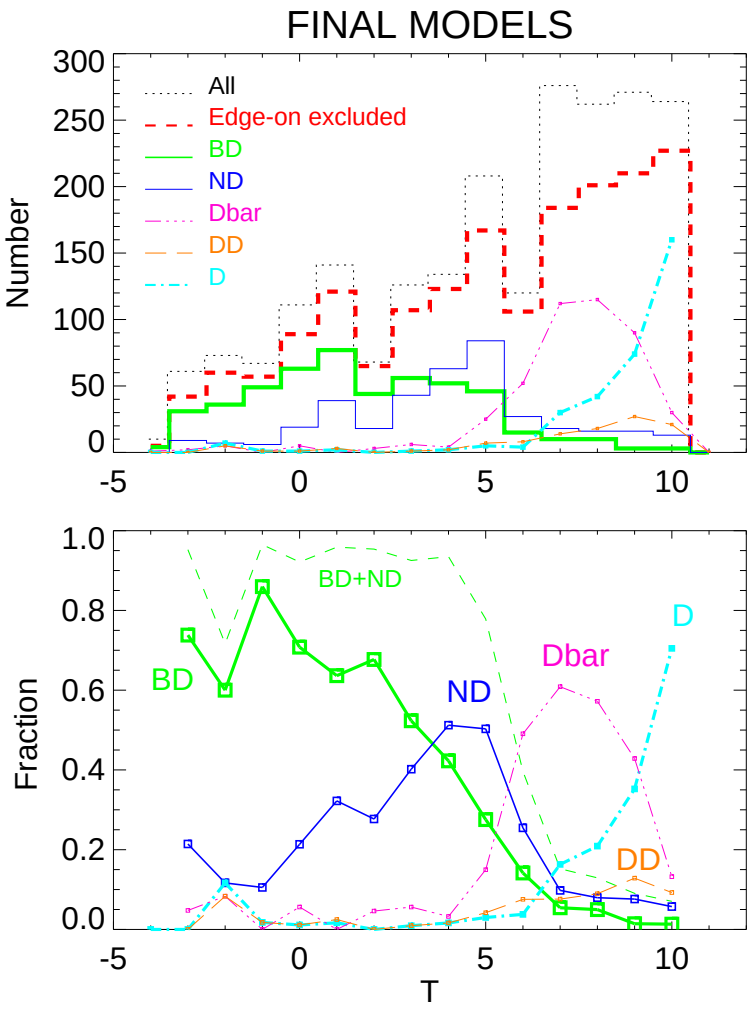

Fig. 32.— Distribution of final decomposition model categories as a function of mid-IR T. In the upper panel the distribution of the original S^{4}G sample (dotted histogram), and of galaxies with final models (red dashed line histogram; excluding the edge-one galaxies). Green histogram is the distribution of models where *both* 'bulge' and 'disk' components where identified (BD). This is also the subsample used in Section 3.1.4 when comparing automatic 2-component and final multi-component decompositions. Dashed dark blue line shows the distributions for models with *both* 'nucleus' and 'disk' (excludes those with 'bulge') (ND). The three other lines are for models with neither 'bulge' nor 'nucleus': 'Dbar' stands for models where a Ferrers-bar was included (together with one or more 'expodisk' components), 'DD' stands for models with inner and outer disks, while 'D' stands for a single 'expodisk' model. In the lower panel the relative fractions of different models are plotted, normalized to the total number of non-edge models (red dashed curve curve in the upper panel). The minor 'peak' of 'DD' and 'Dbar' galaxies at $T = -2$ consists of galaxies classified as dwarf lenticulars in Buta et al. (2014). Here 'BD' and 'ND' include both models with/without 'bar'. For clarity, these models are not shown separately as the differences are not very large.

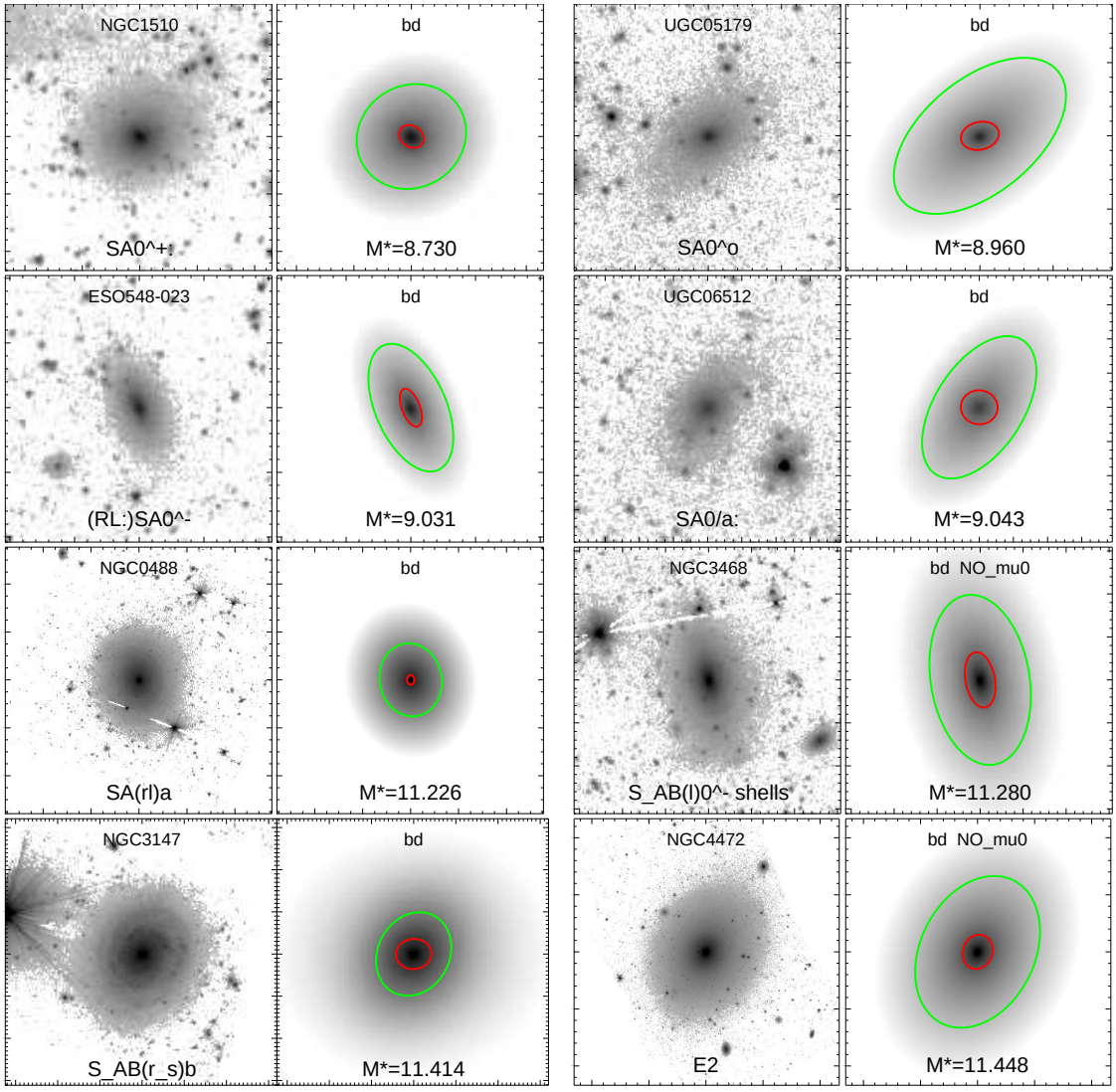

Fig. 33.— a) Examples of different main types of final decomposition models. The four least massive and four most massive galaxies of each type are displayed. The left frames display the 3.6 μm image, with fixed AB magnitude range [18,27], while the right indicates the model components with ellipses with semi-major axis corresponding to $2R_{\rm eff}$ of the component. The labels in the left frame indicate the galaxy name and the Buta et al. (2014) mid-IR classification. Labels in the right frames give the physical coding of the decomposition model components (same as used in the names of the decomposition files, and the $\log 10(M_{star})$ (Stellar masses from Munoz-Mateos et al. 2014). The colors of the ellipses indicate the used functions: expodisk (green), sersic (red), ferrer2 (blue). Similar plots for all galaxies are given in the P4 web-page. In a) examples of **BD** models (without bars) are displayed.

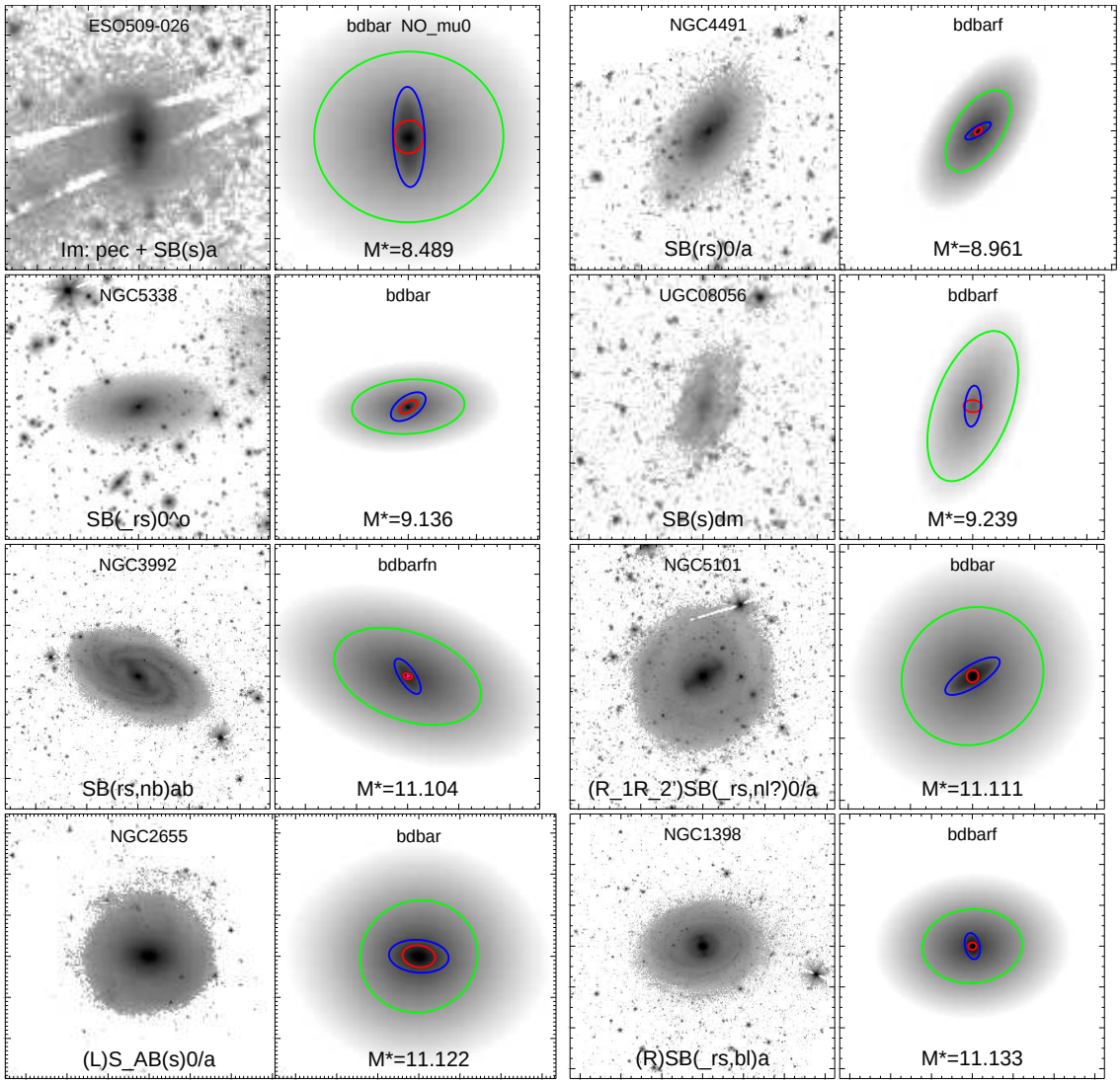

Fig. 33b.— Examples of **BDbar** decomposition models.

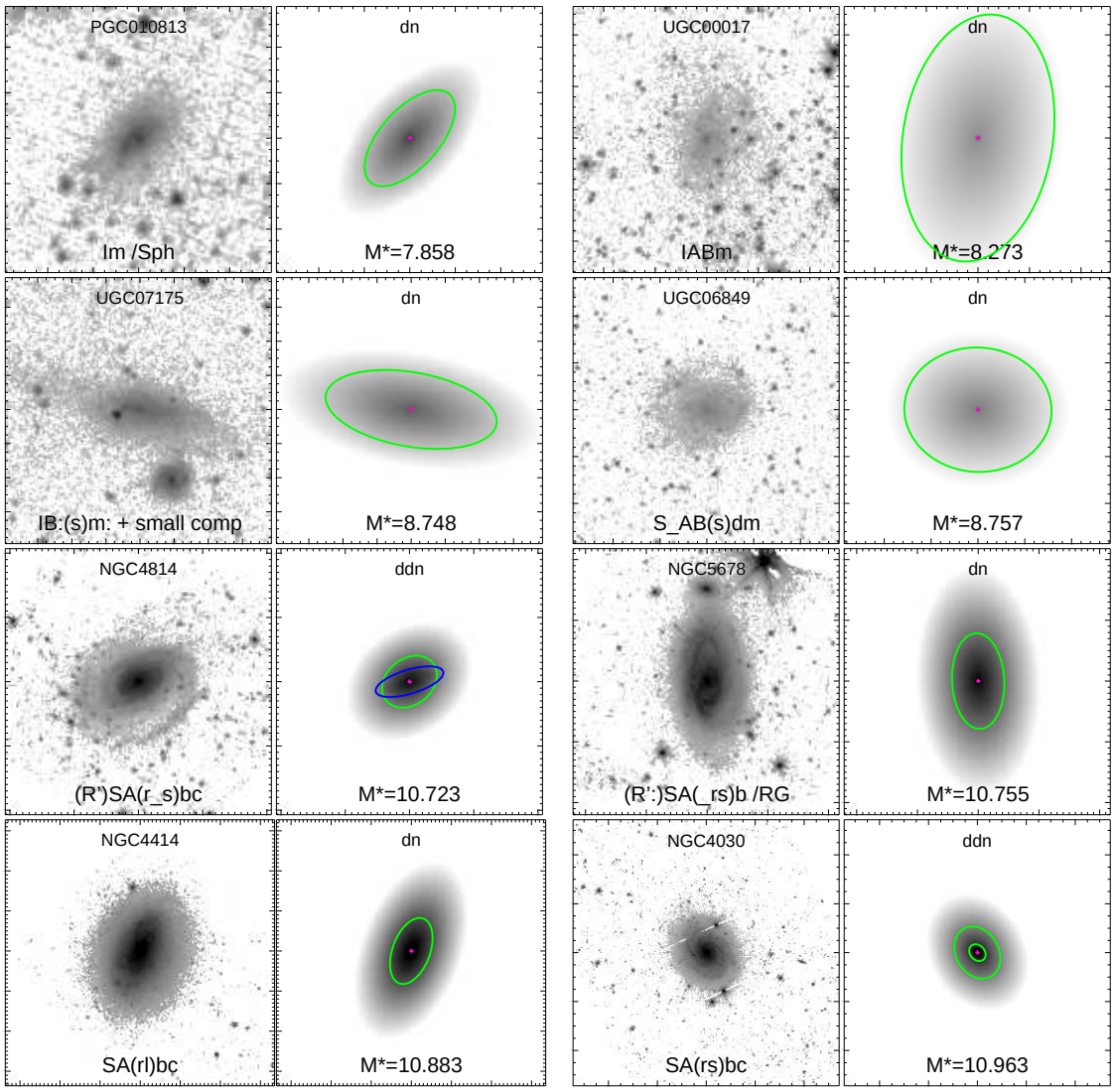

Fig. 33c.— Examples of **ND** decomposition models. The central component (unresolved in decomposition) is indicated with a red dot.

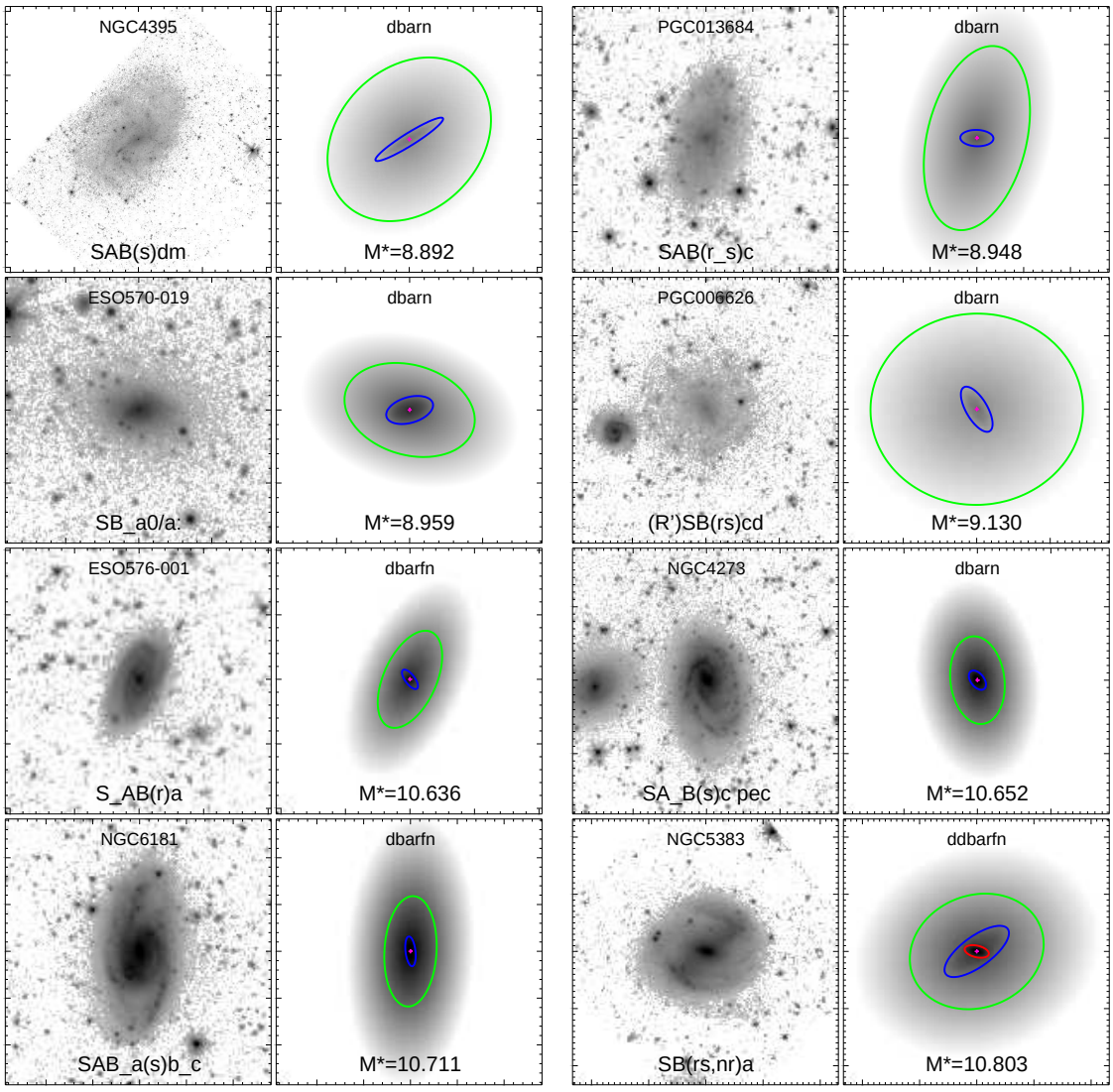

Fig. 33bd.— Examples of **NDbar** decomposition models. The central component is indicated with a red dot.

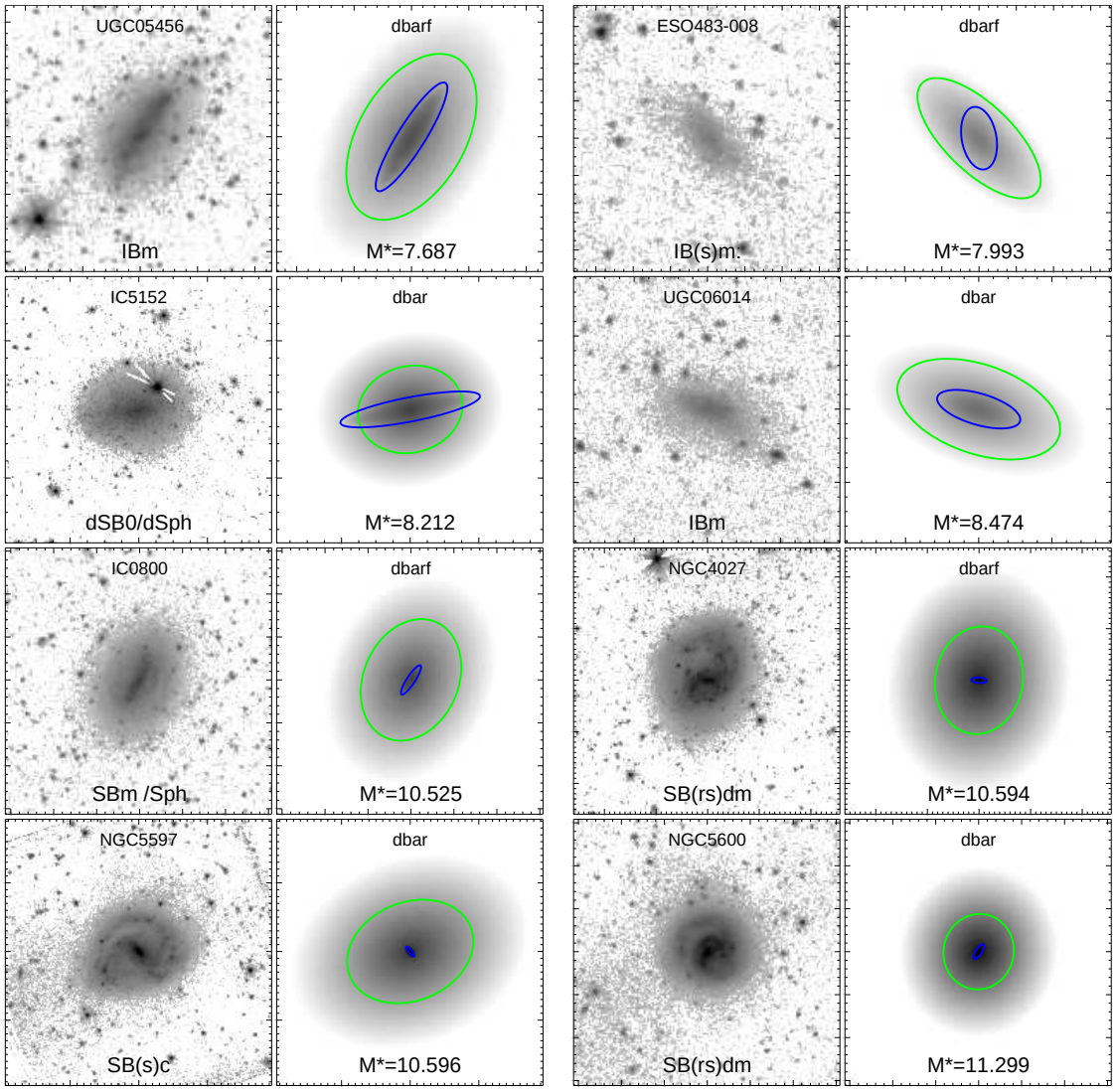

Fig. 33e.— Examples of **Dbar** decomposition models.

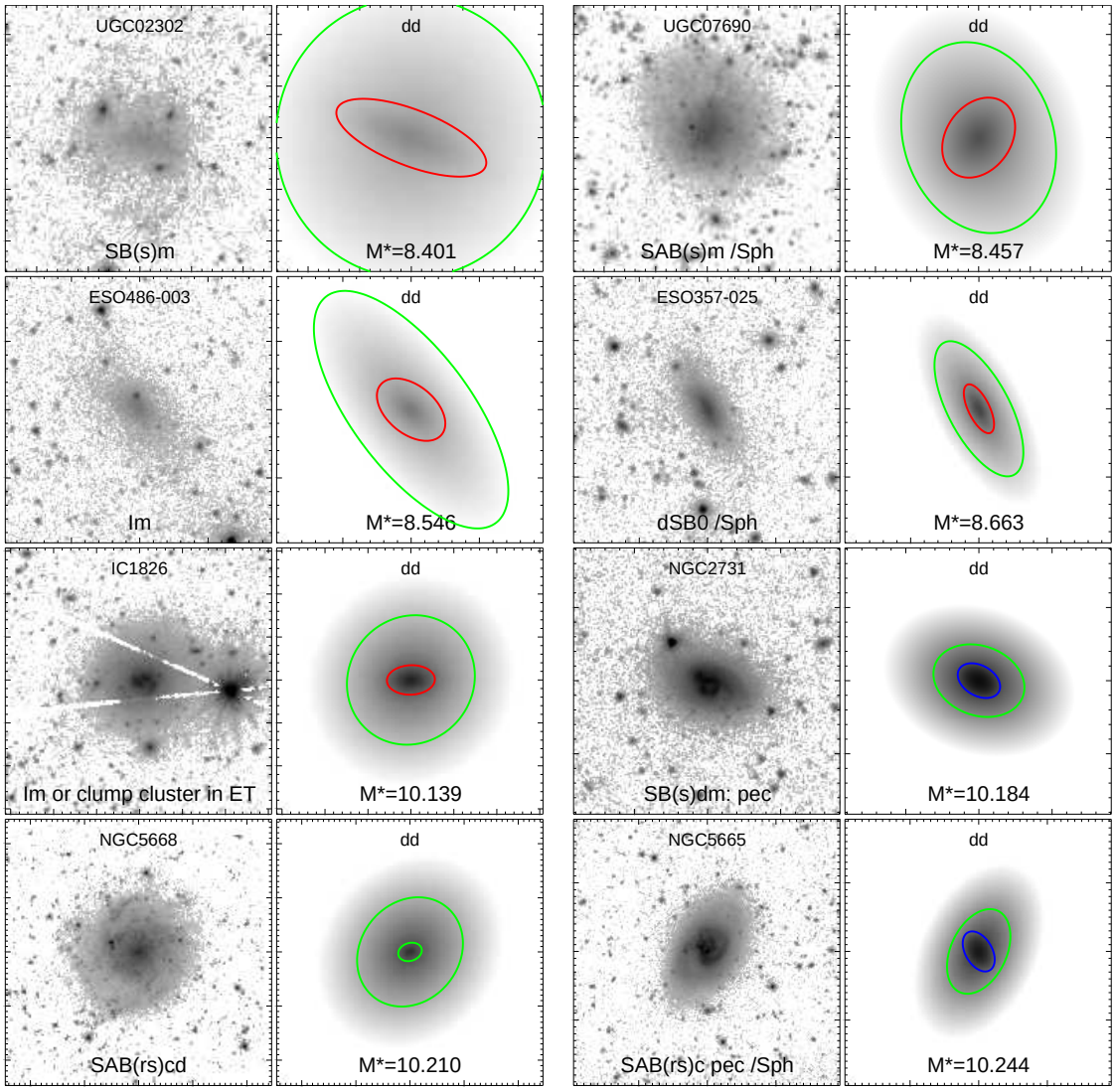

Fig. 33f.— Examples of **DD** decomposition models.

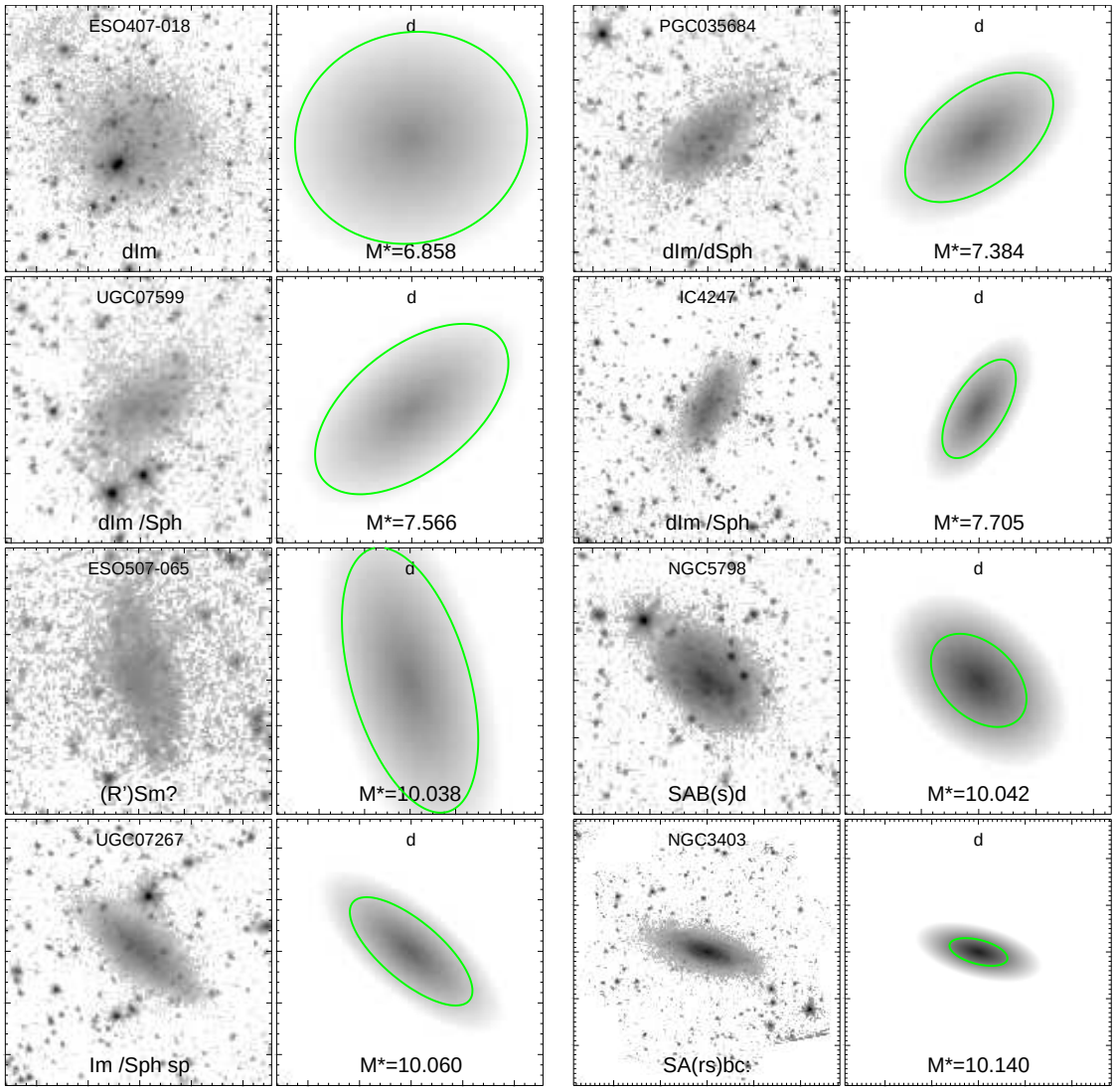

Fig. 33g.— Examples of **D** decomposition models.

5. Summary and Conclusions

Two-dimensional multi-component decompositions, using GALFIT3.0, have been performed at 3.6 μm wavelength for the complete S^{4}G sample (2352 galaxies). Reliable decompositions were possible for 2237 galaxies. Quality flags are given for each galaxy based on the level of confidence on the model parameters. The main goal of the decompositions was to estimate the structural parameters of the bulges and disks in a reliable manner, which dictated our decomposition strategy. Most importantly, a bar-component was included in the decomposition model whenever present, to prevent its light from biasing the derived bulge and disk parameters. However, no attempt was made to match the detailed shape or length of the bar. For the same reason, the models sometimes included a central point source and additional disk components.

We present automated single Sérsic and bulge-disk (Sérsic + exponential) decompositions, and human-supervised, individually checked multi-component models. In the final multi-component models, a maximum of four structural components are fit: bulge (Sérsic), disk (exponential), bar (modified Ferrers), and the nucleus (PSF). Different combinations of component functions were used. For example, in some barred galaxies it was convenient to fit the underlying disk with two different functions. As a first step, we estimated the sky background levels, derived the orientation parameters with ellipse fitting, and edited the masks to eliminate foreground stars and image defects (see also Munoz-Mateos et al. 2014). The uncertainties related to the sky background and the adopted PSF-function were tested. The decomposition data are released in IRSA, and in the P4 web-page, where the decomposition models, the ellipse fitting, and sky background determinations are illustrated. The IDL-based tool (GALFIDL) used in visualization of GALFIT decompositions is also available on the web pages. Besides the decomposition output files, all input files needed in re-doing the decompositions are given in IRSA. All of this provides the possibility to refine

the pipeline models for the needs of specific scientific goals.

The main results are the following:

(1) *Automatic single Sérsic fits.*The Sérsic indexes peak at $n \sim$1.5, having only a minor peak at $n \sim$4, reflecting the fact that a large majority of the sample galaxies are spirals with extended disks.

(2) *Automatic 2-component bulge-disk decompositions*: These suggest a large difference in the parameters of the bulges between barred and non-barred galaxies. The peak value of the Sérsic index in barred galaxies, $n \sim$4, consistent with other similar bulge-disk decompositions applied on samples dominated by barred galaxies. However, we strongly caution in using the automatic 2-component decompositions.

(3) Final *multi-component decompositions*. In contrast to 2-component models, in our final models the differences in bulge parameters between barred and non-barred galaxies disappear, leading to the values of Sersic $n \sim 1-2$ for both types of galaxies. It means that if bars are not included in the fit, the flux of the bar is erroneously mixed with the bulge flux, consistent with several previous studies using a similar multi-component decomposition approach (REF)

(4) Small bulges containing at most a few percent of the galaxy flux at 3.6 μm appear in a large range of Hubble types, including S0s. This result is in agreement with Laurikainen et al. (2010) where results were obtained in near-IR.

(5) At intermediate Hubble types (T=5-7) the very small bulges gradually disappear but the disk can still be unstable to bar formation. At the very end of the Hubble sequence pure disks become dominant.

A detailed analysis of the properties of bulges, disks, and bars, as a function of morphological type, and other overall properties (galaxy mass and global color) will be

presented in forthcoming paper (Part2 in preparation).

6. Acknowledgments

H. Salo, E. Laurikainen, and S. Comeron acknowledge the Academy of Finland for support. J. Laine was supported by the Väisälä Foundation Grant.

We thank J. Janz for discussions and for help with the initial preparation of the web-pages.

A. Appendix: Decomposition pipeline products in IRSA

The results of pipeline 1-component and final multi-component decompositions are available via IRSA database. For each galaxy, decomposition output parameters (*outgal*-file), and input fits-files are given. The user can refine/improve the given multi-component models by including more components or by utilizing additional GALFIT options for the component functions. [9]

```
-----------------------------------------
1) Input data for GALFIT decompositions
-----------------------------------------

IDE is the galaxy designation (e.g. NGC1097)

fits-files:
  IDE.phot.1_nonan.fits     = 3.6 micron image used in decompositions,
                              Bad pixel values (NaN's) removed
      header modified to make GALFIT work correctly
  IDE.1.finmask_nonan.fits  = corresponding mask-file
  IDE.phot.1_sigma.fits_ns  = -"- sigma-image
  PSF-1.composite.fits      = PSF-image

-----------------------------------------
2) Output from GALFIT decompositions
-----------------------------------------

a) ascii-files:

  IDE_onecomp.outgal       =    Automatic best fit parameters for 1-component S\'ersic model
  IDE_twocomp.outgal       =    -"-  for 2-component sersic+expodisk (or sersic-edgedisk) fit
  IDE_MODEL.outgal         =    Final decomposition model with up to 4 different components


  IDE is the galaxy designation (e.g. NGC1097)
  MODEL-string identifies the components included in the final multi-component model:

        'b'    indicates bulge-component
        'd'    indicates disk -"-
```

[9]It is important to use the data and mask files from IRSA P4 directories when refining the given decompositions, instead of using corresponding data products from P1 and P3 directories. Namely, the P4 *outgal*-files assume sky subtracted data images (with NaN image values removed) and EXPTIME keywords set to 1 sec. Additionally, the (P4 vs (P1 & P3)) data and mask images may have small spatial shifts (a few pixels) and correspond to slightly different sky background levels, depending on when the various pipeline products were finalized.

```
        'bar'  indicates non-axisymmetric structure, mainly bars
        'n'    indicates nucleus (or nonresolved bulge)
        'z'    indicates edge-on disk

         e.g. "NGC1415_bdbar"  -> bulge+disk+bad final decomposition model

  These outgal-files contain the decomposition output parameters
  Together with the input fits-files, the user can immediately repeat/refine the decompositions
  starting from the outgal-file (e.g. outgal -o1 NGC1415_bdbar.outgal   -> re-creates


b) fits-file (for the FINAL model)

  IDE_MODEL.outgal_subcomps.fits      Final decomposition output images:
                                      extension 1 =  OBS image
                                      extension 2,3,4... = model components
                                      File header contains also final decomposition parameters.


c) jpg-files (for the FINAL MODEL)

   IDE_MODEL.outgal_profile.jpg        Decomposition model compared with observations:
                                       - shows surface brightness at each image pixel vs distance from galaxy center
         Observed image, model image, and model components displayed separately
       - Collects also decomposition input & output parameters
         Labels indicate relative contribution of model components

   IDE_MODEL.outgal_residual.jpg       Model-observation comparisons:
           upper row: clipped 3.6 micron image, masked image
       lower row: model image, OBS-MODEL residual

   IDE_MODEL.outgal_1dprof.jpg         Decomposition model profiles compared with observations:
                                       - shows surface brightness as a function of isophotal semi-major axis,
         comparing IRAF ellipse fits to the observed image and to the
 model image (using isophotes of the observed image)


   IDE_MODEL.outgal_components.jpg     Schematic plot of model components:
           -  Upper row: Observed image and model image, with different model
          components marked: colors correspond to profile plots, and the semimajor-axis
          of the ellipse is 2 times the effective radius of the components
       -  Lower row: same as upper row, except projected to the disk plane
          (assuming zero-thickness). Empty in case on edge-on final model.


================================================================================================================
  The final decomposition models, as well as various intermediate steps involved, are illustrated in the web-page
  http://www.oulu.fi/astronomy/S4G_PIPELINE4/MAIN
================================================================================================================
```

B. Appendix: Decomposition Pipeline web-pages

The input data used in decompositions, the various steps of the decomposition pipeline, and the final decomposition results are illustrated on the Pipeline 4 web site[10]

`http://www.oulu.fi/astronomy/S4G_PIPELINE4/MAIN`

The web site consists of three layers of pages:

1) Main page

2) Index pages

3) Decomposition pages

The **main page** gives full instructions regarding the contents of the pages, followed by an alphabetical list of all 2352 galaxies in the original sample Clicking on any of the galaxy names opens a corresponding *index page*, with contains information for 100 galaxies, near and including the chosen galaxy (Fig. 34).

The icons in the **index page** indicate the data available for each galaxy

1) P1 image mosaic
2) clipped P1 image, with mask
3) clipped P1 image
4) Deprojected image
5) Elliptical isophote profiles
6) Galaxy center/sky background plots

What decompositions available:

7) 1-component Sérsic-model (icon shows residual plot)
8) Final-model (icon shows residual plot)
9) Final-model (icon shows model components)

An empty icon signifies no data/decomposition model, for instance if the galaxy was discarded from further analysis because of a nearby bright star, etc. In particular, the absence of a final model indicates that the galaxy was considered too problematic to fit reliably (e.g. closely interacting, very peculiar or warped).

Clicking on the galaxy name links to its **decomposition page** (Fig. 35), which

[10]The website does not contain actual fits-files, which are available via the IRSA server/P4.

summarizes the mask, ellipse fitting, sky background, and galaxy center determinations, as described in Section (2.2).

In addition, the pages display for all three types of models (1-component Sérsic model, 2-component bulge/disk model , final multi-component model) the

2D profile plot

Residual plot

1D profile plot

Model-components plot

Again, clicking on the plots displays the full size plots (Figs. 36 37, 38, 39).

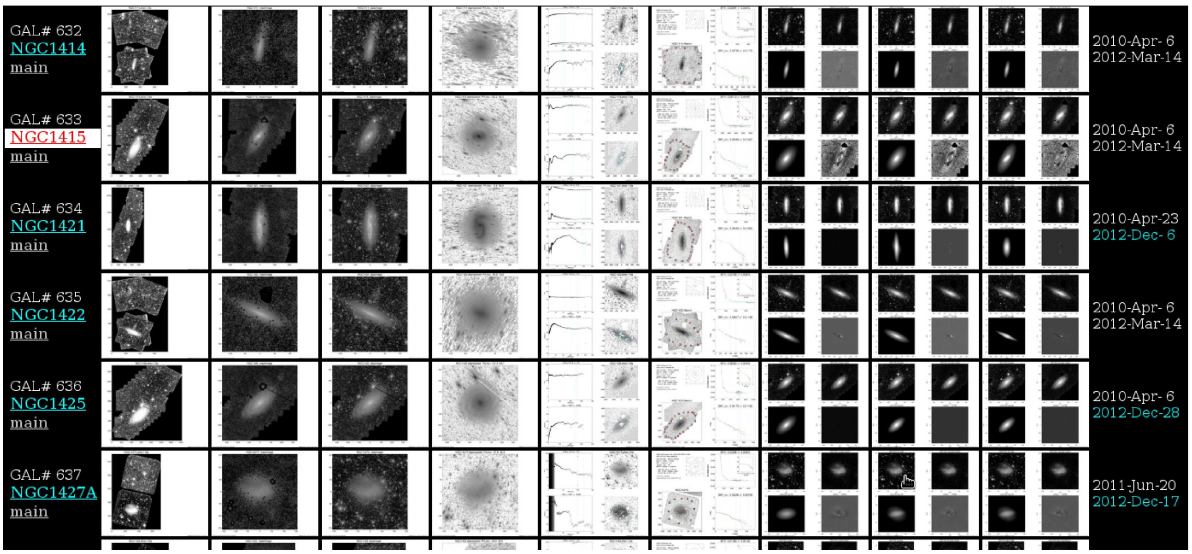

Fig. 34.— Screenshot of Pipeline 4 index page.

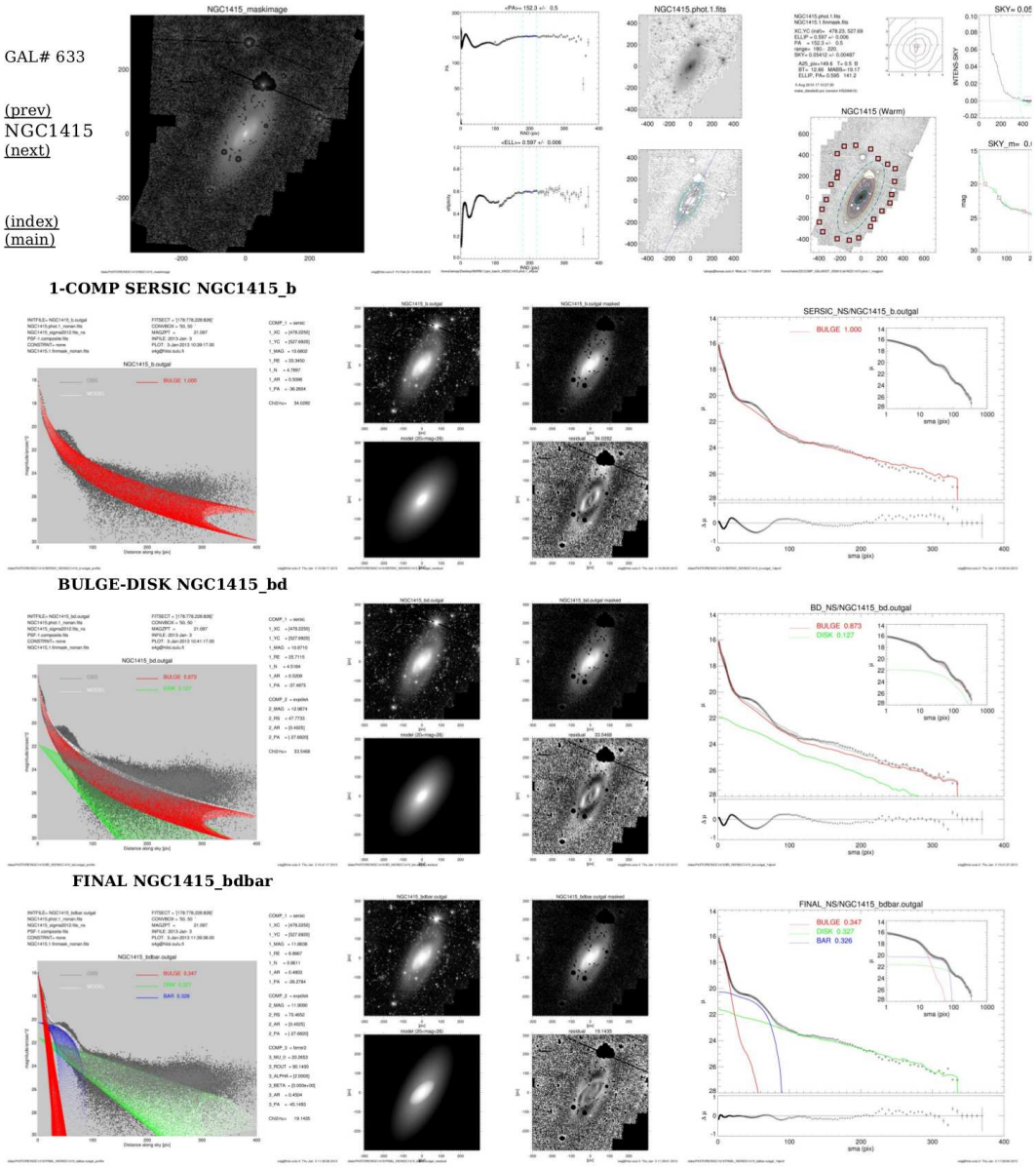

Fig. 35.— Screenshot of various decomposition models for this particular galaxy. Clicking on the image icons opens the enlarged image.

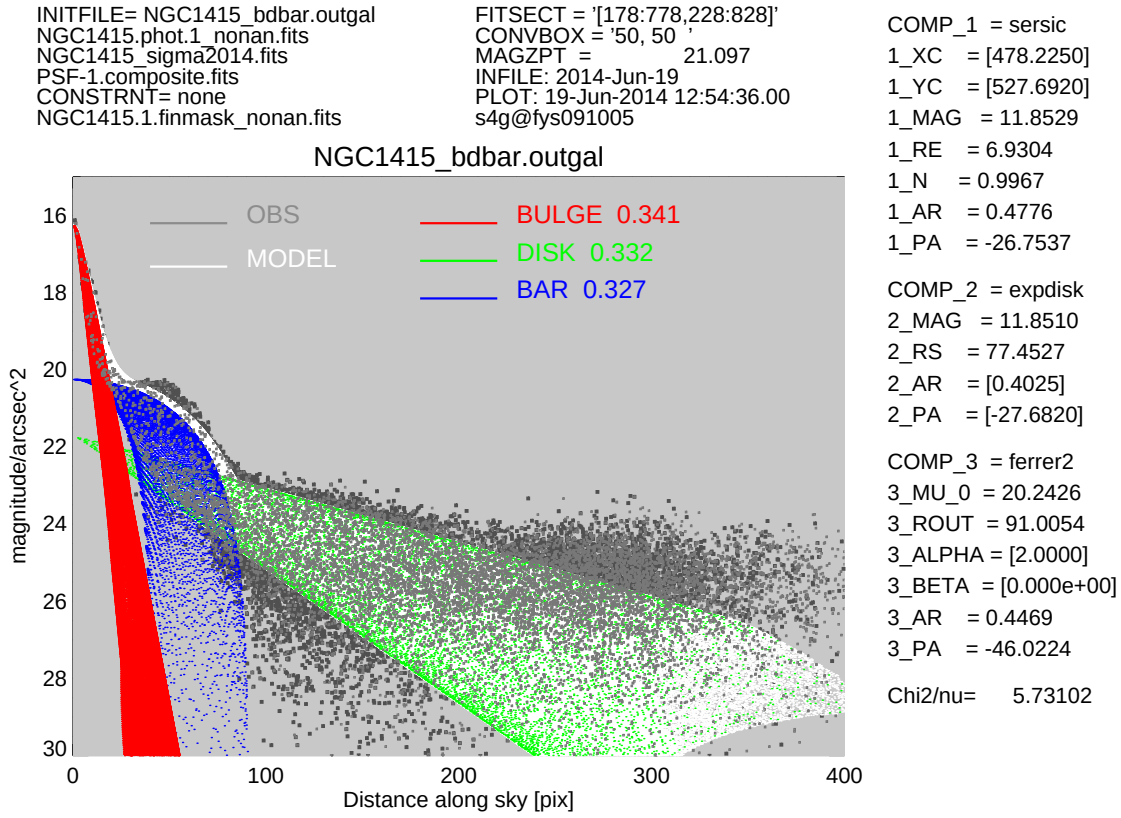

Fig. 36.— Final *pipeline* decomposition for NGC 1415. The decomposition includes bulge, disk, and bar components, indicated by different colors. The numbers after the labels indicate the relative fraction of light in each component. This 2D-profile indicates the brightness of each pixel versus its distance from the galaxy center. The frame also collects the names of the input data files and the final GALFIT decomposition parameter values.

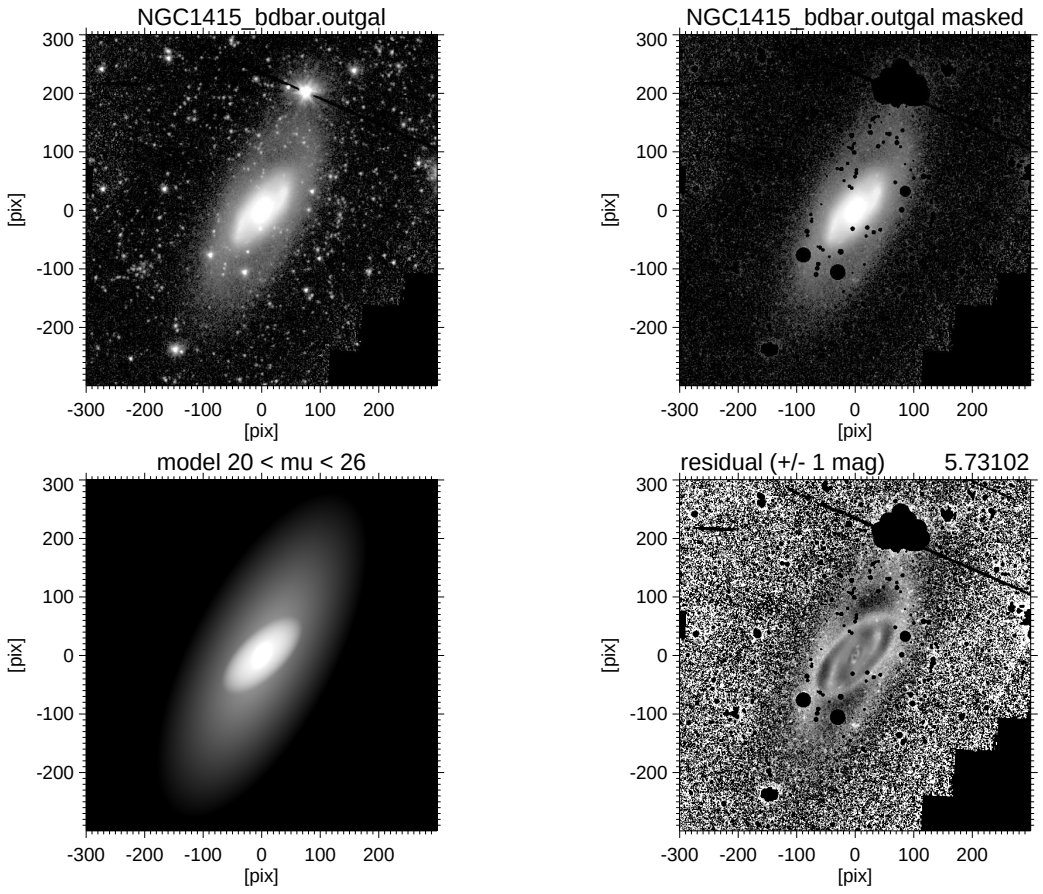

Fig. 37.— Final *pipeline* decomposition for NGC 1415, corresponding to Fig. 36. The upper frames show the observed, clipped and sky-subtracted image (left) and the corresponding masked image (right). The lower frames display the model image (left), and the observed-model residual image (gray scale covers ±1 mag).

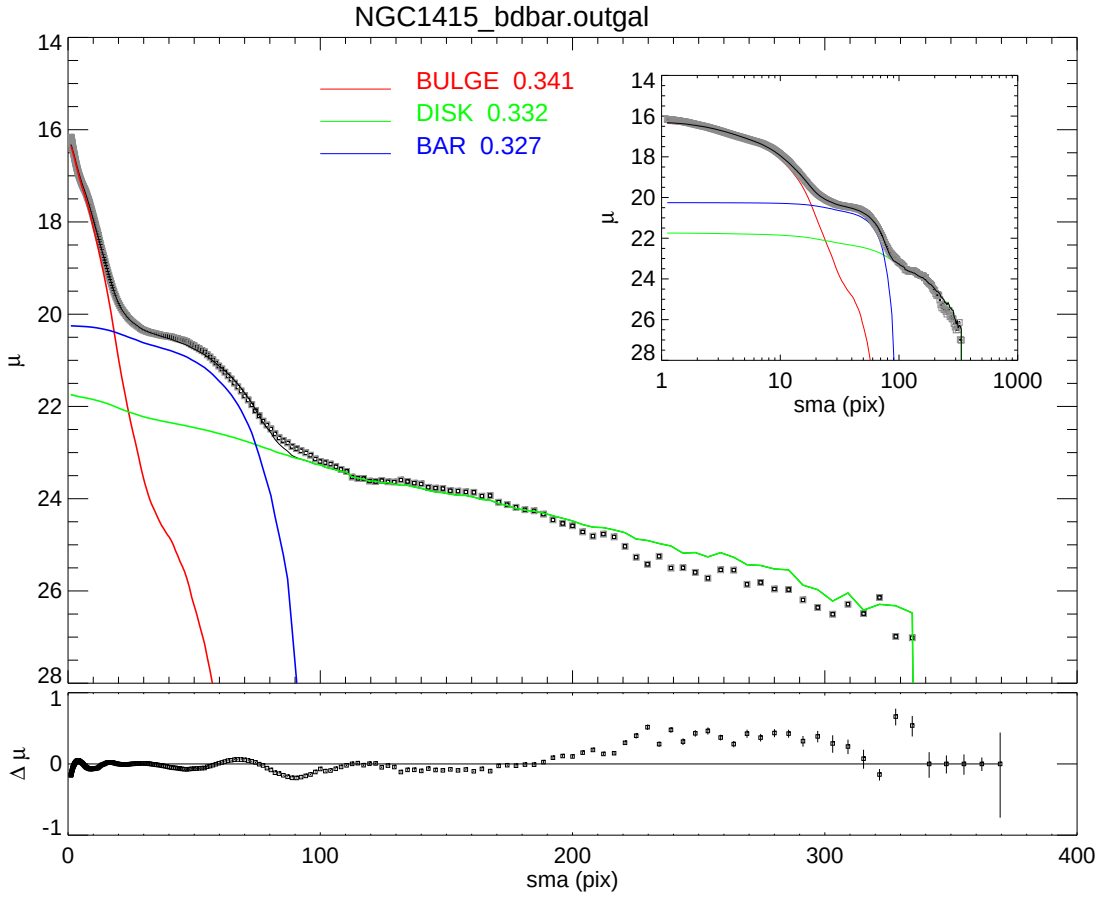

Fig. 38.— One dimensional profiles corresponding to Fig. 36. The symbols indicate the azimuthally averaged surface brightness as a function of semi-major axis, obtained with IRAF ellipse-routine. The curves indicate the azimuthally averaged profiles of the model components, using the same isophotes.

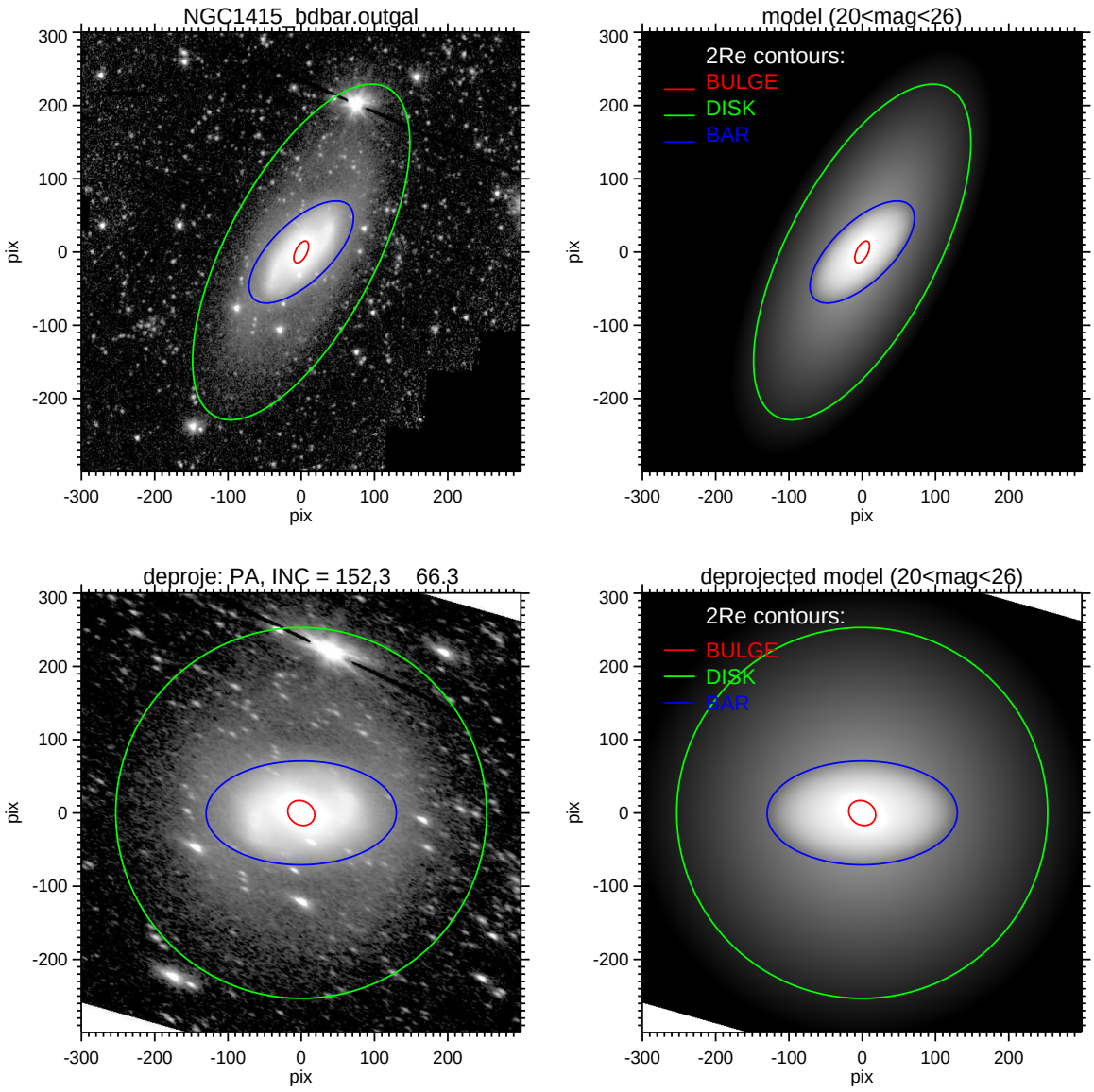

Fig. 39.— Illustration of the model components corresponding to Fig. 36. The upper left shows the observed image, together with superposed ellipses illustrating the various components of the final model: the size of the ellipse corresponds to 2 effective radii, the orientation corresponds to the components' axial ratio and PA. In the upper right, the same but showing the model image. The lower frames are similar, except that the observed galaxy and the model have been deprojected, using the assumed disk orientation parameters.

REFERENCES

Allen, P., Driver, S., Graham, A., Cameron, E., Liske, J., de Propris, R., 2006, MNRAS, 371, 2

Athanassoula, E., Morin, S., Wozniak, H., Puy, D., Pierce, M., Lombard, J., Bosma, A., 1990, MNRAS, 245, 130

Bakos, J., Trujillo, I., 2012, MSAIS, 25, 21

Barazza, F., Jogee, S., Marinova, I., 2008, ApJ, 675, 1194

Bertin, E., Arnouts, S. 1996, A&AS, 117, 393

Cameron, E., Driver, S., Graham, A., Liske, J., 2009, ApJ, 699, 105

Cappellari, M., McDermid, R., Alatalo, K., Blitz, L., Bois, M., Bournaud, F., Bureau, M., Crocker, A., Davies, R., Davis, T. and 14 coauthors, 2013, MNRAS, 432, 1862

Comerón, S., Elmegreen, B. G., Knapen, J. H., Sheth, K., Hinz, J. L., Regan, M. W., Gil de Paz, A., Muñoz-Mateos, J.-C., Menéndez-Delmestre, K., Seibert, M., Kim, T., Mizusawa, T., Laurikainen, E., and 10 co-authors, 2011, 738, L17

Comerón, S., Elmegreen, B. G., Salo, H., Laurikainen, E., Athanassoula, E., Bosma, A., Knapen, J. H., Gadotti, D. A.,Sheth, K. and 10 coauthors, 2012, ApJ, 759, 98

Driver, S., Allen, P., Graham, A., Cameron, E., Liske, J., Ellis, S., Cross, N., De Propris, R., Phillipps, S., Couch, W., 2006, MNRAS, 368, 414

Driver, S., Robotham, A., Bland-Hawthorn, J., Brown, M., Hopkins, A., Liske, J., Phillipps, S., Wilkins, S., 2013, MNRAS, 430, 2622

Draine, B., Lee, H., 1984, ApJ, 285, 89

Erwin, P., Beckman, J., Pohlen, M., 2005, ApJ, 626, L81

Eskridge, P. B., Frogel, J. A., Pogge, R. W., Quillen, A. C., Berlind, A. A., Davies, R. L., DePoy, D. L., Gilbert, K. M., Houdashelt, M. L., Kuchinski, L. E., and 5 coauthors, 2002, ApJS, 143, 73

Freeman K., 1970, ApJ, 160, 811

Gadotti D., 2009, MNRAS, 393, 1531

Graham A., Worley C.C., MNRAS, 388, 1708

Häušler, B., Bamford, S., Vika, M., Rojas, A., Barden, M., Kelvin, L., Alpaslan, M., Robotham, A., Driver, S., Baldry, I., and 6 coauthors, 2013, MNRAS, 430, 330

Huang, S., Ho, L., Peng, C., Li, Z. Barth, A., 2013, ApJ, 766, 47

vad der Kruit, P. C., Searle L. å, 95, 105

Jedrzejewski R. I., 1987, MNRAS, 226, 747

Lackner, C., Gunn, J., 2012, MNRAS, 421, 2277

Kim, T-, Gadotti, D., Sheth, K., Athanassoula, E., Bosma, A., Lee, M., Madore, B., Elmegreen, B., Knapen, J., Zaritsky, D. and 17 coauthors, 2013, astro-ph:1312.3384

Kormendy, J., Barentine J.C., 2010, ApJ, 715, 176

Laine et al. 2014, Accepted to MNRAS.

Landsman 1993, in Astronomical Data Analysis Software and Systems II, A.S.P. Conference Series, Vol. 52, ed. R. J. Hanisch, R. J. V. Brissenden, and Jeannette Barnes, p. 246.

Laurikainen, E., Salo, H., Buta, R., 2005, MNRAS, 362, 1319

Laurikainen, E., Salo, H., Buta, R., Knapen, J., Speltincx, T., Block, D. L., 2006, AJ, 132, 2634

Laurikainen, E., Salo, H., Buta, R., & Knapen, J. H., 2007, MNRAS, 381, 401

Laurikainen, E., Salo, H., Buta, R., & Knapen, J. H., 2009, ApJ, 692, 34

Laurikainen, E., Salo, H., Buta, R., Knapen, J. H., Comerón, S., 2010, MNRAS, 405, 1089

Meidt, S., Schinnerer, E., Knapen, J. H., Bosma, A., Athanassoula, E., Sheth, K., Buta, R., Zaritsky, D., Laurikainen, E., Elmegreen, D., and 16 coauthors, 2012, ApJ, 744, 17

Melvin, T., Masters, K., Lintott, C., Nichol, R., Simmons, B., Bamford, S., Casteels, K., Cheung, E., Edmondson, E., Fortson, L., and 4 coauthors 2014, astro-ph:1401.3334

Nair, P., Abraham, R., 2010, ApJ, 714, 260

Pahre, M. A., Ashby, M. L. N., Fazio, G. G., Willner, S. P. 2004, ApJS, 154, 235

Peletier, R., Kutdemir, E., van der Wolk, G., Falcón-Barroso, J., Bacon, R., Bureau, M., Cappellari, M., Davies, R., de Zeeuw, P., Emsellem, E., and 8 coauthors, 2012, MNRAS, 419, 2031

Peng, C., Ho, L., Impey, C. Rix, H., 2002, AJ, 124, 266

Peng, C., Ho, L., Impey, C., Rix, H., 2010 AJ, 139, 2097

Sellwood, J.A., 2008, in 'Dynamical Evolution of Disk Galaxies', Astronomical Society of the Pacific Conference Series 396, eds. . G. Funes & E. M. Corsini

Sheth, K. et al, submitted to ApJ.

Silk, J, 2013(review, astro-ph 1312.0107)

Skrutskie, M. F., Cutri, R. M., Stiening, R., Weinberg, M. D., Schneider, S., Carpenter, J. M., and 25 coauthors, 2006, AJ, 131, 1163 (Cambridge Univ. Press), 111 Practical Statistics for Astronomers (Cambridge Univ. Press)

Weinzirl, T., Jogee, S., Khochfar, S., Burkert, A., Kormendy, J. 2009 ApJ696, 411.

This manuscript was prepared with the AAS LaTeX macros v5.2.